University of Zurich^UZH

# Distribution of Ice Cliffs on Debris-covered Glaciers in High Mountain Asia

GEO 511 Master's Thesis

**Author**
Seraina Walz
15-702-186

**Supervised by**
Dr. Francesca Pellicciotti (francesca.pellicciotti@wsl.ch)

**Faculty representative**
Prof. Dr. Andreas Vieli

28.09.2021
Department of Geography, University of Zurich

Universität Zürich^UZH
Geographisches Institut

Eidg. Forschungsanstalt für Wald, Schnee und Landschaft WSL

MASTER THESIS

HIGH MOUNTAIN GLACIERS AND HYDROLOGY, WSL

DEPARTMENT OF GEOGRAPHY, UNIVERSITY OF ZURICH

---

# DISTRIBUTION OF ICE CLIFFS ON DEBRIS-COVERED GLACIERS IN HIGH MOUNTAIN ASIA

---

SUBMITTED BY:
Seraina Walz
seraina.walz@uzh.ch
15-702-186

SUPERVISOR:
Dr. Francesca Pellicciotti
High Mountain Glaciers and Hydrology
WSL

FACULTY MEMBER:
Prof. Dr. Andreas Vieli
Department of Geography
University of Zurich

September 28, 2021
Zürich

# Abstract

Ice cliffs are important contributors to the melt of debris-covered glaciers but their role in the glacier mass balance is not yet fully understood due to a lack of data on their distribution at larger scales. Previous research on ice cliff distribution of individual glaciers delineated the ice cliffs manually in a subjective and time-consuming manner. Recent studies used semi-automatic approaches based on elevation, spectral signature or multispectral data. However, these methods had difficulties to address the diversity in the slope and spectral signal of ice cliffs. This thesis adapted a new semi-automated approach based on Linear Spectral Unmixing with scaling factor (LSU-s) to use it with PlanetScope satellite images. These freely available high resolution multispectral images allow a detailed mapping of ice cliffs on several sites in High Mountain Asia. The usability of PlanetScope data is assessed by applying the mapping approach to three test sites in the Himalaya. After the addition of further process steps particularly the bias correction to Landsat-8 scenes with Empirical Quantile Mapping, the adapted LSU-s method is used to map the ice cliff distribution at four study sites in High Mountain Asia each covering four to seven glaciers. The ice cliff density calculated from the ice cliff distribution is then compared to glacier characteristics to find potential ice cliff driving factors. We find that PlanetScope images are applicable to map a detailed ice cliff distribution on similar sites regarding surface characteristics and climate regime. The relative ice cliff area derived in this study is mostly higher than what was stated in former studies which is due to a positive bias in our results or a change of surface characteristics of the investigated glaciers. Additionally, we discover a correlation between the ice cliff density and the longitudinal gradient, driving stress and glacier velocity which can be associated with an increasing number of large ice cliffs next to supraglacial ponds on downwasting glacier surfaces. Overall, these results show that the semi-automatic ice cliff mapping approach used with PlanetScope data derives a detailed ice cliff distribution which allows a better analysis of ice cliff formation processes at different scales and therefore contributes to the better understanding of the role ice cliffs play in the glacier mass balance.

# Acknowledgements

My greatest thanks go out to Marin Kneib, who was my biggest support and accompanied me through all steps of my Master thesis. Thank you very much for providing me with numerous very helpful Matlab codes and for all your constructive ideas, corrections and comments on my thesis. I appreciated all of that incredibly much! Further, I want to thank Dr. Francesca Pellicciotti for enabling and supervising my Master thesis. More thanks go out to the rest of the HIMAL group at WSL, especially to Dr. Evan Miles, who was always open to all of my questions and could help me with many remote sensing issues I faced during my thesis, and to Dr. Thomas Shaw for reading through my thesis. The whole group was very supportive and it was super fun to be part of the group for one year. The highlight was the 3-day fieldwork-trip to Zmutt Glacier. Thanks for taking me with you and showing me how impressive ice cliffs are in real life.

Further, I want to thank the Glaciology Team at the University of Zurich who raised my fascination for glaciers and glacier research. Special thanks to Prof. Dr. Andreas Vieli and James Ferguson who introduced me to debris-covered glaciers.

Lastly, I want to thank my family and friends who always listened to my worries and put me back up when motivation was low. Here, special thanks go out to my fellow students who were responsible for fun lunches and study breaks at Irchel Campus. I was very happy to have people around me facing the same joys, challenges and issues.

# Contents

# List of Figures

# List of Tables

# Introduction

*Figure 1: Ice cliff next to a collapsed conduit on Zmutt Glacier, Oct 2020. Picture by S. Walz.*

Supraglacial debris cover is common worldwide and has an influence on the surface melt rates of glaciers and therefore on their response to climate change (Scherler et al., 2018). In East South Asia, which covers the study area of this thesis, 18.7% of the total glaciated area is covered by debris (Herreid and Pellicciotti, 2020). A thin debris layer leads to increased surface melt due to the lower albedo, whereas a thicker layer of more than a few centimetres insulates the ice because of longer distance for heat conduction and leads to a reduction in melt rate (Nicholson et al., 2018; Östrem, 1959). Nevertheless, recent large-scale studies have shown that the surface lowering of debris-covered glaciers is similar to bare-ice glaciers at the same elevation and therefore tended to be higher than expected and predicted in glacier melt models (Anderson et al., 2021; Brun et al., 2019; Gardelle et al., 2013; Kääb et al., 2012; Pellicciotti et al., 2015). This observation can be explained by reduced emergence velocities (Brun et al., 2018; Vincent et al., 2016; Anderson et al., 2021), by the presence of thin debris which increases ablation due to a decrease in albedo (Gardelle et al., 2013; Fyffe et al., 2020) or by the presence of supraglacial ice cliffs and ponds, which are frequently observed on debris-covered glacier tongues (Pellicciotti et al., 2015; Salerno et al., 2017).

There is no consensus definition of an ice cliff, but we define it here as an exposed ice surface on an otherwise continuously debris-covered glacier. They are generally steeper than 30°, a threshold above which debris would otherwise accumulate (Herreid and Pellicciotti, 2018; Figure 1). These supraglacial features on debris-covered ablation zones act as energy windows that transfer heat directly onto the glacier ice because they are directly exposed to incoming shortwave radiation as well as incoming long wave radiation from the surrounding debris (Buri et al., 2016).

Ice cliffs have been suggested to be important contributors to the mass balance of debris-covered glaciers. A number of studies estimated the contribution of ice cliffs to glacier melt for only a few glaciers in HMA, the Alps and Alaska. To have an idea of the melt contribution of ice cliffs, it is useful to not only look at the percentage that ice cliffs account to the ablation but also to look at the enhancement factor which considers the total area of ice cliffs and therefore directly shows the enhanced ablation due to the presence of ice cliffs. Furthermore it allows a direct comparison of different glaciers (Brun et al., 2018). On Ngozumpa Glacier, ice cliffs represent only 5% of the debris-covered area but account for 40% of the ablation (Thompson et al., 2016). The ice cliffs therefore enhance the ablation by a rather high factor of 8. On Changri Nup Glacier, ice cliffs cover 7 to 8% of the glacier tongue and contribute 22 to 25% to the total ablation which gives an enhancement factor of approximately 3.1 (Brun et al., 2018). On Lirung Glacier, ice cliffs and ponds cover 8% of the observed area and are responsible for 24% of the total melt (Immerzeel et al., 2014) and the glacier melt is therefore enhanced by a factor of 3. King et al. (2020) found that the ice cliffs on Khumbu Glacier accounted for 35% of melt from January to October 2015 by covering 13.2% of the study area. This leads to an enhancement factor of 2.7. Beside these glaciers in High Mountain Asia, Mölg et al. (2019) found that the ice cliffs on Zmutt Glacier in the Alps only contribute to 5% of the total ablation because of their small total area (1.1% of the debris-covered area in 2013) and the relatively thin debris layer. Even if these numbers are low, the enhancement factor of 4.5 is quite high compared to the other numbers. On Kennicott Glacier in Alaska the ice cliff area is 11.7% of the debris-covered glacier tongue and the ice cliffs are responsible for 26% of the melt at the glacier tongue (Anderson et al., 2021). The ablation is therefore enhanced by a factor of 2.2 even if the ice cliffs cover a larger area than for the upper glaciers. The numbers of this paragraph are summarized in Table 1.

*Table 1: Relative ice cliff area, melt contribution and enhancement factor of previously investigated glaciers in former studies.*

| *Glacier* | Rel. Cliff area [%] | Melt contribution [%] | Enhancement factor |
|---|---|---|---|
| **Ngozumpa** | 5 | 40 | 8.0 |
| **Changri Nup** | 7-8 | 22-25 | 3.1 |
| **Lirung** | 8 | 24 | 3.0 |
| **Khumbu** | 13.2 | 35 | 2.7 |
| **Zmutt** | 1.1 | 5 | 4.5 |
| **Kennicott** | 11.7 | 26 | 2.2 |

These studies are done on a local scale for only a few glaciers and we therefore do not know whether they are representative for larger regions. To improve the understanding of the processes governing the distribution and evolution of ice cliffs and their contribution to melt it is important to conduct research into the distribution of ice cliffs at larger scales (Kneib et al., 2021b; Steiner et al., 2019; Watson et al., 2017; King et al., 2020). Past studies which tried to assess the distribution of ice cliffs at larger scale from remote sensing data highlighted difficulties in the mapping of these features (Watson et al., 2017; Steiner et al., 2019; Herreid and Pellicciotti, 2018; Kneib et al., 2021b). These ice cliff mapping methods and their difficulties are further explained in Chapter 2 of this thesis.

Kneib et al. (2021b) developed two new methods, a spectral curvature and a spectral unmixing approach, to map ice cliffs semi-automatically from multispectral satellite images. This thesis focuses on the linear spectral unmixing with scale (LSU-s), because Kneib et al. (2021b) documented good results and transferability for coarser satellite data. Additionally, this approach does not require further datasets such as a digital elevation model (DEM). The linear spectral unmixing with scale (LSU-s) is further developed within this thesis to apply it to PlanetScope data, which we chose because of its high spectral and temporal resolution and because it is freely available. The adapted cliff mapping method is then used to map the distribution of ice cliffs in HMA for post-monsoon season 2019 at a larger scale including 23 glaciers. The reason for choosing this season is that the chance of cloud- and snow-free satellite images is highest during this period of the year. Furthermore, the resulting ice cliff distribution is analysed by calculating the relative ice cliff area and brought into relation with potential driving factors such as driving stress, longitudinal gradient, glacier velocity, strain rates and glacier mass balance.

## 1.1 Objectives and Research Questions

This Master thesis has three main aims. The first aim is to test the transferability of the semi-automated LSU-s approach developed by Kneib et al. (2021b) to PlanetScope multispectral images.

Secondly, we aim to map the distribution of ice cliffs from PlanetScope satellite images at four different sites (one site = four to seven glaciers) spread across HMA for the post-monsoon season 2019 using the further adapted semi-automated cliff delineation method.

The third aim is to compare the resulting ice cliff distribution with different glacier characteristics to identify the driving factors of ice cliff distribution.

To reach these objectives, the following research questions are addressed in this Master thesis:

1. Transferability of LSU-s to PlanetScope images:
    - 1.1 Can PlanetScope satellite images be used to map ice cliffs on several glaciers across HMA in a semi-automated way?
    - 1.2 How do the PlanetScope images need to be adapted so that the delineation method is transferable over multiple satellite scenes?
    - 1.3 How consistent are the spectral end-members across the study sites?
2. Distribution of ice cliffs across the study sites in HMA:
    - 2.1 Is the ice cliff distribution consistent over the whole study area?
    - 2.2 What is the ice cliff density for each glacier and how does it differ across HMA?
3. Potential ice cliff driving factors:
    - 3.1 How does the ice cliff density calculated per glacier correlate with different glacier characteristics at the scale of the whole study area?
    - 3.2 How does the ice cliff density calculated across elevation bands for each glacier correlate with glacier characteristics at the scale of a study site?
    - 3.3 How does the ice cliff density calculated across elevation bands for each glacier correlate with glacier characteristics at the scale of the whole study area?

# Background

This chapter explains the importance of glacier research in High Mountain Asia. Subsequently, the current state of ice cliff research is given. This contains the description of previously used ice cliff mapping methods as well as current scientific understanding about potential drivers of ice cliff distribution.

## 2.1 Glacier Research in High Mountain Asia

Glacier research in HMA revolves around two main topics: The water availability and glacier-related hazards such as glacier lake outburst floods or glacier collapses. Because the ice cliff research is embedded in the research of water supply, this chapter ignores glacier-related hazards.

### 2.1.1 Glacier Melt Contribution to Water Availability

Glaciers in HMA generate melt water which contributes to the water supply of the worldwide most vulnerable river basins regarding climatic, societal and environmental changes (Miles et al., 2021; Immerzeel et al., 2020). This glacier melt water covers the basic water supply for approximately 221 million people living in one of the worlds most densely populated areas (Pritchard, 2019; Viviroli et al., 2020). The populations in HMA are particularly vulnerable to drought, during which time glacier melt water is a resilient water source as they act as high elevation storage of freshwater which is released during the warmer months. In a drought year, the monthly peak of glacier melt in the Aral Basin contributes to up to 87% of the river inputs, whereas the contribution is 77% in an average year. Therefore, the glaciers in HMA have an important role in the protection of the downstream populations from severe drought effects (Pritchard, 2019). With further climate warming in the $21^{st}$ century, there will be a projected loss of half of the glacier ice volume in HMA (Kraaijenbrink et al., 2017). This glacier ice shrinkage will firstly lead to an increase in glacier runoff and a peak in melt water in the next decades, but will subsequently lead to an ultimate decline in glacier melt water production at the end of the $21^{st}$ century (Pritchard, 2019; Huss and Hock, 2018; Rounce et al., 2020). Nevertheless, Ragettli et al. (2016) stated that the impact of climate change to runoff cannot be generalized. But they as well modelled an increase in glacier runoff and peak flows, followed by a decrease for the Langtang region in HMA. However, they found a compensation of this decrease by a projected increase in precipitation. Overall, it can be said that climate warming and the associated deglaciation in HMA lead to significant changes to the society living in this region (Hock et al., 2019). It is therefore essential to do further research on the health and sustainability of these glaciers and their reaction to the current $21^{st}$ century warming (Miles et al., 2021; Kraaijenbrink et al., 2017; Bolch et al., 2012).

### 2.1.2 State of HMA's Glaciers

Miles et al. (2021) calculated the specific mass balance for 56% of the total area of HMA's glaciers larger than 2 $km^2$.They found that around 40% of the ablation of these glaciers is unsustainable with the current climatic conditions and cannot be balanced by accumulation. This leads to a glacier volume loss of 23% by 2100 without considering further climate warming. Rounce et al. (2020) modelled a slightly higher mass loss of 29 ± 12% by the end of the century. Hugonnet et al. (2021) calculated a mass loss of -0.22 *m w.e.* per year from 2000 to 2019. Beside these volume changes, Bolch et al. (2012) stated a retreat in length for most of HMA's glaciers since the mid-$19^{th}$ century. The mass losses and retreat of the Himalayan glaciers result in an increase of debris cover, a potential decrease in glacier velocity and the growth of glacier lakes and lead to a positive feedback. An exception to that is observed in the Karakoram, where large glaciers have been stable or even advanced in the recent years. This contradictory behaviour of the glaciers in the Karakoram is not only detected for glacier length but also for the mass balance, where a slight mass gain could be observed. In the literature, this occurrence is referred to as the Karakoram anomaly (Bolch et al., 2012; Azam et al., 2018; Farinotti et al., 2020). Since there is a strong increase in the thinning of glaciers in HMA, the thickening in the Karakoram region has also changed to a thinning of these glaciers in the late 2010s. This observation suggests the end of the Karakoram anomaly (Hugonnet et al., 2021; Bhattacharya et al., 2021).

The changes of the summer monsoon-affected Himalayan glaciers can be partly explained with their sensitivity to temperature rise. Increasing temperature leads to less solid precipitation in summer and extends the melting period. In contrast, the advance and mass gain of the Karakoram glaciers was considered to come from increased solid winter precipitation and decreasing summer temperatures in this region. Nevertheless, the regional temperature increase starts to affect these glaciers as well (Bolch et al., 2012; Azam et al., 2018; Bhattacharya et al., 2021).

### 2.1.3 Current Knowledge Gap

Currently, glacier research in HMA is still limited, because the access to the high-altitude glaciers of HMA is difficult and time-consuming and therefore field measurements of accumulation and ablation are done for only a small sample of relatively low-altitude glaciers (Miles et al., 2021; Bolch et al., 2012). Another challenge beside this extreme topographical relief is the diversity of climatic conditions which leads to speculative forecasts (Bolch et al., 2012). On account of these points, the spatial and also the temporal coverage of the understanding of the Asian glaciers remain weak (Azam et al., 2018). The lack of local observations leads to considerable uncertainty in future forecasts of glacier changes in HMA (Hock et al., 2019). Furthermore, the limited and biased knowledge of the local patterns of mass gain and loss for most of the glaciers in HMA leads to a bias in the current glacier change models because internal dynamics and surface-climate interactions such as debris cover are ignored (Rounce et al., 2020). One way to address these uncertainties without direct glaciological measurements is the use of remote sensing methods.

## 2.2 Ice Cliff Research

To fully understand the controls on glacier mass balance in HMA, it is crucial to gain a greater understanding about the spatio-temporal changes in morphological characteristics such as supraglacial debris cover or avalanches (Brun et al., 2019). Because approximately 30% of the ablation area in HMA is debris-covered (Kraaijenbrink et al., 2017), the understanding of the influence of debris at glacier surfaces is a current debate where further investigations at larger spatial scale is needed. Recent large-scale studies showing similar thinning rates of bare-ice and debris-covered glaciers are in contradiction with the insulating effect of debris on glacier ice and therefore with the prediction in recent melt-models (Anderson et al., 2021; Brun et al., 2019; Gardelle et al., 2013; Kääb et al., 2012; Pellicciotti et al., 2015). To find an explanation for this discrepancy, the influence of supraglacial features on debris-covered glaciers such as ice cliffs to ablation was the focus of many previous studies, but they mostly concentrated on individual glaciers (Thompson et al., 2016; Brun et al., 2018; Immerzeel et al., 2014; King et al., 2020; Miles et al., 2018).

### 2.2.1 Ice Cliff Mapping

Ice cliffs are very dynamic features which can rapidly appear, evolve and disappear (Buri and Pellicciotti, 2018; Steiner et al., 2019). To understand their contribution to glacier melt for consideration in melt modelling frameworks, it is therefore important to know their spatial distribution and their temporal evolution. To address this for a whole glacier but also at a regional scale, consistent and transferable ice cliff mapping methods are needed. The main challenges that are faced when developing cliff delineation methods are the need of high resolution imagery, the varying surface characteristics and steepness of ice cliffs and the transferability to larger scale and different spatial resolutions (Kneib et al., 2021b).

Many recent studies investigating ice cliffs have used manual delineation to identify the cliffs with the help of different datasets. These methods include the delineation of ice cliffs using a combination of DEM elevations and slope and aspect characteristics (Thompson et al., 2016), the derivation of triangulated irregular networks of each ice cliff using terrestrial photogrammetry (Brun et al., 2018) or the manual digitization on the basis of an orthophoto mosaic generated from UAV-collected photos (Immerzeel et al., 2014). The manual identification of ice cliffs is a time-consuming and repetitive task which depends on the expert knowledge of the operator who has to accurately and correctly read different shapes and surface characteristics of ice cliffs. The manual delineation can lead to a delineation bias and related misinterpretation due to inaccurate cliff representations coming from different surface properties and illumination across a scene. Hence, this method can be seen as subjective (Kneib et al., 2021b). To tackle the problem of cliff illumination which can hide parts of the cliff in their own shadow, Thompson et al. (2016) and Watson et al. (2017) developed a cliff identification method where they just delineate the top of the ice cliffs. However, this method ignores the ice cliff geometries which can be important to interpret the evolution of ice cliffs in space and time.

The need of less time consuming and also more objective delineation methods was approached with the development of semi- or fully automated methods. Herreid and Pellicciotti (2018) and Reid and Brock (2014) took the slope of the ice cliffs as classification criteria. This method relies on the assumption that debris cannot accumulate above a certain slope threshold. The basis for this cliff classification is a digital elevation model (DEM). Because the surface slope of a glacier depends on numerous factors such as the climatic glacier conditions or geomorphological characteristics, it is best to automatise the slope threshold selection. This does not only improve the accuracy of the threshold selection but also the transferability of the method to different glaciers (Herreid and Pellicciotti, 2018). King et al. (2020) took a fine resolution DEM to develop a statistical measurement of relief (SMR) to define ice cliffs. The threshold setting was based on field observations, photographs and satellite images. One disadvantage of these two methods is the dependence on the spatial resolution of the DEM. For the most accurate results, a fine resolution DEM is needed, which can identify steep and narrow ice cliffs as well as potentially overhanging cliffs. These high-resolution DEM are not freely available and the preprocessing is connected with high computational requirements (Kneib et al., 2021b).

Another semi-automated approach to delineate ice cliffs is based on the spectral signature. The goal is to distinguish the spectral signature of ice cliffs from the surrounding debris and water bodies such as supraglacial or proglacial lakes. The challenge of these methods is the large variation in the nature of ice cliffs. Bare-iced cliffs can be very bright whereas cliffs covered with a thin layer of dust are mostly darker than their surrounding (Anderson et al., 2021; Kraaijenbrink et al., 2016). Kraaijenbrink et al. (2016) used object-based image analysis (OBIA) which they applied to UAV data with very high resolution. Mölg et al. (2019) combined OBIA applied to orthophotos with manual cliff delineation. The results of this approach are promising, but in both studies the cliff delineation was just done for a small region of homogeneous ice cliffs. The transferability of this method to other and larger areas and to coarser datasets was therefore not assessed.

Further methods are based on the assumption that multispectral images can be used to semi-automatically map ice cliffs in a transferable and objective way (Kneib et al., 2021b). These methods have evolved from the idea that spectral indices calculated from simple band ratios are a successful way to produce binary maps of different features, such as water bodies (Watson et al., 2018). Anderson et al. (2021) developed an approach which uses the different brightness of cliffs and the surrounding debris to delineate cliffs semi-automatically. The challenge of this approach is to have scenes with little shading. Furthermore, varying debris and ice cliff nature lead to the need of new training sets for every new scene. Another disadvantage of this method is that it is based on the assumption, that ice cliffs are darker than the surrounding debris. This is not always the case as cliffs can be bare ice and therefore brighter than their surrounding or the debris can be wet and therefore darker than the ice cliffs. Kneib et al. (2021b) developed the spectral curvature (SC) method which tackles the varying shape of ice cliff spectra depending on different surface characteristics by classifying ice cliff pixels based on the curvature of their spectra which is not existent for the flat debris spectra. SC worked best for the high resolution Pléiades satellite images and the method is described as transferable from scene to scene.

Considering the possibility to use all the spectral information contained in modern multispectral satellite images, Kneib et al. (2021b) developed another delineation method which uses a linear spectral unmixing (LSU) of the multispectral data. This method decomposes the spectrum of each pixel in a linear combination of previously defined spectral end-members. LSU works well for features with a very mixed signal (Kopačková and Hladíková, 2014) such as ice cliffs. In addition to the LSU, an LSU with scale (LSU-s) was developed by Kneib et al. (2021b) which defines the ice cliffs over a scale factor. This method is further explained in section 5.2 of this thesis. The LSU-s gave the best results for coarser imagery such as Sentinel-2 where it also showed good transferability. Hence, adjustments to this method is in theory not needed when using it in other regions. This Master thesis addresses the transferability of the LSU-s to PlanetScope images and to different study sites.

### 2.2.2 Ice Cliff Driving Factors

Ice cliff mapping is useful to estimate their contribution to glacier melt by comparing their distribution with potential enhancement factors. Furthermore, improving the knowledge of potential ice cliff drivers can contribute to the ongoing debate on the formation and dynamics of ice cliffs. Recent studies have found that different glacier characteristics can be linked to a number of cliff formation mechanisms.

For instance, Benn et al. (2001, 2012) describe the collapse of englacial drainage systems and the associated formation of supraglacial ponds as a driver of ice cliff formation. These collapses are a result of the surface lowering and reduction of the longitudinal gradient of glaciers with a debris-covered tongue due to an inverted ablation gradient. These processes lead to a reduction in glacier velocity and driving stress. The supraglacial ponds can grow rapidly by the melting of the exposed ice cliffs surrounding the ponds or by calving. This melt is 10 to 100 times greater than the sub-debris melt. Mölg et al. (2020) observed the same cliff formation process for some of the ice cliffs on Zmutt Glacier.

However most of the ice cliffs on Zmutt Glacier are located on either side of large cryo-valleys in the high-relief area. These valleys are formed where melt water runoff accumulates and builds a stream. With pronounced meandering of the streams, the ice cliffs grow and enlarge the meanders in multiple directions by ice cliff backwasting (Mölg et al., 2020).

Considering ice cliffs occurring where the surface slope exceeds the friction angle of debris, Reid and Brock (2014) describe the opening of crevasses as another possible mechanism of ice cliff formation. The south-facing cliffs flatten with time because the upper section receives direct sunlight whereas the north-facing cliffs maintain their angle. They therefore have differential melt rates.

Finally, ice cliff formation was observed by debris slumping on an oversteepening slope (Sharp, 1949; Moore, 2018; Westoby et al., 2020). Fine debris that is prone to high melt rates can fluidize with the melt water and can already slump on shallow slopes, whereas thicker and coarser debris is less sensitive and remains stable on steeper slopes (Moore, 2018).

# Study Area

The automatic delineation of ice cliffs and the analysis of their distribution is done for four sites spread across the Himalaya, each covering four to seven glaciers (Figure 2). The choice of the study sites can be justified by the selection of regions including well-studied glaciers and the coverage of the Himalayan climatic gradient. This gradient can be described as following: The rather dry climate in the north-western Himalaya is driven by the westerlies which bring winter precipitation whereas the more humid climate in the south-eastern Himalaya is influenced by the summer monsoon (Bolch et al., 2012; Azam et al., 2018).

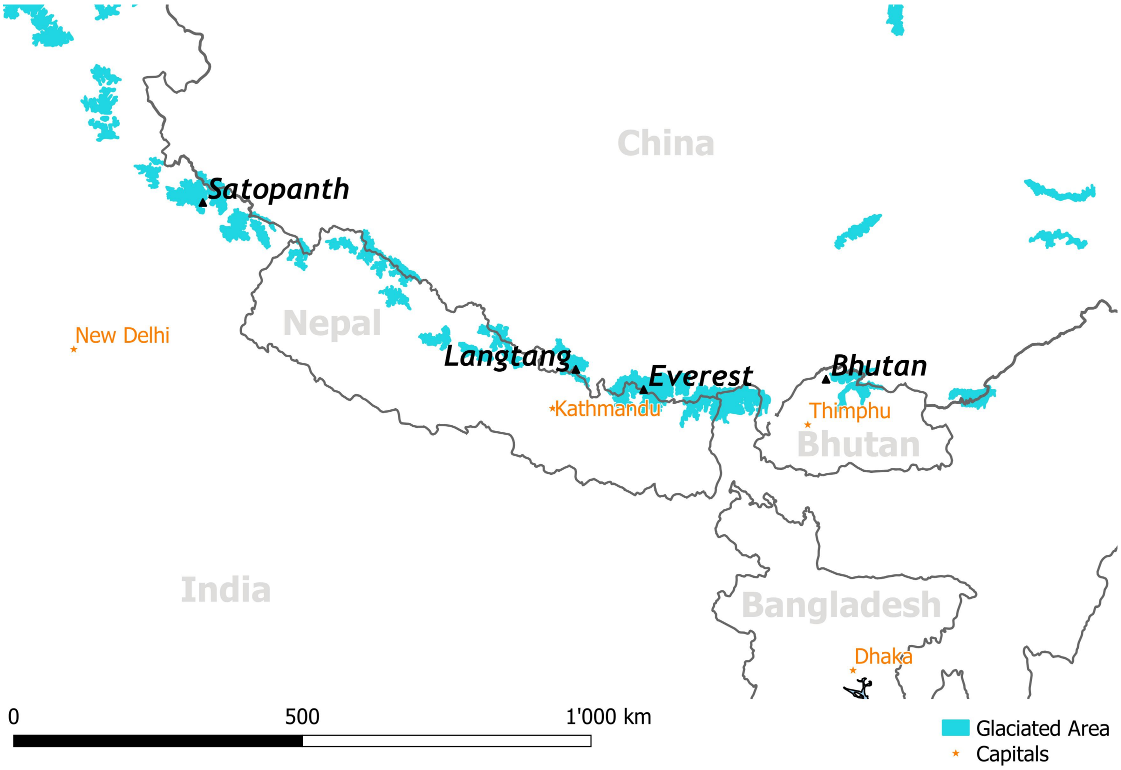

*Figure 2: Study sites in the Himalaya used for the automatic ice cliff delineation.*

## 3.1 Study Sites

The study site around Satopanth Glacier lies in the North of the Indian state Uttarakhand in the northern Himalaya. In comparison to the other sites, it is located most northern of the climatic gradient. This site is chosen because Kneib et al. (2021b) tested the LSU-s on Satopanth (S1) and Bagirath Kharak Glacier (S2). Gangotri Glacier (S4) as part of this site was previously studied by Bhattacharya et al. (2016). To simplify the names of the glaciers, they are named S1 to S4 in this study (Figure 3).

Langtang site lays in the Langtang National Park in central Nepal. This study site was for example investigated by Pellicciotti et al. (2015) who studied mass balance changes and by Steiner et al. (2019) and Buri et al. (2021) who examined supraglacial ice cliffs and ponds and their influence on the mass balance. The ice cliffs of Langtang Glacier (L3) were mapped by Kneib et al. (2021b) and investigated by Kraaijenbrink et al. (2016). The most studied glacier at this site is Lirung Glacier (L1) (Sakai et al., 2002; Immerzeel et al., 2014; Buri et al., 2016; Buri and Pellicciotti, 2018; Steiner et al., 2021). This study site covers six glaciers simplified to L1 to L6.

Bhutan site covers six glaciers in the Himalayan mountains of Bhutan. They are named B1 to B6 in this thesis. This site is well researched, especially with regard to glacier lakes and the hazard of glacier outburst floods (Naito et al., 2012; Fujita et al., 2008).

The Everest site lays in the Mount Everest region of the Himalaya in Nepal. The study site includes seven glaciers to the west of Khumbu Glacier (K1 to K7). This region is well researched in previous studies. Benn et al. (2012) for example studied the response of debris-covered glaciers to recent warming. Salerno et al. (2017) examined the debris-covered glacier anomaly. Ngozumpa Glacier (K5) was already investigated in numerous studies (Benn et al., 2001; Thompson et al., 2016; Nicholson et al., 2018; Herreid and Pellicciotti, 2018).

## 3.2 Test Sites

To calibrate the automated ice cliff mapping to PlanetScope imagery, initial tests are done for three test scenes which are taken on earlier dates than post-monsoon 2019: Satopanth (S1/S2), Langtang (L3) and Lunana Glacier (B4). In the case of Satopanth and Langtang, these glaciers are chosen because the manually delineated ice cliff outlines were already available from Kneib et al. (2021b). We chose Lunana Glacier because there is an available Pléiades image to manually outline the ice cliffs of this glacier.

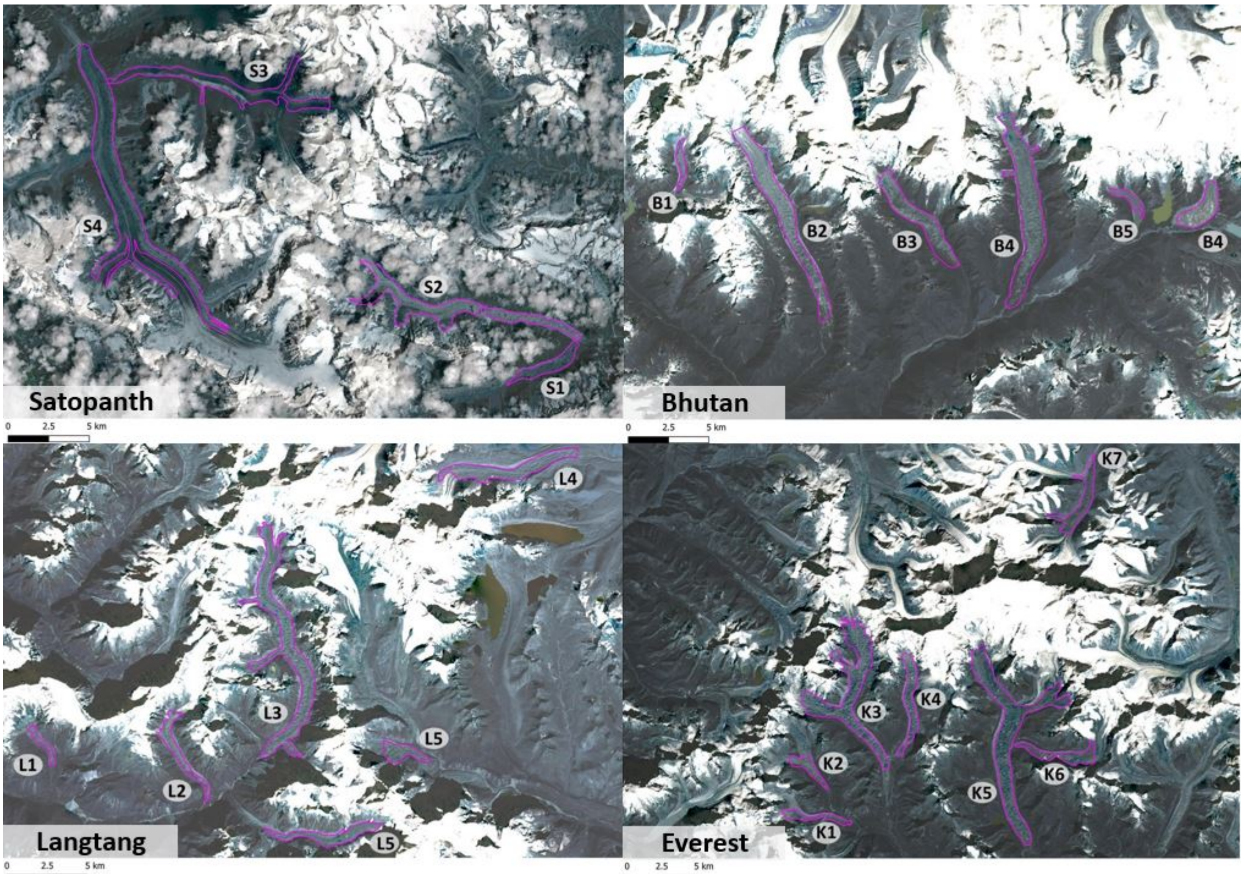

*Figure 3: All investigated glaciers illustrated with the debris-covered outlines used for this study. Background: true-colored Landsat-8 scenes from post monsoon season 2019.*

# Data

This chapter describes the data which is used for the semi-automated ice cliff mapping as well as for the analysis of the ice cliff distribution and its drivers at the four study sites.

## 4.1 Data for Ice Cliff Mapping

### 4.1.1 PlanetScope Imagery

To automatically generate the ice cliff maps for the four sites in HMA, PlanetScope imagery (Planet Team, 2017) is used in this study. The PlanetScope satellite images are collected from a group of approximately 130 individual Dove CubeSat satellites which cover the entire land surface of the Earth every day. The PlanetScope images have a spatial resolution of approximately 3.7 $m$ (altitude dependent) in the four multispectral bands blue, green, red and near-infrared (NIR) (Planet Labs Inc., 2021)(Table 2). For this study, orthorectified surface reflectance 4-band PlanetScope images are used because the spectral resolution of these images is similar to the one of the Pléiades satellite images (Airbus Defence & Space, 2021) for which the LSU-s approach was developed. Furthermore, the PlanetScope data is freely available with an academic licence on the Planet Explorer and can be downloaded with a monthly quota of 5000 $km^2$. PlanetScope images are the most appropriate multispectral images for this study, because of their high spatial resolution, which allows the mapping of a detailed ice cliff distribution, their high repeat time and simple and free access over a large area. These characteristics make them more appropriate to map ice cliffs at a larger scale than Pléiades images, which are not freely available, and Sentinel-2 images which have a considerably lower spatial resolution of 10 $m$. The PlanetScope images used in this thesis are listed in Table 3.

### 4.1.2 Debris-Covered Glacier Outlines

The glacier outlines used in this study are taken from the Randolph Glacier Inventory (RGI) 6.0 (RGI Consortium, 2017). The RGI 6.0 is a global inventory of glacier outlines which were derived from Landsat imagery acquired between 1986 and 2016. The quality of the RGI outlines is limited because of the manual selection of Landsat images over a long time range (Herreid and Pellicciotti, 2020). Therefore, a manual adaptation and improvement of the outlines is needed because the glaciers have further retreated and to get rid of artefacts. Furthermore, the glacier outlines have to be cut to the debris-covered area of the investigated glaciers because this study only focuses on the glaciated areas which are covered with debris.

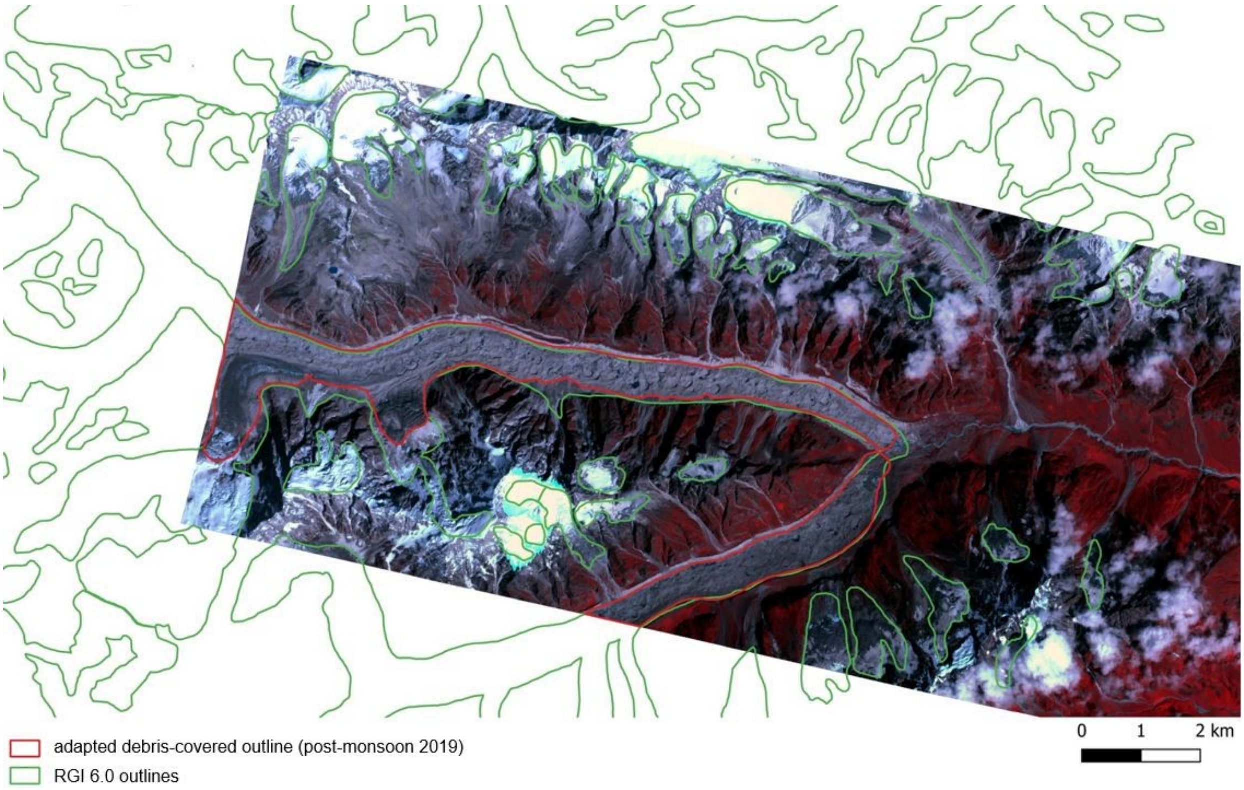

*Figure 4: The RGI 6.0 outline compared to the adapted debris-covered glacier outline used in this study. Background: false-color composite (NIR, red, green) PlanetScope image.*

### 4.1.3 Pléiades Imagery

For the adaptation and calibration of the LSU-s to run it with PlanetScope images, Pléiades satellite images are used. The multispectral orthoimages have a spatial resolution of 2 $m$ and sample the blue, green, red and NIR spectrum with four bands (Airbus Defence & Space, 2021) (Table 2). The images were stereo-processed using either Rational Polynomial Coefficients (RPCs) with AMES stereo pipeline for Langtang and Lunana Glaciers (Shean et al., 2016; Beyer et al., 2018; Kneib et al., 2021b) or the Semi Global Matching (SGM) correlation algorithm for Satopanth Glacier (Hirschmüller, 2008; Kneib et al., 2021b). In a second step, the orthoimages were corrected to surface reflectance to get rid of atmospheric effects and the directional aspect of the raw images (Airbus Defence & Space, 2021; Kneib et al., 2021b). Table 3 contains the acquisition dates of the Pléiades images used for the calibration of the mapping method.

As an example, the Pléiades and PlanetScope scenes of the tree test sites and the debris-covered glacier outlines used for the ice cliff mapping can be found in Figure 5.

### 4.1.4 Shapefiles of Manually Delineated Ice Cliffs

To calibrate the LSU-s approach before applying it to all glaciers in the study area, the ice cliff mapping was done for PlanetScope images of the test sites where available Pléiades images allowed for manually deriving a validation dataset. The shapefiles of the manually delineated ice cliffs of Satopanth and Langtang Glaciers are taken from Kneib et al. (2021b). The manually delineated ice cliffs of Lunana Glacier are generated for this study based on the corresponding Pléiades satellite image and are checked by a second operator so that we are confident in the accuracy of the manual cliff outlines. The shapefiles of these three glaciers consist of a sample set of 30 to 40 manually delineated ice cliffs.

### 4.1.5 Landsat-8 Imagery

This study uses a Landsat-8 satellite image of each site to bias correct the PlanetScope satellite images so that they can be directly compared with each other within one site. This step needs to be done because the sensors acquiring PlanetScope images are not identical and the images are not robust in terms of spectral equivalence (Planet Labs Inc., 2021). We chose Landsat-8 images because they are less prone to spectral inequalities as they are collected by only one satellite. The Landsat-8 satellite has a repeat cycle of 16 days and the resulting images have a size of 185*180 *km* with a spatial resolution of 30 *m*. The size of the Landsat-8 images therefore covers a whole study site. Landsat-8 scenes have nine spectral bands but for the bias correction of the PlanetScope scenes, only bands 2 to 5 which correspond to the four spectral bands of the PlanetScope Satellite images are used (USGS, 2021) (Table 2). Landsat-8 images can be directly downloaded from USGS Earth Explorer, where they are freely available. The Landsat-8 scenes used for this study are listed in Table 3.

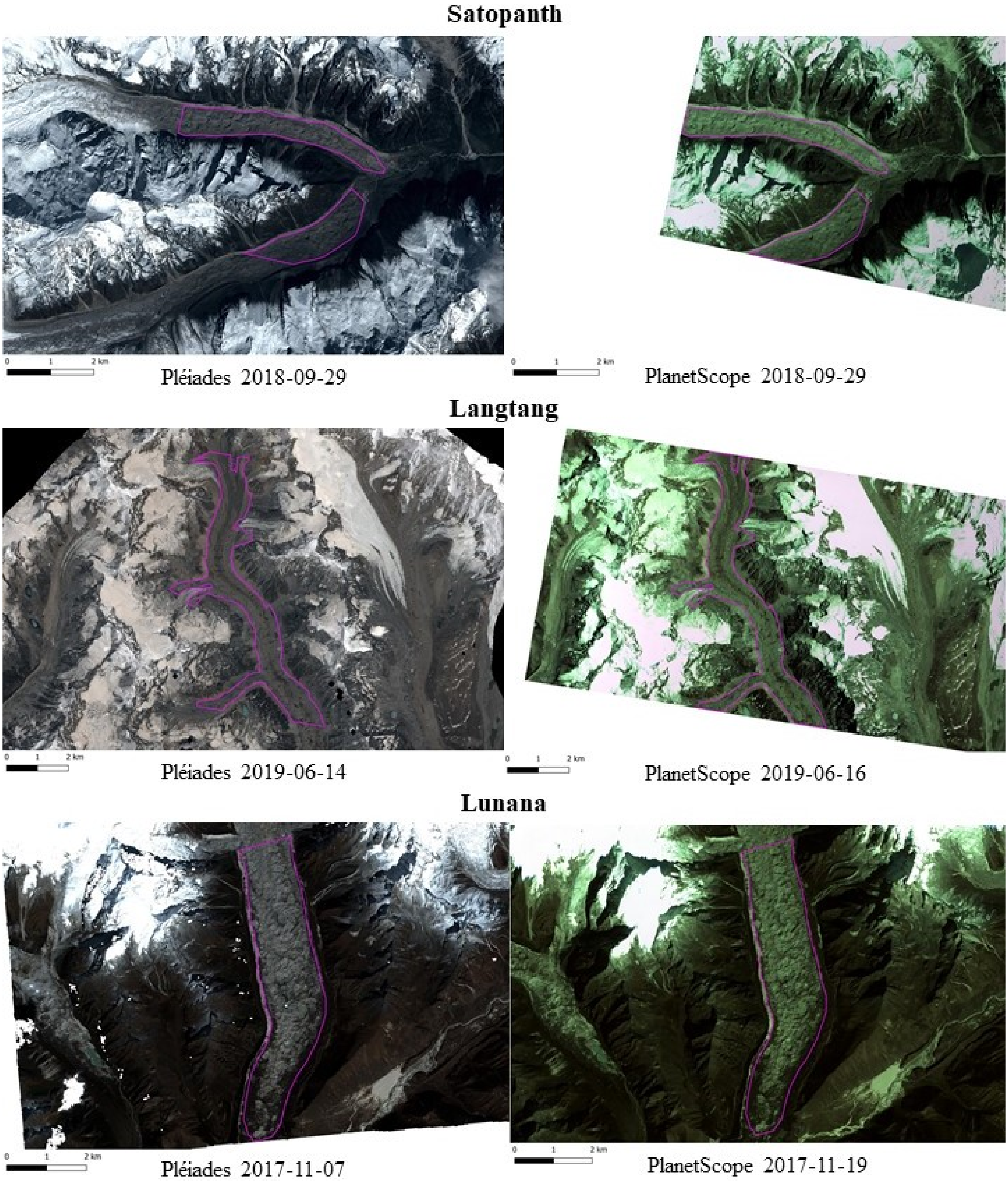

Satopanth

Pléiades 2018-09-29

PlanetScope 2018-09-29

Langtang

Pléiades 2019-06-14

PlanetScope 2019-06-16

Lunana

Pléiades 2017-11-07

PlanetScope 2017-11-19

*Figure 5: True-colored Pléiades and Planetscope images of test scenes with acquisition dates. Pink: debris-covered outlines cropped to the extents of the PlanetScope scenes.*

*Table 2: Wavelengths of the four bands used in this study for PlanetScope, Pléiades and Landsat-8 imagery.*

| | **PlanetScope** | | **Pléiades** | | **Landsat-8** | |
|---|---|---|---|---|---|---|
| *Band Type* | *Band Number* | *Wavelength [nm]* | *Band Number* | *Wavelength [nm]* | *Band Number* | *Wavelength [nm]* |
| blue | 1 | 464 - 517 | 1 | 460 - 530 | 2 | 450 - 510 |
| green | 2 | 547 - 585 | 2 | 520 - 600 | 3 | 530 - 590 |
| red | 3 | 650 - 682 | 3 | 610 - 690 | 4 | 640 - 670 |
| NIR | 4 | 846 - 888 | 4 | 770 - 890 | 5 | 850 - 880 |

*Table 3: Aquisition dates of all multispectral data used in this study.*

| | | *Number of scenes* | **PlanetScope** | **Pléiades** | **Landsat-8** |
|---|---|---|---|---|---|
| *Purpose* | | | ice cliff mapping | calibration of method | bias correction of PlanetScope |
| *Test sites* | | | | | |
| Satopanth | | 1 | 2018-09-29 | 2018-09-29 | 2018-10-02 |
| Langtang | | 1 | 2019-06-16 | 2019-06-14 | 2019-06-12 |
| Lunana | | 1 | 2017-11-19 | 2017-11-07 | 2017-11-24 |
| *Study sites* | | | | | |
| Satopanth | Satopanth | 1 | 2019-09-10 | | |
| | Gangotri | 2 | 2019-10-15 | | 2019-08-11 |
| | Bagirath Kharak | 1 | 2019-09-11 | | |
| Langtang | | 4 | 2019-11-20 | | 2019-11-19 |
| Bhutan | | 2 | 2019-11-27 | | 2019-11-14 |
| Everest | | 2 | 2019-11-13 | | 2019-11-12 |

## 4.2 Data for Analysis of Ice Cliff Distribution

The analysis of the ice cliff distribution is based on different datasets which are obtained from previous studies.

The calculation of the driving stress and the longitudinal gradient for each glacier uses the consensus ice thickness estimates from Farinotti et al. (2019), which correspond to the RGI 6.0 outlines and have a resolution of 25 *m*, and the ASTER 3.0 30 *m*-DEM (NASA/METI/AIST/Japan Spacesystems and U.S./Japan ASTER Science Team, 2019). Both these datasets were preprocessed by Miles et al. (2021) who defined a grid for each glacier using local UTM projections and a resolution of 50 *m* for glaciers with an area > 15 $km^2$, 100 *m* for larger glaciers of < 80 $km^2$ and 200 *m* for glaciers with an area larger than 80 $km^2$. The ASTER DEM was reprojected and resampled to the given grid with a cubic spline interpolation. The ice thickness estimates where degraded to the final resolution. The uncertainties of these datasets are not taken into account in this study.

The flow velocity and the strain rates are derived from the mean of the annual glacier flow velocities for the years 2009 to 2018 with a spatial resolution of 240 *m* from the NASA MEaSUREs ITS_LIVE project (Dehecq et al., 2019; Gardner et al., 2020). The reported uncertainties of this dataset are very low and therefore neglected.

The dataset of the specific mass balance (SMB) for each glacier is taken from Miles et al. (2021) and has the same resolution for different glacier sizes as the preprocessed ice thickness and DEM datasets. The SMB per pixel was calculated by solving the continuity equation (Eq. 1). The uncertainty of the SMB values are not considered in this thesis.

$$\frac{\rho_{dH}}{\rho_{H_2O}}\frac{dH}{dt} = \dot{b} - \frac{\rho_{\nabla q}}{\rho_{H_2O}}\nabla * q \tag{1}$$

where:

$\frac{dH}{dt}$ = annual rate of elevation change at the glacier surface

$\dot{b}$ = annual SMB

$\nabla * q$ = annual flux divergence

$\rho$ = density for each quantity

To calculate the ice cliff metrics and potential driving factors per elevation band, a zonal dataset from Miles et al. (2021) is used which divides the area of each glacier in elevation bins based on the glaciers slope distribution. This dataset is generated by smoothing the preprocessed ASTER DEM with a 11*11 Gaussian low-pass filter and segmenting it into 25 *m* elevation bins. These bins are then intersected with a smoothed version of the debris cover datasets provided by Scherler et al. (2018).

# Method Development

## 5.1 Preprocessing of Satellite Scenes

Before running the semi-automatic ice cliff mapping with LSU-s the outlines of the debris-covered glacier areas have to be adapted to the multispectral satellite images and the satellite images have to be cut to the area of interest.

The PlanetScope scenes chosen for the test sites have to fulfill two requirements. Firstly, they have to be near-contemporaneous to the Pléiades images which were used for the manual delineation of ice cliffs. Secondly, they need to be as cloud- and snow-free as possible and no shadows should cover the debris-covered area of the glaciers in order for the ice cliffs to be properly recognised with the LSU-s approach. The latter does also account for the PlanetScope images of the post-monsoon season 2019 which are used for the ice cliff mapping at larger scale. Because PlanetScope images do not have a footprint covering a whole study site, multiple satellite scenes have to be selected for each site. Cloud-, snow-, and shadow-covered areas should also be minimal in the Landsat-8 images used for the bias correction of the PlanetScope scenes. The acquisition dates of all satellite scenes used in this thesis are listed in Table 3.

### 5.1.1 Data Preparation for Bias Correction

In a first step, the debris-covered glacier outlines of the investigated glaciers have to be cut to each PlanetScope scene. Afterwards, the outlines are buffered with a 1000 $m$-buffer because we not only include the glacier area but also non-glaciated areas like moraines, glacier foreland and rock walls beside the glaciers to reach the best possible bias correction. Furthermore, the buffer has to be adapted to exclude areas with potential shadows, cloud- and snow cover of the respective PlanetScope and Landsat-8 scene.

These interfering factors would otherwise falsify the bias correction. To better recognize these factors in the Landsat-8 scenes, the images separated per bands are merged first.

These adapted 1000 *m*-buffer of the debris-covered outlines are then used to cut the PlanetScope and Landsat-8 images to the same extents before running the bias correction.

### 5.1.2 Data Preparation for Ice Cliff Mapping

For the ice cliff mapping with LSU-s the debris-covered glacier outlines have to be cut to the extent of the bias corrected PlanetScope scenes. With this step, potential clouds, snow and shadows of the PlanetScope scenes are already removed from the area of interest. Additionally, the adapted outlines have to be buffered by 66 *m* due to methodological steps which are further explained in section 5.2. Finally, The PlanetScope images are cut to the 66 *m*-buffer before running the LSU-s.

## 5.2 Linear Spectral Unmixing with Scale

The LSU-s approach (Kneib et al., 2021b) which we use for the semi-automated ice cliff mapping in this study decomposes the spectrum of each pixel in a multispectral satellite image as a linear combination of a set of ‘pure’ spectral end-members. Therefore, the reflectance of each spectral band can be expressed with Eq. 2. The coefficients $\alpha_j$ of each pixel are scaled so that the sum is equal to 1. The scaled coefficients can then be interpreted as the abundance of each end-member. Additionally, a scaling factor is calculated for each pixel (Eq. 3) which informs on the absolute reflectance of each pixel relative to the reflectance of the spectral end-members that fit the spectrum of the pixel best. For the automatic delineation of ice cliffs, the spectral end-members of water, bright debris and dark debris are used and chosen directly from a multispectral image at locations where it is assumed that the pixel is composed exclusively of one of these ‘pure’ end-members. On the contrary to the simple LSU, this approach does not include the spectral end-member ice which is not independent of the end-member water. To optimize the results the ice cliffs are separated in two categories: bare ice with a very high reflectance and slightly debris-covered and wet ice cliffs with very low reflectance. The delineation is done with Eq. 4.

$$R(\lambda_i) = \sum_{j=1}^{n} \alpha_j r_j(\lambda_i) \tag{2}$$

where:

$R(\lambda_i)$ = reflectance at central band wavelength $\lambda_i$
$n$ = number of spectral end-members
$r_j(\lambda_i)$ = reflectance values of end-members j at band $\lambda_i$
$\alpha_j$ = coefficients to solve system ($\geq$0)

$$s = \sum_{j=1}^{n} \alpha_j \tag{3}$$

$$Cliffs = (ln(s) < T_{dark})|(ln(s) > T_{bright}) \tag{4}$$

where:

$s$ = scale factor
$T_{dark}$ = scale threshold for the dark cliffs
$T_{bright}$ = scale threshold for the bright cliffs

As part of this method, the supraglacial ponds are delineated using a Normalized Difference Water Index (NDWI) threshold. The NDWI, a metric used to map water bodies (McFeeters, 1996), was used to specifically map supraglacial ponds before (Watson et al., 2018; Miles et al., 2017). It is calculated as following:

$$NDWI = \frac{R(green) - R(NIR)}{R(green) + R(NIR)} \tag{5}$$

where:

$R$ = reflectance value at the given wavelength

The ponds are delineated before the classification of the ice cliffs, because the LSU-s may wrongly map ponds as cliffs otherwise. Figure 6 shows sampled spectra of the end-members used for the LSU-s and a subset of a sample Pléiades image showing the different components used for the ice cliff and pond mapping.

Before running the LSU-s, the debris-covered outlines of the investigated glaciers have to be buffered with 66 *m*, because the scale map used for the ice cliff mapping is filtered using a 33 *m*-window median filter to enhance the patterns in the scale map. Without the buffering, the marginal parts of the areas of interest would not be included in the final ice cliff maps.

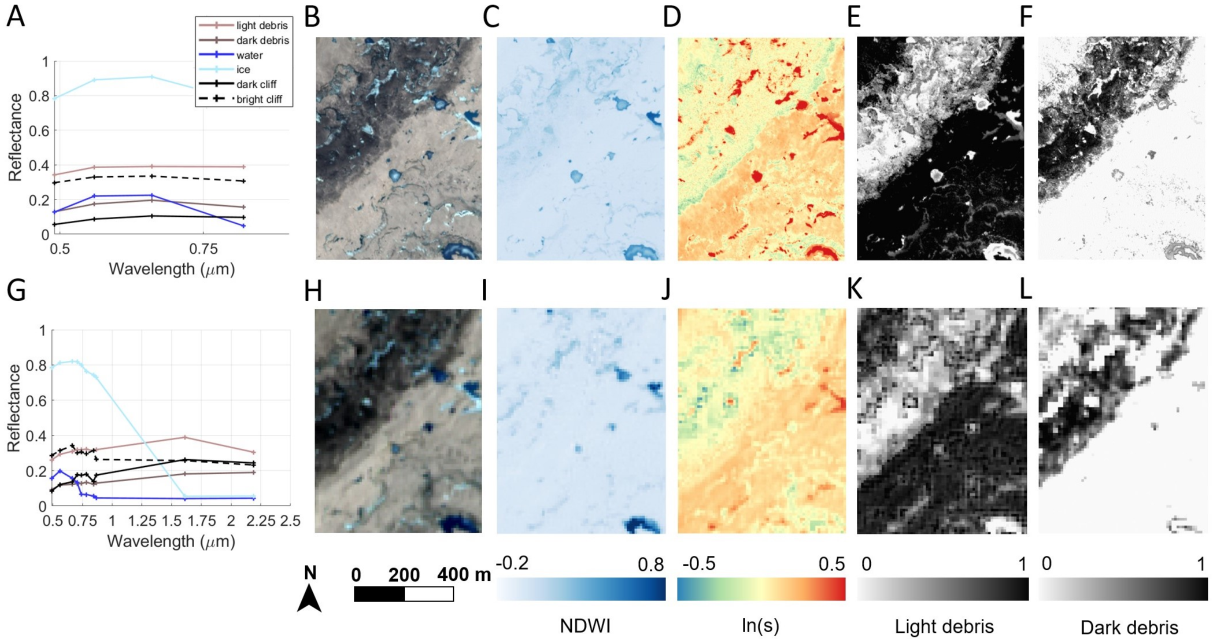

*Figure 6: Sampled spectra of ice, water, light and dark debris from the Khumbu Pléiades (A) and Sentinel-2 (G) images for all bands. The black lines correspond to the spectra of randomly chosen dark (plain line) and bright (dashed line) cliffs. (B). We also show a subset of the Pléiades false color composite image (B) along with its NDWI (C) filtered scale (D) maps, light (E) and dark (F) debris content and the Sentinel-2 false color composite image of the same area (H) with its NDWI (I) filtered scale (J) maps, light (K) and dark (L) debris content (Kneib et al., 2021b, pg. 8).*

## 5.3 Adaptation of LSU-s to PlanetScope Imagery

LSU-s was initially developed for Sentinel-2 and Pléiades images and has to be adapted to PlanetScope satellite data for the approach of this study. For the adaptation of the LSU-s approach, the automated ice cliff mapping is tested on three PlanetScope test scenes covering Satopanth, Langtang and Lunana Glacier with near-contemporaneous Pléiades images (acquisition dates in Table 3). The process of the adaptation of the LSU-s approach is illustrated in a flow chart in Appendix 10.1.1.

### 5.3.1 Coregistration of Planet Test Scenes to Pléiades Images

For the testing of the LSU-s with PlanetScope imagery, the ice cliff maps automatically delineated with PlanetScope images are compared with the manual outlines from the Pléiades. Because the viewing angle of the PlanetScope and the Pléiades satellites can differ, along with the DEM used for projection, the two scenes can be slightly shifted. This shift would falsify the evaluation of the LSU-s method because the ice cliffs in the two scenes would not exactly overlap. Therefore, a coregistration of the PlanetScope image to the Pléiades scene is done using ImGRAFT (Image Georectification and Feature Tracking). ImGRAFT was developed by Messerli and Grinsted (2015) to have a complete and openly available package that involves georeferencing, georectification and feature tracking for terrestrial oblique images. To track features in an image pair, ImGRAFT uses a matching algorithm to find the highest correlation between a defined template area in image 1 within a defined search region in image 2. Knowing the coordinates of the center point of the template area in image 1 and the area with the highest correlation in image 2, the displacement of the two images can be found. This study compares PlanetScope and Pléiades scenes of the test sites with each other. We therefore consider the whole scene including the glaciated area because we assume that the shifts in the images are only due to coregistration problems and not to glacier changes as the images are taken within a few days form one another. After comparing the two images and calculating the horizontal shift, the calculated offset is applied to the PlanetScope image.

### 5.3.2 Initial Testing of LSU-s

Before the initial tests of the LSU-s approach, an end-member set for every test site is generated in QGIS. The end-member sets consist of 10 to 20 sample points for "water", "bright debris" and "dark debris" which are manually identified within the test scenes. Figure 7 shows the spectra of the end-members for the four PlanetScope spectral bands after the bias correction of the satellite images. The initial tests of the LSU-s approach with PlanetScope imagery are done with Langtang and Satopanth test scenes using the Langtang end-member set.

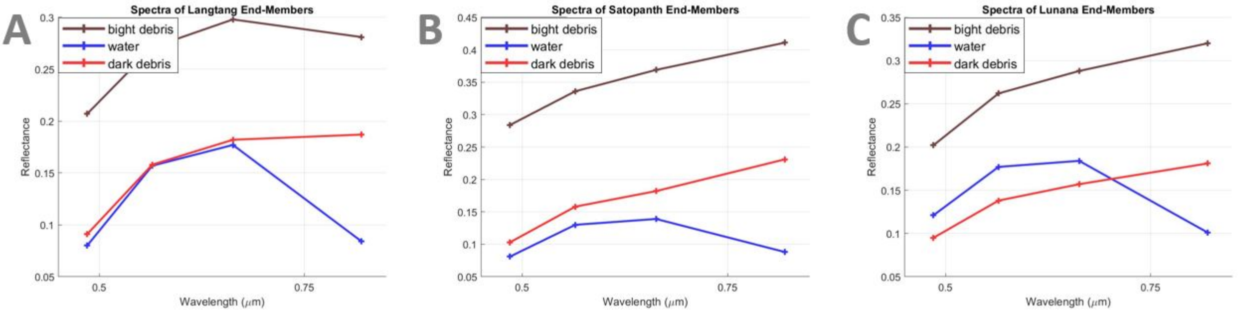

*Figure 7: The spectra of the end-member set of Langtang (A), Satopanth (B) and Lunana (C) test sites after the bias correction of the satellite scenes.*

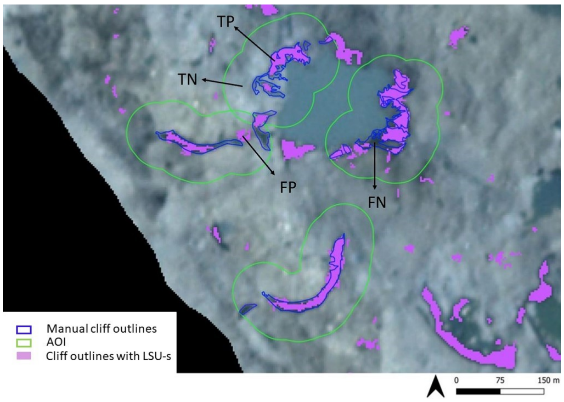

*Figure 8: Example map of Langtang test scene showing the parameter for the Dice calculation. Background: true-colored PlanetScope image.*

The ice cliff distribution of Langtang and Satopanth Glaciers using the Langtang end-members is compared with the manually delineated ice cliffs from the corresponding Pléiades images by calculating the Dice coefficient which is a metric that ranges from 0 to 1 (Eq. 6). The higher the Dice, the better the automatically delineated ice cliffs overlap the manually delineated cliff outlines (Kneib et al., 2021b). The calculation of the Dice does just consider a 50 $m$-buffer around the main manual delineated ice cliffs instead of the whole debris-covered glacial area. This limited area of interest is chosen small enough, so that all ice cliff features inside the buffer can be manually mapped, and big enough so that not only the ice cliffs but also the surrounding debris and water faces are included to best possibly validate the automatically delineated ice cliffs. To find the scale thresholds which give the best results, the LSU-s is run for multiple values of $T_{dark}$ (0.18 to 0.39) to find the threshold set which generates the highest Dice value.

$$Dice = \frac{2TP}{2TP + FP + FN} \tag{6}$$

where:

$TP$ = Number of true positive pixels
$FP$ = Number of false positive pixels
$FN$ = Number of false negative pixels

The Dice value for the resulting ice cliff map of the Langtang test scene is 0.5360. This value is higher than 0.5 and does therefore meet our requirements. Satopanth test scene has a lower Dice of 0.4310 (Figure 9). We aim for Dice values higher than 0.5 considering the Dice equation. When solving the equation to TP we get $TP = 0.5FP + 0.5FN$. With a Dice of 0.5, the true positive pixels are therefore at least the same amount as half of the sum of the false positive and false negative pixels.

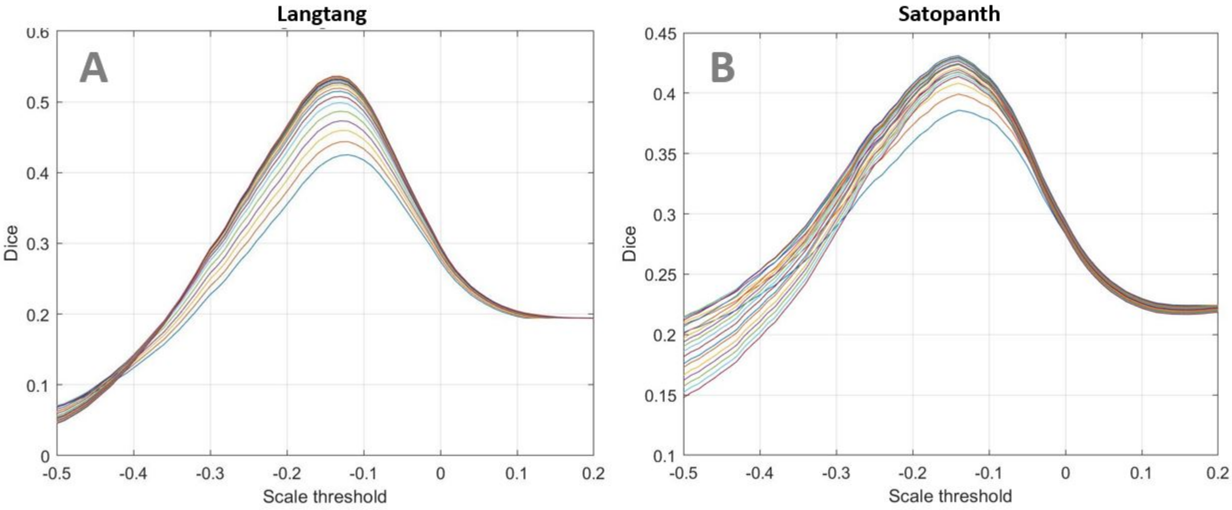

*Figure 9: Dice values for multiple scale thresholds of the Langtang (A) and Satopanth (B) test scenes. X-axis shows $T_{bright}$, differently colored lines show $T_{dark}$.*

The Dice value of the Satopanth test scene can be improved by taking the local end-members for the unmixing of the satellite image. This shows that the spectra of the end-members is not transferable between the two sites due to a spectral difference in the PlanetScope scenes. In order to automate the ice cliff mapping to use it for multiple sites across HMA, it is essential that the same spectral end-member set and the same scale thresholds can be used for all sites . This only works if the PlanetScope scenes are spectrally as identical as possible. Therefore we developed a method to bias correct the PlanetScope satellite images.

### 5.3.3 Bias Correction with Empirical Quantile Mapping

The bias correction of the PlanetScope images is done with empirical quantile mapping (EQM). This method was used in previous research of climate models to correct the biases in the distribution of a modelled variable by comparing it to an observational distribution of the same variable (Feigenwinter et al., 2018; Cannon, 2018; Enayati et al., 2021). This study applies the EQM to the histograms of the PlanetScope scenes with the goal of generating spectrally more equivalent images.

We bias correct the PlanetScope images to Landsat-8 images which are more consistent due to the image acquisition with a single satellite. The two satellite scenes have to cover the same extent. In this case this is the adapted 1000 *m*-buffer around the debris-covered outlines. For the EQM, only Landsat-8 spectral bands 2 to 5 are used, because these bands correspond to the four PlanetScope bands RGB and NIR. Before running the bias correction the pixel values of the Landsat-8 scene have to be changed from digital numbers to real surface reflectance by applying the rescaling coefficients to every band so that they can be directly compared to the pixel values of the PlanetScope scenes. Afterwards, the pixel values are divided into 1000 quantiles and the quantiles of the PlanetScope image are adjusted to these of the Landsat-8 image so that the histograms of the four bands are the same (Figure 10).

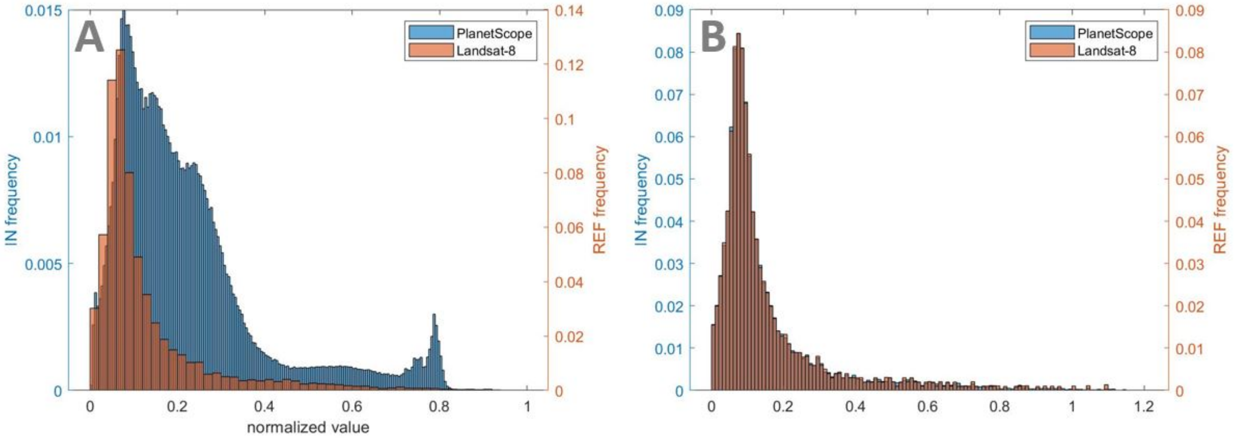

*Figure 10: Sample histograms of one spectral band of a PlanetScope and a Landsat-8 scene covering the same extent before bias correction (A) and after bias correction with EQM (B).*

The bias correction is tested with three Satopanth scenes which overlap each other. The EQM is done with the same Landsat-8 image covering all three scenes. Figure 11 shows the bias corrected PlanetScope images. It can be observed that the images are visually more equivalent than the original images because the image margins are less visible and the colors match (Figure 11).

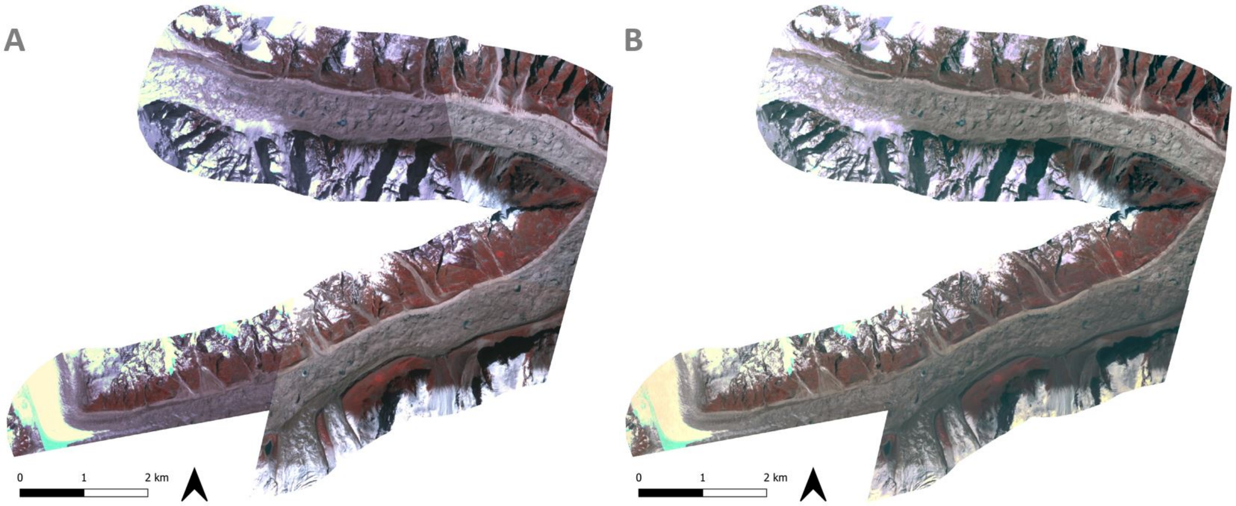

*Figure 11: False-color composite (NIR,red,green) PlanetScope images of Satopanth (A), bias corrected false-color composite PlanetScope image of Satopanth after EQM (B).*

The bias correction of the Langtang and the Satopanth test scenes considerably improved the Dice values. Using the Langtang end-members for Satopanth results in a Dice of almost 0.55. Furthermore, the Dice value of the Langtang test scene is higher than 0.6 using Satopanth end-members for the unmixing of the satellite image.

Looking at the resulting ice cliff maps for Satopanth and Langtang test scenes, many very small cliffs can be recognized. To improve the semi-automated mapping, we just consider ice cliffs that are at least 10 pixels (or 90 $m^2$ considering the spatial resolution of 3 $m$ for the PlanetScope images). This decision can be justified with the findings of Salerno et al. (2012) which consider a pixel size of 10 $m$ as appropriate to correctly describe glacier surfaces. This step is therefore done to decrease uncertainties in the resulting cliff distributions. The Dice value for the Langtang and Satopanth test scenes further improved when ignoring all these small ice cliffs.

### 5.3.4 Calibration of the LSU-s Parameters

To find the end-member set and thresholds which give the most adequate cliff distributions for all the test scenes, a cross comparison is performed. We test every end-member set and every threshold set on all three scenes. Table 4 shows the resulting Dice values for the test runs. To find the best fitting end-member and threshold set, the Dice values were ranked from 1 (lowest value) to 27 (highest value) and the sum of the ranks per end-member and threshold set is calculated. In a last step, these sums are ranked again from 1 (highest sum) to 9 (lowest sum). The end-members of Satopanth and the threshold set of Langtang with rank

1 give the best results over all the test scenes and are therefore used for the automated ice cliff mapping in this study.

*Table 4: Dice values for test scenes using every end-member and threshold set.*

| | *End-Members:* | **Satopanth** | | | | | | **Langtang** | | | | | | **Bhutan** | | | | | |
|---|---|---|---|---|---|---|---|---|---|---|---|---|---|---|---|---|---|---|---|
| | *Thresholds:* | **Satopanth** | **R** | **Langtang** | **R** | **Bhutan** | **R** | **Satopanth** | **R** | **Langtang** | **R** | **Bhutan** | **R** | **Satopanth** | **R** | **Langtang** | **R** | **Bhutan** | **R** |
| *Scenes:* | **Satopanth** | 0.5795 | 21 | 0.5751 | 20 | 0.5658 | 16 | 0.5320 | 9 | 0.5262 | 7 | 0.5312 | 8 | 0.4450 | 3 | 0.4177 | 1 | 0.4398 | 2 |
| | **Langtang** | 0.5913 | 26 | 0.6120 | 27 | 0.5804 | 22 | 0.5194 | 5 | 0.5716 | 19 | 0.5197 | 6 | 0.4754 | 4 | 0.5895 | 25 | 0.5675 | 17 |
| | **Bhutan** | 0.5409 | 10 | 0.5440 | 11 | 0.5564 | 14 | 0.5880 | 23 | 0.5681 | 18 | 0.5880 | 23 | 0.5515 | 13 | 0.5503 | 12 | 0.5596 | 15 |
| | **Rank Sum** | | 57 | | 58 | | 52 | | 37 | | 44 | | 37 | | 20 | | 38 | | 34 |
| | **Rank** | | 2 | | 1 | | 3 | | 6 | | 4 | | 6 | | 9 | | 5 | | 8 |

## 5.4 Ice Cliff Mapping of all Study Sites

After the adaption of the LSU-s approach to PlanetScope imagery, the ice cliffs of all four study sites representing a total of 23 glaciers can be semi-automatically mapped using the Satopanth end-member set and Langtang thresholds. The process of the ice cliff mapping with LSU-s is illustrated in a flow chart in Appendix 10.1.2.

Visually checking the resulted ice cliff maps with the PlanetScope images, it can be observed that overall too many pixels are classified as ice cliffs. Figure 12 shows that many of the classified cliffs cannot obviously be recognized as ice cliffs in the ln(scale) map. There are especially many small cliffs which do not show the typical shapes of ice cliffs which are lateral cliffs positioned perpendicular to the flow line, longitudinal cliffs positioned along the flow line and partially or completely circular cliffs (Steiner et al., 2019). To improve the ice cliff maps, we want to keep the cliffs, where the absolute ln(scale) value is approximately higher than 0.35 (Figure 12).

### 5.4.1 Post Processing with Object Classification

For the improvement of the ice cliff maps, we use object classification. Where an ice cliff is mapped with the LSU-s, it is highly likely, but not sure, that there is a real ice cliff. In this step we consider the ice cliffs as objects and the goal is to get rid of the false positive cliffs. Therefore, we take the mean absolute ln(scale) values of the mapped ice cliffs and define a threshold. All the cliffs which have a lower mean value than the threshold are eliminated from the ice cliff distributions. This post processing method concerns identified cliffs with a mean value close to the used scale thresholds which are not likely to be real ice cliffs for example.

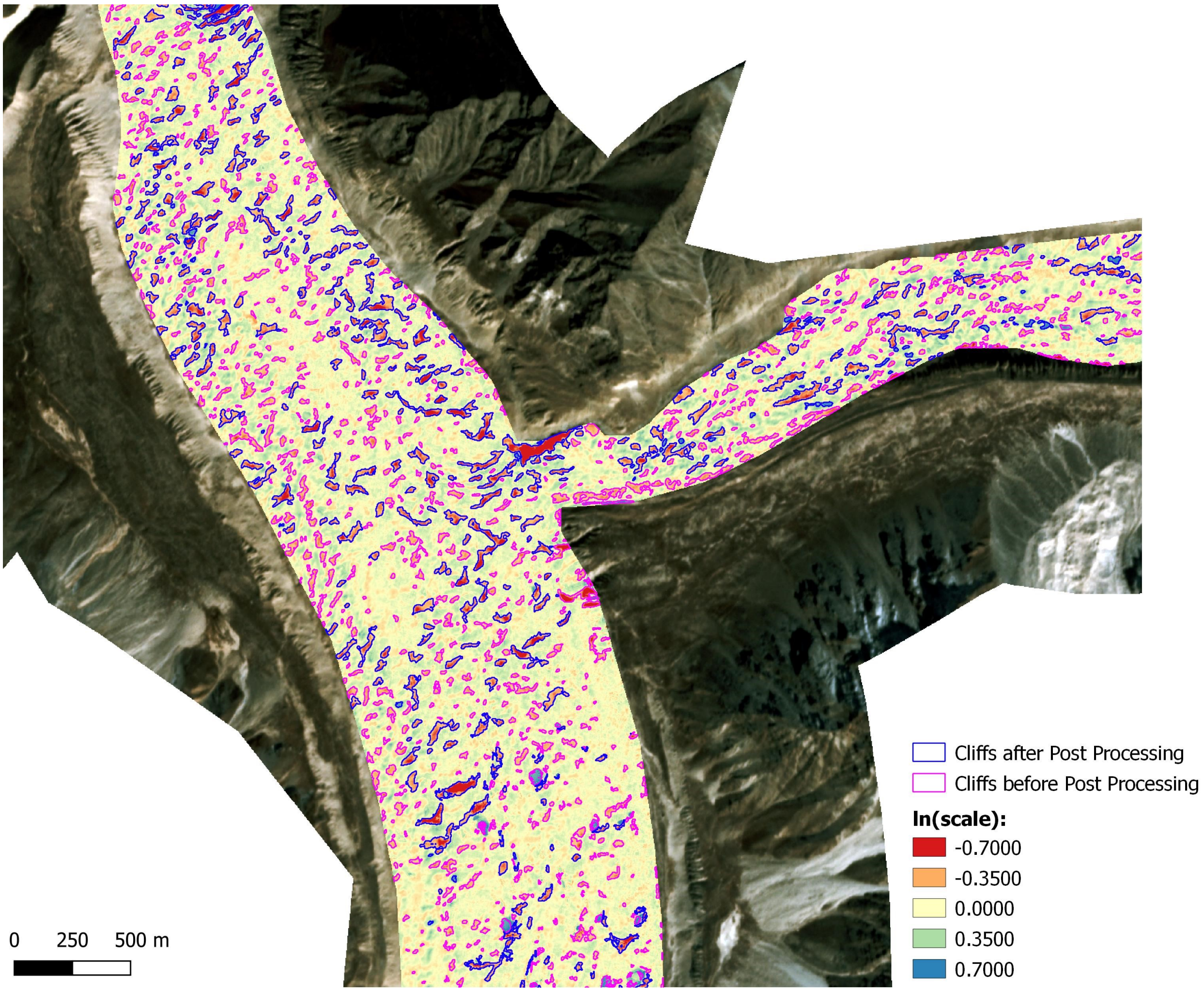

*Figure 12: Ice cliff distribution of Gangotri Glacier (S4) before and after post processing.*

### Threshold Definition

To define the threshold, we look at the histograms and scatterplots of the mean absolute ln(scale) values of the automatically delineated ice cliffs of the three test scenes (Figure 13). The object means are plotted as histograms per object but also per pixel to consider how many pixels actually are affected from the post processing. Figure 13 shows that it is a challenge to find an appropriate threshold. Looking at the histograms and the scatterplot of Satopanth test scene, a threshold of 0.25 would eliminate most of the small cliffs. The histograms of Langtang test scene would assume that a threshold of 0.25 is too high, but considering the scatterplot, it would also just eliminate small ice cliffs with an area smaller than 230 pixels. Considering Bhutan test scene, 0.25 seems to be an appropriate threshold.

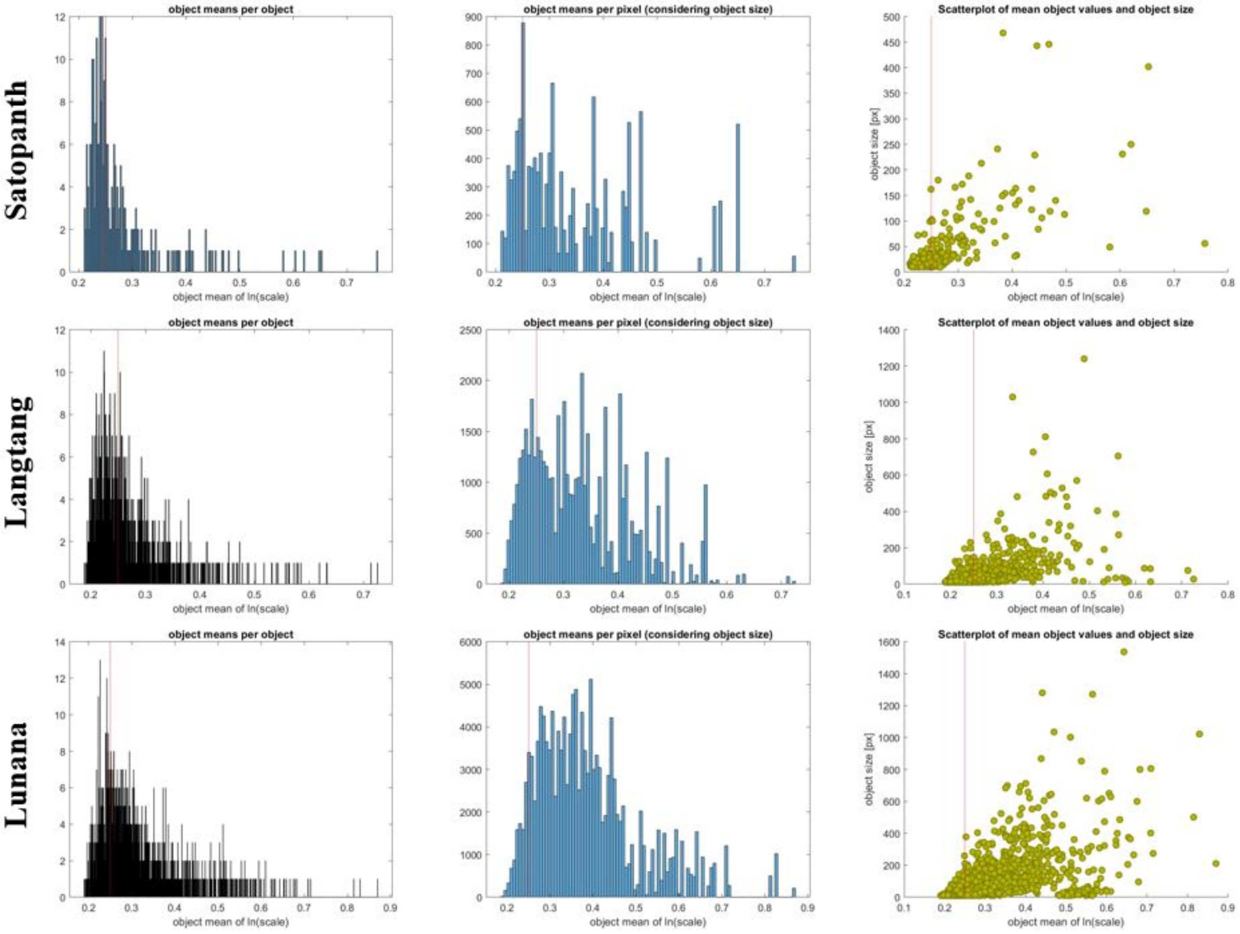

*Figure 13: Histograms and scatterplots of the mean absolute ln(scale) object values. Red lines indicate a threshold of 0.25.*

In a next step, scatterplots (Appendix 10.2) for all study sites are created to see if a threshold of 0.25 is appropriate for all the scenes. Considering these scatterplots and the ice cliff maps themselves, we recognized that a threshold of 0.25 is too low for some of the scenes and a higher threshold of 0.3 would give better results. Because the goal of this study is to have the best possible ice cliff distributions which can be compared with different glacier characteristics, we decided to chose separately for each scene, if a threshold of 0.25 or 0.3 is appropriate. After the post processing a final manual adaption of the ice cliff distributions is done in QGIS to get rid of wrongly classified cliffs at the glacier margins, which are part of the moraine or shadows from the steep rock walls surrounding the glaciers, and wrongly classified ponds.

## 5.5 Analysis of Ice Cliff Distribution

To compare the ice cliff distributions of the 23 glaciers with different glacier characteristics to find potential driving factors, the ice cliff metrics and the glacier characteristics have to be calculated per glacier as well as per elevation band.

### 5.5.1 Calculation of Ice Cliff Metrics

The resulting ice cliff map at each glacier is used to calculate the ice cliff area and the ice cliff density. These values are computed over the whole glacier and across elevation bands. To get the ice cliff area over the debris-covered area of the glacier which we use for the calculation of the ice cliff density, the sum of the pixels classified as ice cliffs is multiplied by the pixel size (9 $m^2$). To get the density, the ice cliff area is divided by the debris-covered area of the glacier (Eq. 7). Furthermore, the zonal datasets from Miles et al. (2021) are used to calculate the ice cliff density per elevation band for each glacier.

$$\rho_{cliff} = \frac{n_{cliff} * s}{n_{dc} * s} \tag{7}$$

where:

$\rho_{cliff}$ = ice cliff density

$n_{cliff}$ = number of pixels classified as ice cliffs

$n_{dc}$ = number of pixels of debris-covered area

$s$ = pixel size (= 9 $m^2$)

### 5.5.2 Calculation of Glacier Characteristics per Glacier

To see how the ice cliff density correlates with potential driving factors, the following glacier characteristics are computed for each glacier: driving stress, longitudinal gradient, glacier flow velocities, compressive and extensive strain rates and specific mass balance.

Driving stress is calculated along the main flow line of the glacier using Eq. 8. The driving stress along the flow line is then interpolated to the whole glacier area. In a last step, the mean driving stress over the whole glacier is calculated.

$$dStr = \rho * g * h * sin\alpha \tag{8}$$

where:

$dStr$ = driving stress
$\rho$ = ice density (= 917 $kg * m^3$)
$g$ = gravitational acceleration (= 9.81 $m/s^2$)
$h$ = ice thickness
$\alpha$ = ice surface slope (calculated along flow line)

The longitudinal gradient along the flow line which corresponds to $\alpha$ from Eq. 8, is derived by fitting a linear regression model between the surface elevation and the distance to the terminus of the glacier to calculate the surface angles. To have one value for each glacier, the mean over the whole glacier is calculated.

The annual glacier flow velocities from ITS-Live (Gardner et al., 2020) have to be cut to the four study sites and resampled to a resolution of 120 $m$ with cubic spline interpolation. Additionally, the coordinate system has to be changed from WGS 84 to the local UTM zones. Afterwards, the flow velocity is cut to each glacier and the mean value over the whole glacier is calculated.

The compressive and extensive strain rates are calculated using the principal strain components in x-,y-, and xy-direction which are derived from the velocity difference along this three directions. The strain rates are calculated with Eq. 9 and 10 which are taken from Nye (1959)(Eq. 4 & 5).

$$lmin = 0.5 * (exx + eyy) - \sqrt{0.25 * (exx - eyy)^2 + exy^2} \tag{9}$$

$$lmax = 0.5 * (exx + eyy) + \sqrt{0.25 * (exx - eyy)^2 + exy^2} \tag{10}$$

where:

$lmin$ = compressive strain rate

$lmax$ = extensive strain rate

$exx$ = strain rate component in x-direction

$eyy$ = strain rate component in y-direction

$exy$ = strain rate component in xy-direction

The specific mass balance for each glacier derived by Miles et al. (2021) is averaged over the debris-covered area of the glacier to have one value per glacier.

After these calculations, the mean of each glacier characteristic is plotted against the ice cliff density to find relations between the datasets. The resulting plots consist of 21 data points, one for each glacier (Figure 16).

### 5.5.3 Calculation of Glacier Characteristics per Elevation Band

To have a more detailed analysis of the ice cliff distribution and find further correlations, the mean of each above mentioned glacier characteristic is calculated per elevation band for each glacier. These mean values are then compared to the ice cliff density of each elevation band. These comparisons are made for each study site separately as well as for the whole study region. Furthermore, the data points which visualise the elevation bands are grouped into quantiles to generate box plots which should clarify the correlation patterns (Figure 22.

### 5.5.4 Exceptions

The ice cliff metrics and glacier characteristics could not be calculated for all of the glaciers. B7 of Bhutan site is not included in the analysis because Miles et al. (2021) did not include this glacier in their study and the datasets are therefore not available. Glacier B2 has to be excluded from the analysis because the dataset containing the elevation zones seems to be erroneous. Therefore, the glacier characteristics calculated for this glacier are inaccurate. Furthermore, S1 and S2 are taken together, because Miles et al. (2021) refer to them as one glacier. This is, because Bagirath Kharak and Satopanth glaciers are seen as one glacier with one ID in the RGI 6.0. The comparison of the relative ice cliff area and the glacier characteristics is therefore done for 21 glaciers in HMA.

# Results

## 6.1 Ice Cliff Distribution

The final ice cliff maps of all the investigated glaciers can be found in Appendix 10.3. As an example, Figure 14 shows the final ice cliff distribution compared to the distribution before the post processing for a section of Gangotri Glacier (S4).

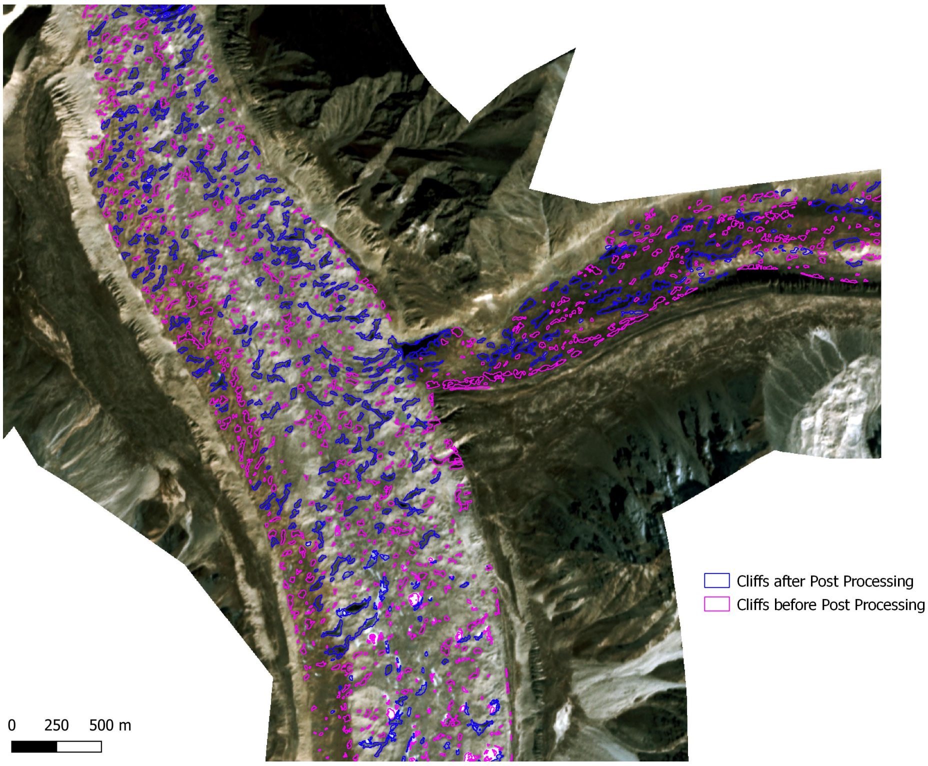

*Figure 14: The ice cliff distribution of a section of Gangotri Glacier (S4). Background: true-colored bias corrected PlanetScope satellite image used for the ice cliff delineation.*

To have a better understanding of the ice cliff distribution of each sample glacier, the scatterplots in Figure 15 show the ice cliff density across elevation bands for each glacier. Additionally, the maps of each glacier showing the ice cliff density for each elevation band can be found in Appendix 10.4. The range of the cliff densities is very high going from 1.2% to 29.2%. The ice cliff densities calculated per glacier range from 3.9% to 17.1% (Table 5). Looking at the average values per study site, Bhutan has the highest cliff density with 12.2%, Langtang the second highest with 10.0%, Everest the third highest with 7.9% and Satopanth the lowest density with 7.4%.

Examining the distribution of ice cliff density, there cannot be seen a clear pattern along the flow line of the glaciers. Most of the glaciers, namely S3, L3, L6, B1, B4, K1-3 and K6, have increasing cliff density along the flow line. Half of these glaciers show an increasing number and size of ice cliffs with increasing cliff density. The other glaciers showing the same density pattern do not have a prominent change in cliff size but just an increasing number of ice cliffs along the glacier flow.

S1/S2 and L5 show an opposite pattern with higher ice cliff density towards the upper part of the glacier. These glaciers show consistent cliff sizes over the whole debris-covered area. It is therefore just the number of cliffs which lead to an increase in cliff density.

L2, L4 and B3 have the highest cliff density in the center of the glacier and the density decreases along and against the flow line. Glaciers L2 and B3 show a similar pattern with larger cliffs perpendicular to the flow line which either have a straight or a circular shape. L4 does not show this phenomena and just has an increased number of ice cliffs of similar size in the middle of the glacier.

L1 and S4 display the lowest cliff density in the center of the glacier. This two glaciers show very different characteristics and are therefore not representative. L1 has a very low number of rather large ice cliffs with different shapes which are well distributed on the glacier whereas S4 has many smaller ice cliffs, which are mostly consistently spread on the debris-covered area. The ice cliff density of S4 is lower in the center of the glacier, because there are just a few cliffs located on the middle moraine of the glacier.

K4-5 and K7 display a random pattern of ice cliff density. Glaciers showing a random distribution of ice cliff density have similarly shaped and sized ice cliffs over the whole debris-covered glacier tongue. K4 is mostly covered with ice cliffs which have a moon-like shape perpendicular to the flow line which appear at the side of ponds. The ice cliffs of K7 are shaped along the flow line. These cliffs are rather large and have a meander-like shape.

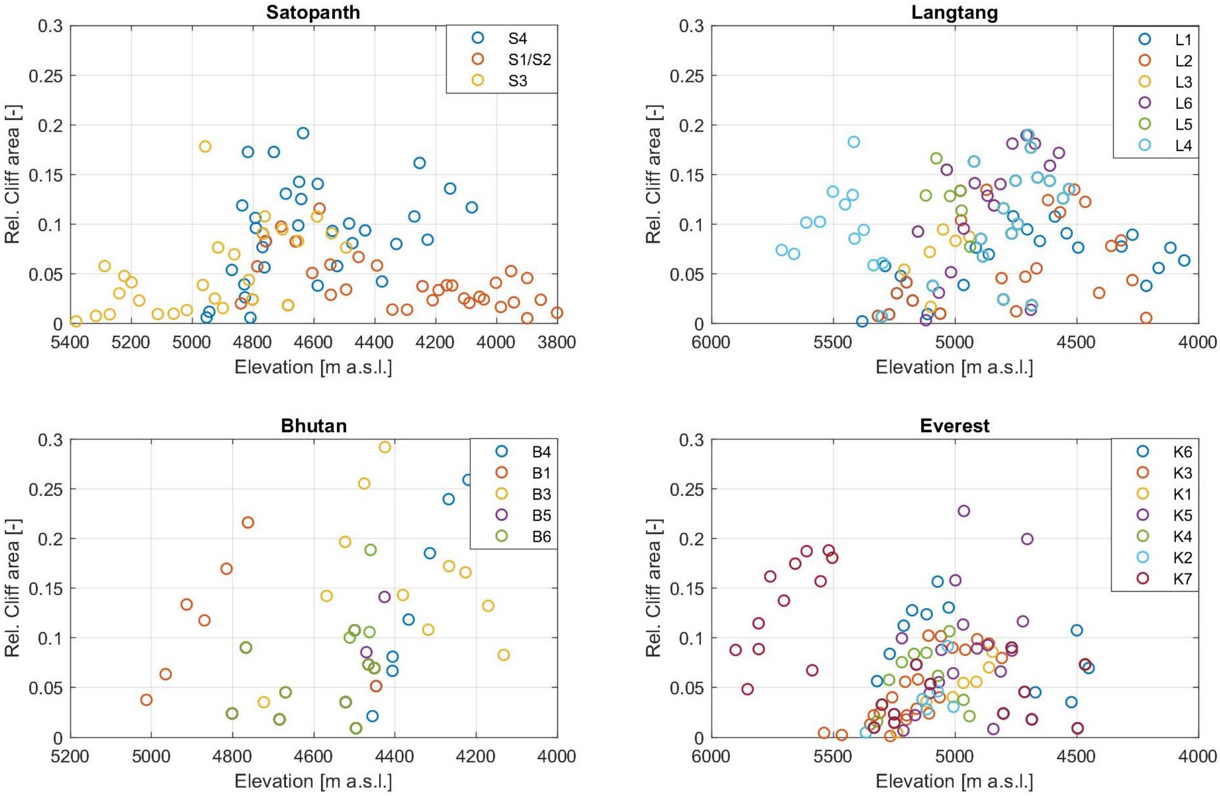

*Figure 15: Cliff density per surface elevation for all glaciers at each study site. The data points represent the elevation bands.*

*Table 5: Relative ice cliff area for each investigated glacier.*

| *Satopanth* | rel. cliff area [-] | *Langtang* | rel. cliff area [-] | *Bhutan* | rel. cliff area [-] | *Everest* | rel. cliff area [-] |
|---|---|---|---|---|---|---|---|
| **S1/S2** | 0.04 | **L1** | 0.06 | **B1** | 0.13 | **K1** | 0.07 |
| **S3** | 0.05 | **L2** | 0.08 | **B3** | 0.16 | **K2** | 0.05 |
| **S4** | 0.13 | **L3** | 0.11 | **B4** | 0.17 | **K3** | 0.05 |
| | | **L4** | 0.1 | **B5** | 0.07 | **K4** | 0.05 |
| | | **L5** | 0.14 | **B6** | 0.06 | **K5** | 0.09 |
| | | **L6** | 0.11 | | | **K6** | 0.11 |
| | | | | | | **K7** | 0.13 |

## 6.2 Comparison with Glacier Characteristics

### 6.2.1 Comparison of Glacier Average Values

To have a first overview of all the sample glaciers in HMA, the ice cliff density is plotted against the glacier average of the glacier characteristics in Figure 16. At first sight, we can say that the data is spread and no clear relation can be detected. Looking at the different sites, the spread is also high. However, the glaciers at Langtang site have a low mean glacier velocity and near zero strain rates compared to the other sites.

Nevertheless, the scatterplot of the longitudinal gradient shows a trend: the larger the longitudinal gradient, the smaller is the cliff relative area. This means there are fewer ice cliffs in steeper debris-covered areas. Other relations can be seen for compressive and extensive strain rates. When the strain rates are higher, the cliff relative area appears to increase quickly. The lowest cliff density seems to be where strain rate are 0. The scatterplots for driving stress, mean glacier velocity and specific mass balance do not show any trend.

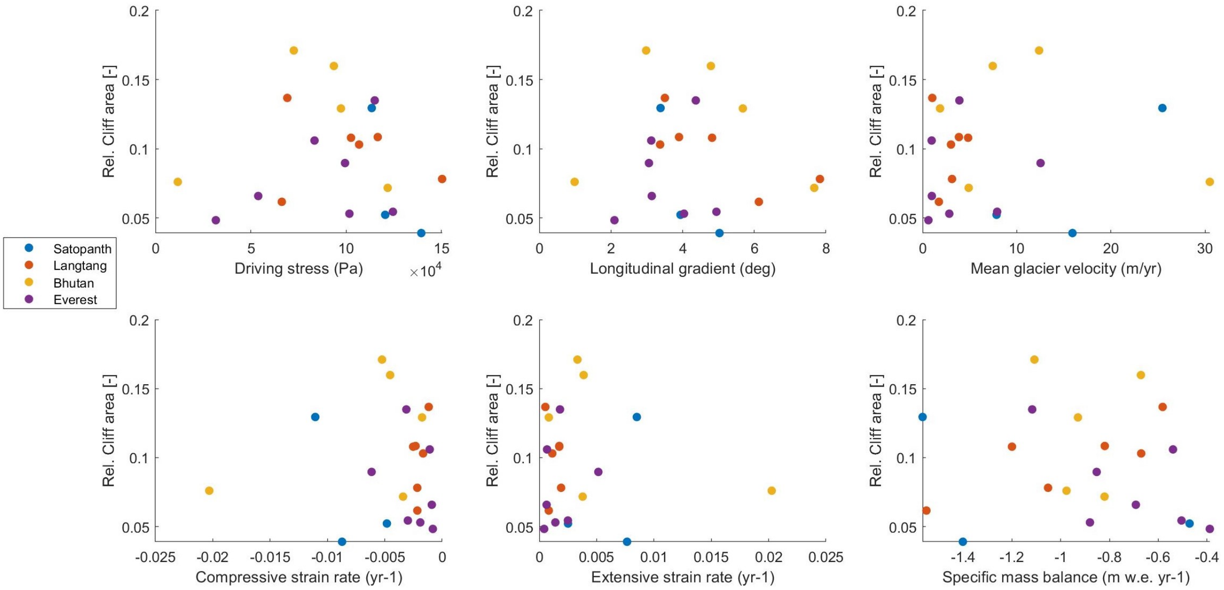

*Figure 16: Scatterplots of the ice cliff density plotted against the glacier characteristics averaged for each glacier.*

### 6.2.2 Comparison of Elevation Band Averages

To have a more detailed look at the data, we look at the local-scale variations at each site and over the whole study area. The data points of the three glaciers at Satopanth site in Figure 17 are spread mostly without very clear trends. Especially for S4, the data is very scattered and makes it more difficult so see clear relations. Only for the longitudinal gradient can a relation with the ice cliff density be recognized. As mentioned before, it seems like the cliff density is lower, where the longitudinal gradient is higher. The relative cliff area decreases faster than the gradient increases.

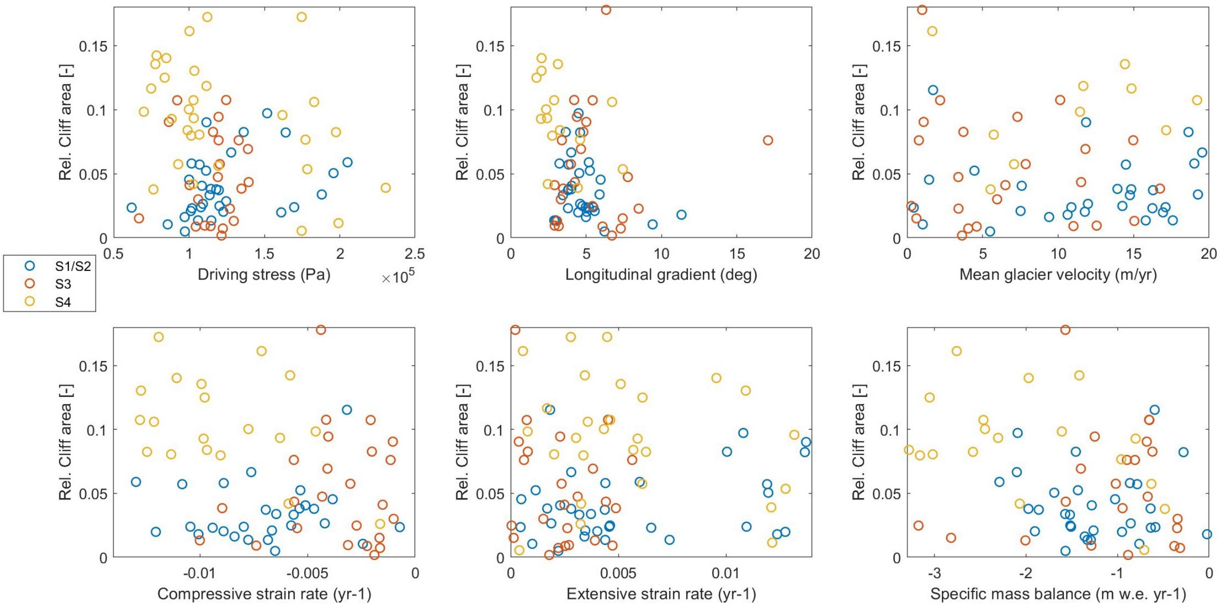

*Figure 17: Scatterplots of the ice cliff density at Satopanth site plotted against the glacier characteristics averaged per elevation band.*

The glaciers at Langtang site in Figure 18 show clearer trends. The scatterplot of the longitudinal gradient confirms the relation described in the previous paragraph. The cliff relative area decreases quickly with an increase of the longitudinal gradient. Furthermore, we can see a relation between the mean glacier velocity and the ice cliff density. As for the longitudinal gradient, the cliff relative area decreases with increasing mean glacier velocity. Another relation is observed for the strain rates. Cliff relative area is highest where the strain rates are near 0. with higher compressive and extensive strain rates, the ice cliff density decreases quickly.

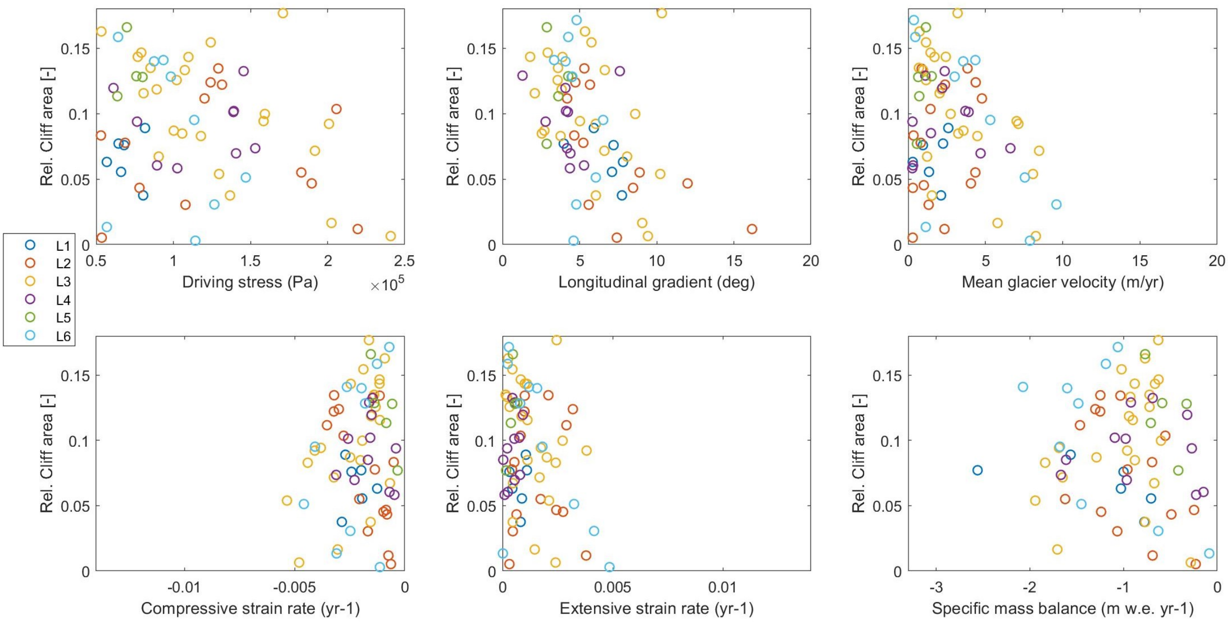

*Figure 18: Scatterplots of the ice cliff density at Langtang site plotted against the glacier characteristics averaged per elevation band.*

The scatterplots of the glaciers at Bhutan site in Figure 19 do not show clear trends. Especially the mean velocity and the extensive strain rate plots have some outliers which obstruct the observation of relations in the datasets. However, a relation between the cliff density and the longitudinal gradient which underlines our assumptions is also visible for the Bhutan site. Furthermore, a relation between the relative cliff area and the driving stress can be found. The ice cliff density decreases with increasing driving stress. The compressive strain rate plot shows the same trend as for the Langtang site. the cliff relative area seems to increase with lower compressive strain rates. Other than for the two previous sites, Bhutan site shows a relation between the specific mass balance and the cliff density. With a higher relative cliff area, the specific mass balance seems to be increased.

The scatterplots of Everest site in Figure 20 show clear trends in the relationship of the ice cliff density and the driving stress, the longitudinal gradient, the mean glacier velocity, and the compressive strain rates. As for Bhutan site, the cliff relative area seems to decrease with an increase of the driving stress. The plot of the longitudinal gradient shows the same relation as for the three other sites: the cliff relative area is lower where the glacier is steeper. Underlining our assumption for the Langtang site, the ice cliff density decreases with higher glacier velocities. Additionally, the cliff relative area increases with lower compressive strain rates. This is also what we saw for Langtang and Bhutan site.

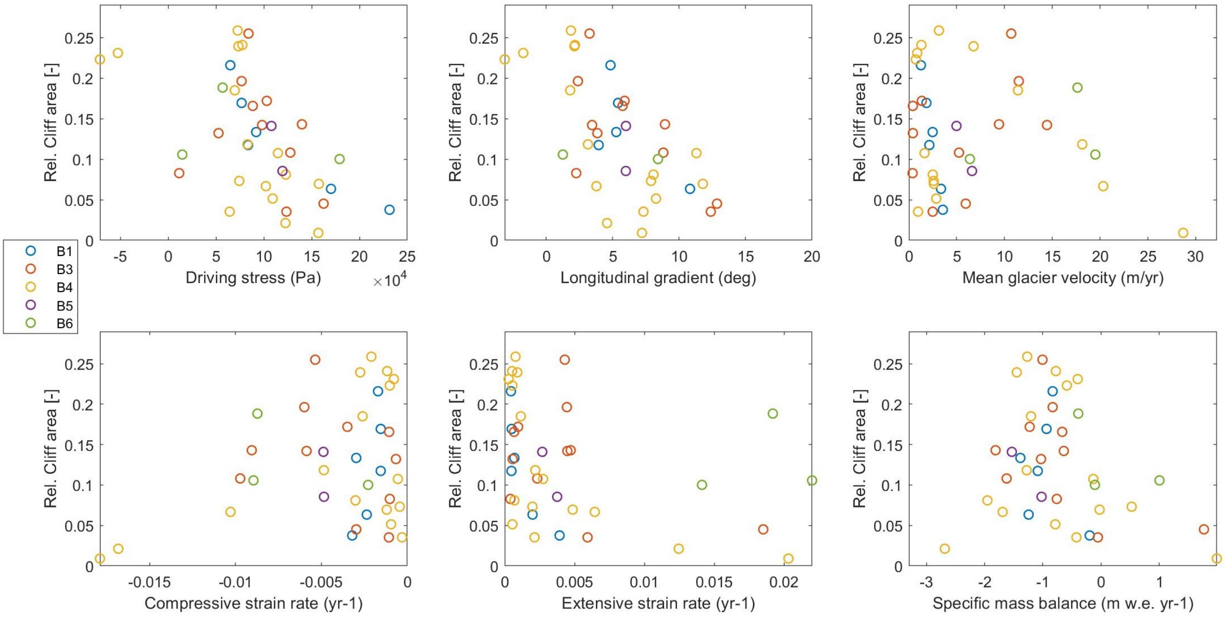

*Figure 19: Scatterplots of the ice cliff density at Bhutan site plotted against the glacier characteristics averaged per elevation band.*

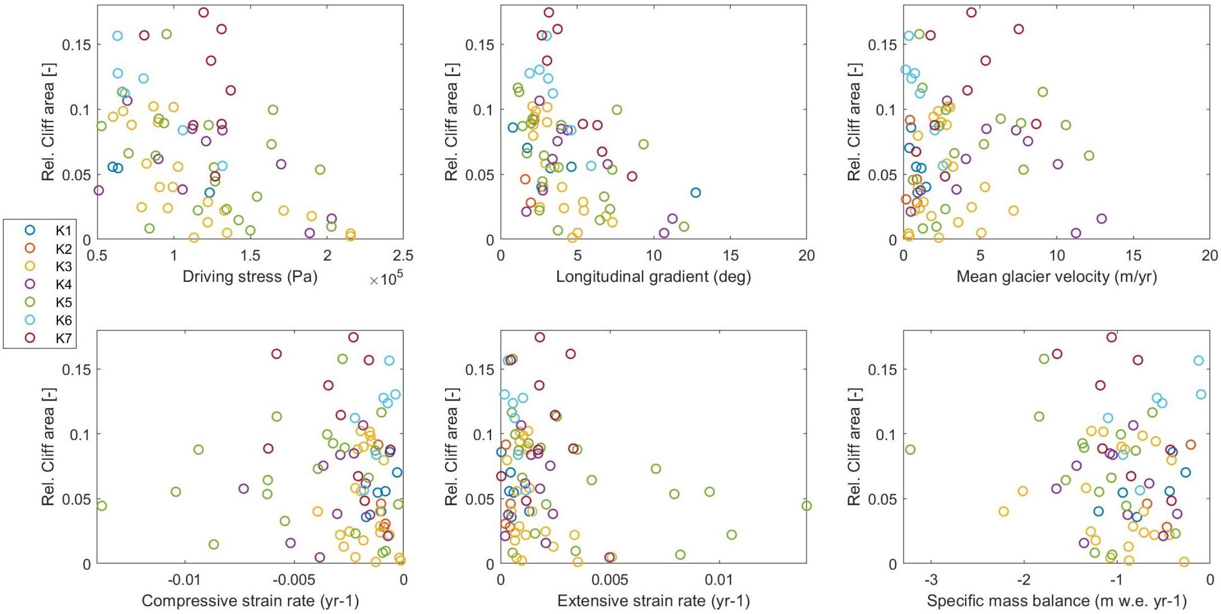

*Figure 20: Scatterplots of the ice cliff density at Everest site plotted against the glacier characteristics averaged per elevation band.*

To see if the detected relations between the relative ice cliff area and the glacier characteristics are also present if we compare the local variations of all the glaciers together, a plot where each data point is an elevation band (Figure 21) and a plot where the data is illustrated in box plots (Figure 22) are generated. The ice cliff density compared to the driving stress shows a clear relation. The cliff density decreases with an increase of the driving stress. The trend for the longitudinal gradient is less clear if we look at the whole study area. But we can still say that there is a tendency that the relative ice cliff area quickly decreases with an increase of the longitudinal gradient. The plot for the glacier flow velocity slightly shows a trend which indicates that the ice cliff density is lower with increased velocities. Overall, the strain rates have the same pattern as we have seen for Langtang, Bhutan and Everest site. The cliff relative area is highest where the strain rate is close to 0. With increasing compressive and extensive strain rates, the ice cliff density decreases. However the spread along the y-axis with value 0 is very high.

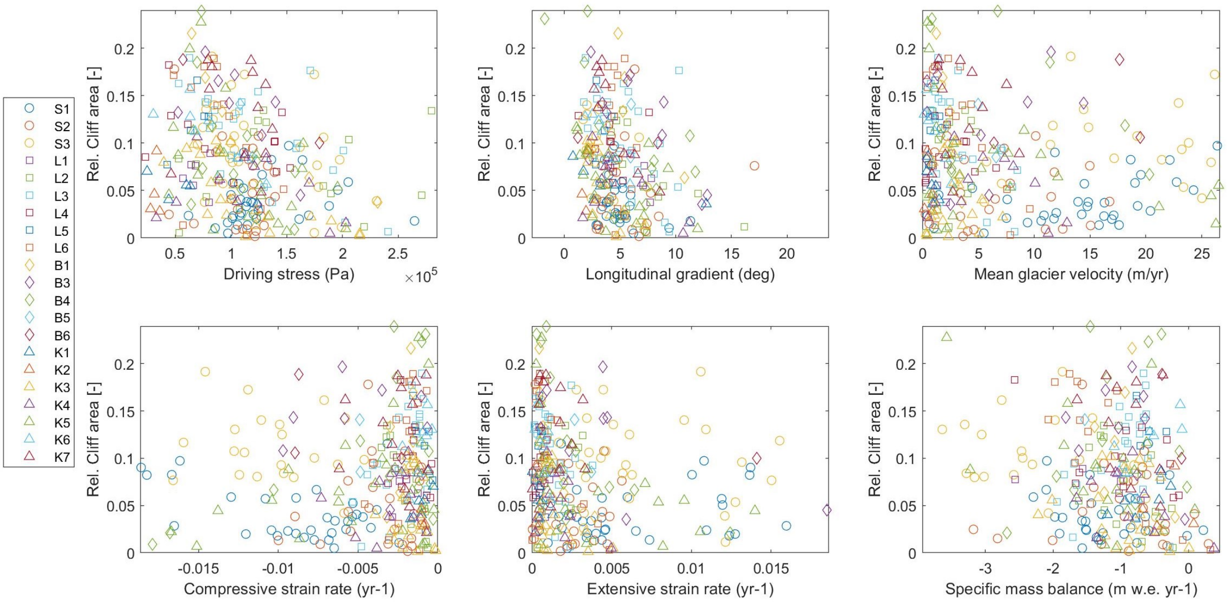

*Figure 21: Scatterplots of the ice cliff density plotted against the glacier characteristics averaged per elevation band for the whole study area.*

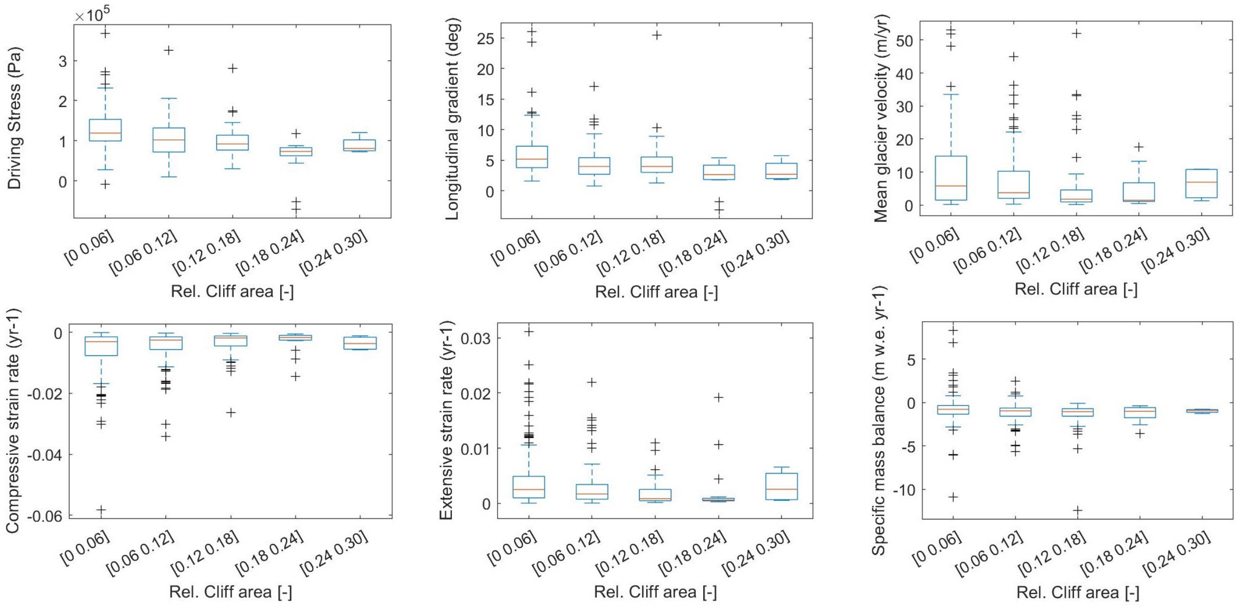

*Figure 22: Boxplots of the ice cliff density plotted against the glacier characteristics averaged per elevation band for the whole study area.*

# Discussion

This chapter is structured according to the three research topics defined in the introduction. It discusses the transferability of the ice cliff mapping with LSU-s to PlanetScope images and the adaptations that had to be done to this approach to have promising results. Additionally, the resulted ice cliff distributions of the four sites are compared to distributions of former studies and critically examined. Lastly, the relationships between the ice cliff density and potential ice cliff driving factors are discussed considering previous research.

## 7.1 Transferability of LSU-s to PlanetScope Images

The goal of Kneib et al. (2021b) was to find a delineation method which maps ice cliffs at different scales and with different spatial resolution imagery. This thesis extended the ideas of that study by testing the transferability of the LSU-s to PlanetScope images with a higher spatial resolution but lower radiometric precision than the Sentinel-2 satellite images with which the method was previously evaluated. The initial tests showed that the ice cliff mapping with LSU-s using PlanetScope images faces different challenges.

### 7.1.1 PlanetScope Imagery

PlanetScope images are taken from approximately 130 individual Dove CubeSat satellites. The satellite images are geometrically corrected and orthorectified using ground control points (GCPs), DEMs and a collection of reference images. The location accuracy of the products therefore varies by region based on available GCPs and DEMs (Planet Labs Inc., 2021). However, the effect of this discrepancy is minor for our research, because the ice cliffs are just mapped for one point in time. The results of this thesis are much stronger effected by the radiometric accuracy of the satellite images. Even if the radiometric accuracy of the PlanetScope data is based on numerous calibration methods, we found spectral differences between exactly overlapping PlanetScope scenes which are from the same date but collected from different satellites

(Figure 23 (A)). These differences can be explained by the facts that the sensors are not identical and the images can have different viewing angles, leading to varying spectral characteristics. In addition, there could also be errors in the geometric and radiometric correction of the two satellite scenes. This dissimilarity hinders the transferability of spectral end-members and threshold values from one scene to another. This issue is especially problematic for the purpose of this study, because the PlanetScope satellite scenes do not have a very large footprint, so mapping cliffs at the large scale requires to use multiple scenes of varying radiometric characteristics. In this study we used several scenes for each site and sometimes even for a single glacier. Figure 23 shows that the differences in the value distribution can be eliminated with the EQM bias correction.

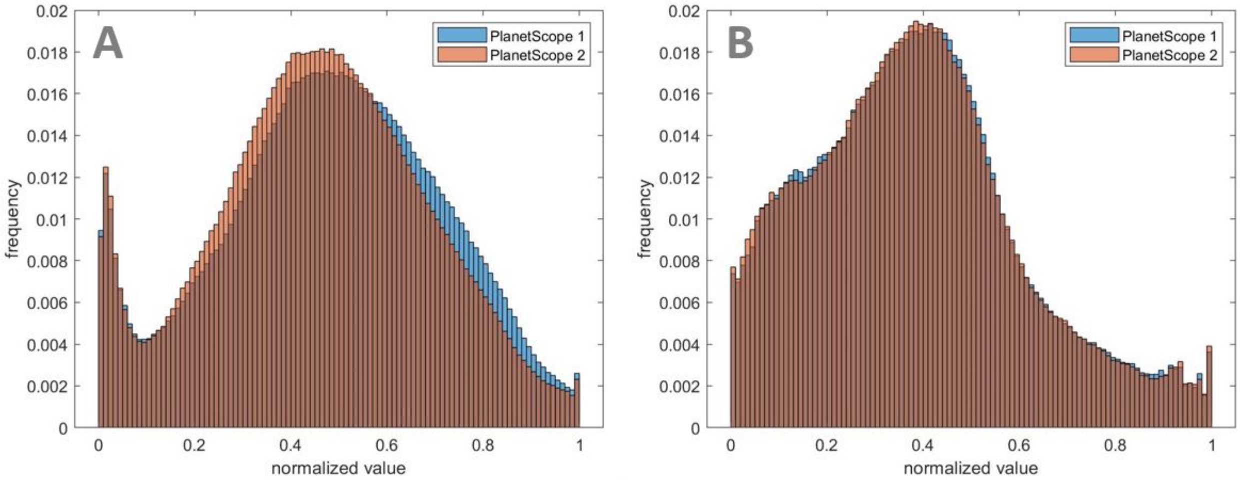

*Figure 23: Histograms of two exactly overlapping PlanetScope scenes from 2019-09-10 collected from different satellites (sensor IDs: 0F28, 0F22) before bias correction (A) and after bias correction to Landsat-8 (B).*

Another disadvantage of PlanetScope data are erroneous images where one spectral band is spatially offset to the other bands. The appearance of such an error can be explained by the band-separated geometric correction of the PlanetScope images. We found that for the PlanetScope images covering Khumbu Glacier where band 1 is shifted and the image reminds of a stereo image (Figure 24). The appearance of this error was therefore location dependent. This shift makes the mapping of ice cliffs with LSU-s impossible without an additional time-consuming geometric correction. When PlanetScope images are therefore used to map ice cliffs for the whole region of HMA, erroneous satellite images can lead to gaps in the cliff distribution.

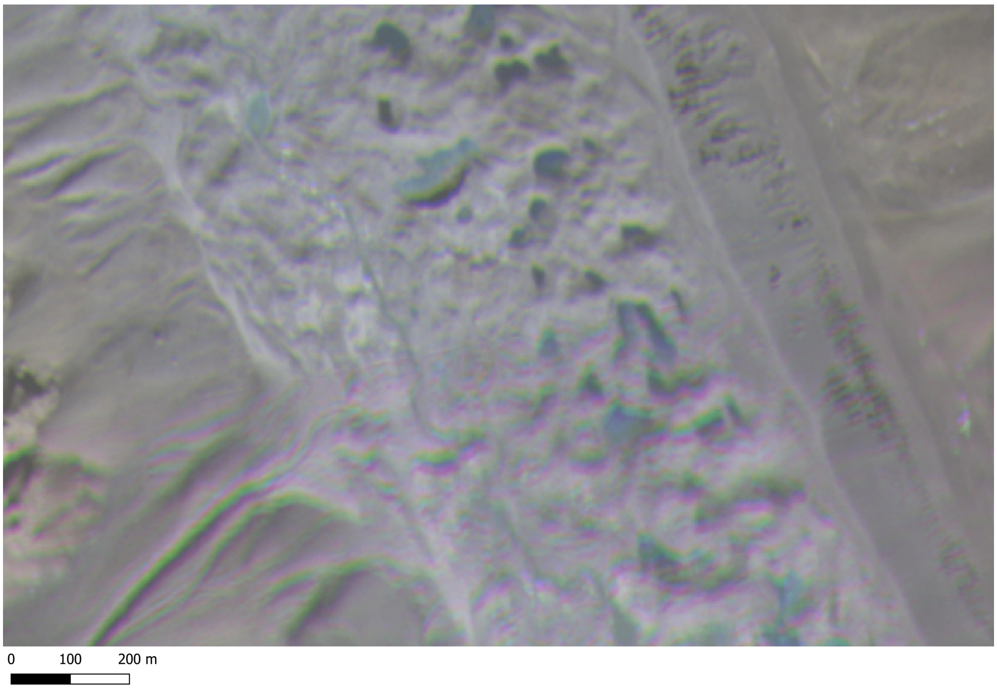

*Figure 24: Erroneous true-colored PlanetScope image of Khumbu Glacier showing the shift of band 1.*

Despite these issues, we found a way to overcome the radiometric differences in the PlanetScope images by bias correcting the satellite scenes to Landsat-8 images to make them spectrally as equivalent as possible. Including the bias correction with EQM in the mapping approach, we argue that PlanetScope data is applicable to semi-automatically map the ice cliff distribution at a larger scale with numerous satellite scenes.

Another point to discuss is that the different viewing angles of the PlanetScope scenes can lead to a disappearance of small, steep or overhanging cliffs in the images (Kneib et al., 2021b). This issue can bias to some extent the final ice cliff distributions. However, Steiner et al. (2019) stated that ice cliffs below a pixel area of 3-5 $m^2$ are so ephemeral that they are not of interest to a potential mass loss increase. Additionally, most of the ice cliffs that Steiner et al. detected were larger than 25 $m^2$. Considering these statements, the potential absence of small and steep ice cliffs in the PlanetScope images have a very small impact on the ice cliff distribution overall.

For the purpose of mapping ice cliffs at a regional scale, it is important that the satellite images are freely available. PlanetScope fulfils this requirement with a collection of daily data covering the entire Earth surface. Nevertheless, the monthly quota of 5000 $km^2$ which is approximately double the size of our summed up study area is limiting the download of data for larger regions. This limitation can be eliminated by requiring a special PlanetScope use agreement. Regarding this issue, Sentinel-2 or Landsat-8 data would be more applicable for larger scale mapping. They are as well less prone to spectral differences of the images due to individual image corrections, because Sentinel-2 data is collected by just two satellites whereas Landsat-8 data is collected by one satellite (The European Space Agency, 2021; USGS, 2021). However, the prominent advantage of PlanetScope data is the high resolution of 3 $m$ with which the resolution of Sentinel-2 (10 $m$) and Landsat-8 (30 $m$) cannot match. A high resolution is required to reduce the bias of missed-out ice cliffs. This is especially important since the ice cliff distribution is assumed to follow a log-normal distribution considering cliff size which means that there are more smaller ice cliffs than larger ice cliffs (Watson et al., 2017). Therefore, we argue that the adaptation of PlanetScope images is more desirable than the usage of Sentinel-2 or Landsat-8 images. Furthermore, the successful automatic ice cliff mapping with Pléiades from Kneib et al. (2021b) showed that the spectral resolution of four bands is enough to properly map ice cliffs and that more diverse spectral information as in Sentinel-2 images is not needed.

Multispectral images have the disadvantage that cloud cover and shadows are not excluded from the images and can cover relevant parts of the study area. The former can hinder the investigation of surface objects in areas with much precipitation and cloudiness. This would for example be the case if one wants to investigate supraglacial surface features in the monsoon season. Using multispectral images for ice cliff mapping in the monsoon-affected Himalaya is therefore not useful for all seasons. Because of the high temporal resolution of PlanetScope images, the issue of cloud cover in non-monsoon seasons is not major. However, shadows are a bigger problem, because they are dependent of the acquisition time instead of the season. LSU-s classifies shadows as dark ice cliffs and therefore they have to be excluded from the study area. To minimize this problem, the satellite images used for this approach should be collected around noon when shadows are shortest. Another issue that derives from the functioning of the LSU-s is snow cover, which is classified as bright ice cliffs. Therefore, snow cover also has to be excluded from the study area. The cutting out of snow and shadows can lead to an exclusion of relevant parts of the study area and bias the ice cliff distributions (ex. for glaciers S1/S2 in Figure 3). Despite the different issues mentioned in this paragraph, we argue that multispectral images can still be used for the semi-automatic ice cliff mapping in the Himalaya with LSU-s in pre- and post-monsoon season, when the debris-covered glaciers tongues are not covered with snow. The mapping also works in the monsoon season, when suitable cloud-free images are available.

### 7.1.2 Adaptation of LSU-s

#### Bias Correction

The bias correction of the PlanetScope images is done with Landsat-8 images which cover a whole study site and are as well taken in post-monsoon season 2019. Considering the snow-covered accumulation zone of the studied glaciers, it was impossible to find a Landsat-8 image which had no snow cover in a 1000 *m*-buffer around the debris-covered glacier tongue. Additionally, it was very difficult to find a Landsat-8 image that had no cloud cover or shadows in an area of 1000 *m* around the glacier outlines. As for the PlanetScope data, these disruptive factors would influence the bias correction and have to be cut out of the satellite image. This resulted in blended scenes which reduce the quality of the bias correction because less pixels of different surface types are compared. In the worst case, parts of the debris-covered glacier tongue had to be excluded from the study area which has an influence on the ice cliff distribution because no ice cliffs are mapped in affected areas. We can therefore conclude that Landsat-8 images are useful for the bias correction, because they include equivalent spectral bands as the PlanetScope images (Table 2) and the scenes cover a whole study area. Another advantage is that the images are collected from the same satellite and are therefore less prone to spectral differences. Nevertheless, Sentinel-2 data could be more suitable because the temporal resolution is three days instead of 16 for Landsat-8. The swath width of Sentinel-2 is 290 km and therefore even larger than for Landsat-8.

#### Calibration

The calibration of the method with the manual outlines from Pléiades images brings some uncertainties. Even though the PlanetScope images are coregistered to the Pléiades images of the same site, the viewing angles of the satellites can still differ due to biases in the correction to surface reflectance. This leads to not exactly overlapping satellite scenes and influences the Dice value. This issue has supported our decision to concentrate on Dice values higher than 0.5.

Additionally, because the Pléiades images have a higher spatial resolution of 2 *m*, it can show steep cliffs which do not appear in the PlanetScope scenes. This leads to more false negative values and decreases the Dice value.

The ranking method of the Dice values (Table 4) to find the end-member and threshold set to use for every scene has a high influence on the quality of the resulting ice cliff maps. For Satopanth and Langtang sites the final end-members and thresholds bring the second best or best Dice. However, Bhutan has the second lowest Dice with these parameters and would have better results with the end-members of the Langtang test scene. Nevertheless, the Dice of 0.5440 is higher than 0.5 and the difference to the highest Dice of 0.5880 is not too high. Also from a qualitative standpoint, the final outlines for Bhutan look consistent with what we would expect (Figure 25).

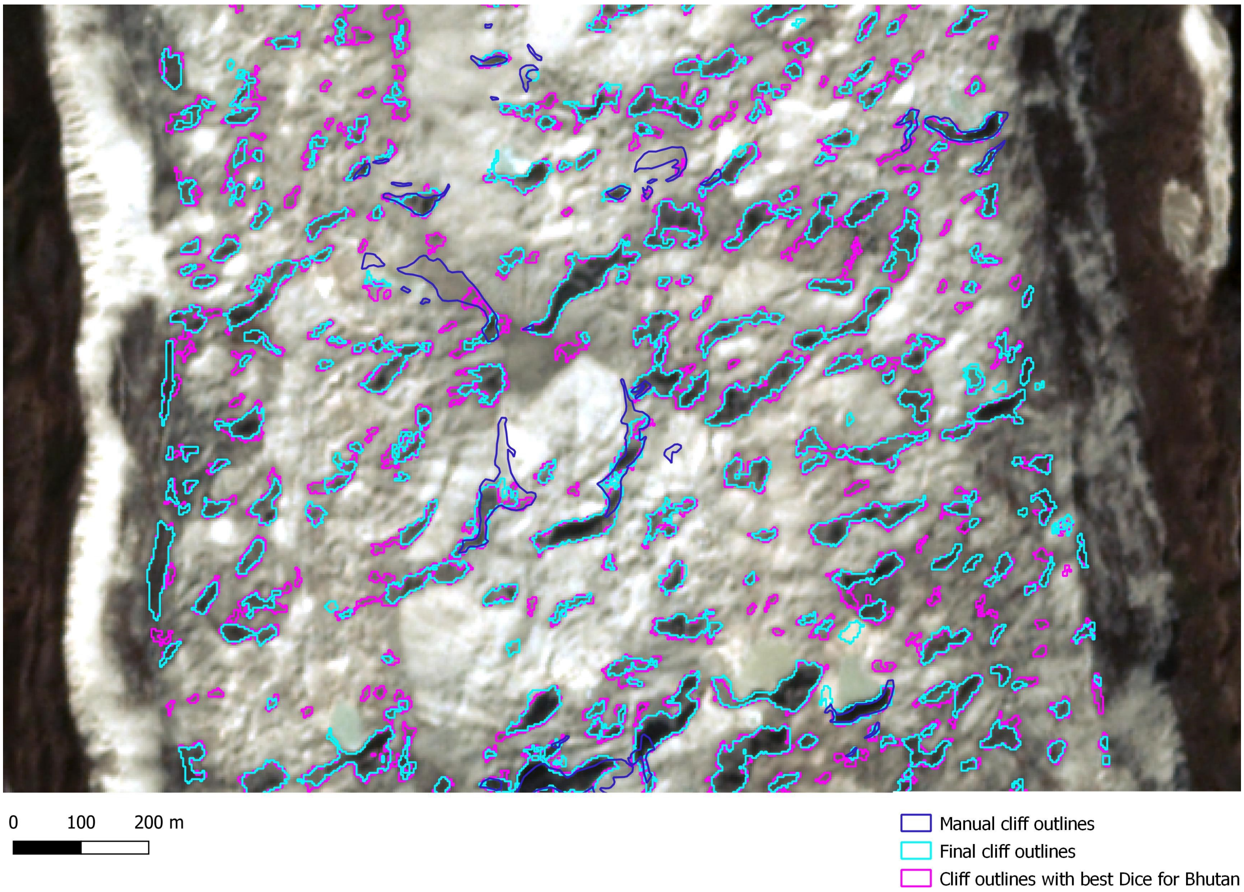

*Figure 25: Cliff map for Bhutan test scene with the final cliff outlines of this study compared to the cliff outlines with the best Dice value. Background: bias corrected true-colored PlanetScope image.*

Overall, the question remains whether one can transfer the end-member set from scene to scene or needs to take new end-members from every site. The shapes of the curves in the end-member spectra of the three test scenes (Figure 7) indicate significant variances. This dissimilarity can be explained by different spectral responses of the end-members "water", "dark debris" and "bright debris" from scene to scene which could be related to true differences in surface structure and appearance or to a bias in the correction of the satellite images. We can therefore conclude, that the spectral end-members are not consistent across the sites. However, examining the table of the Dice values, we can say that local end-members do not work best for the test scenes. We would therefore stick to the same end-member set for all the scenes, also considering the time saved for the processing for little to no improvement of the cliff maps. Examining the threshold sets, we can see that the Dice is always highest using the local scale thresholds. This means, that the ln(scale) maps differ from scene to scene and the scale thresholds are not excellently transferable. To further improve the estimation of ice cliff distribution, new scale threshold values for every scene could therefore be derived. But for that, a sample set of manual cliff outlines is needed and the method would be much less automated. However, considering the promising results of this study and the goal to have a mapping method which is as automated as possible, we argue that LSU-s is applicable to map ice cliffs at larger scales by using the same thresholds across satellite scenes.

### Post Processing

The post processing of the cliff maps with object classification is associated with many uncertainties. The definition of a threshold for this classification as it was done in this study is very subjective because it depends on visual checks of the ice cliff outlines overlaying the ln(scale) map and the generated histograms and scatterplots. With the goal of a time saving threshold definition to generate the best possible ice cliff distributions, it has just been decided for every scene to either use a threshold of 0.25 or 0.3. The post processing can be improved by finding a statistic-based method considering the distributions of the mean ln(scale) values per objects to automate the threshold definition for every scene.

### Method Evaluation

To check if the method used in this thesis is appropriate for mapping ice cliffs on debris-covered glacier tongues, we can compare the manual cliff outlines from Pléiades with the ln(scale) map to see if the ice cliffs are clearly visible. Figure 26(A) shows a section of Langtang Glacier (L4), where the manually mapped ice cliffs are clearly identifiable in the ln(scale) map. Most of the ice cliff pixels have a ln(scale) value lower than -0.35 and are therefore classified as ice cliffs taking a threshold of -0.30 to post process the ice cliff distribution. Contrarily, the manually delineated ice cliffs in Figure 26(B) are not clearly visible as a whole ice cliff in the ln(scale) map. Most parts of these ice cliffs would not be classified as cliff after the post processing. This issue could just be improved by a more appropriate end-member set for the Langtang test scene. Nevertheless, it is questionable if the semi-automated ice cliff mapping could be improved with a new set of end-members or if this is a limitation of the LSU-s approach.

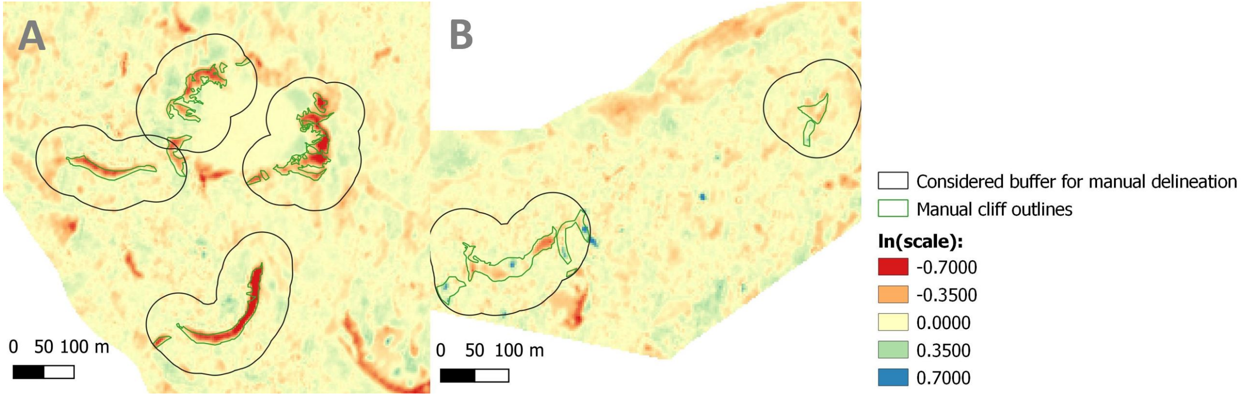

*Figure 26: Manually delineated cliff outlines from Pléiades for two sections of Langtang Glacier (A & B) compared to the ln(scale) map of this test scene.*

The scatterplots of the object means of ln(scale) in Figure 13 show that larger ice cliffs have higher absolute mean ln(scale) values. We can therefore conclude that the semi-automatic cliff delineation with LSU-s works best for large ice cliffs which are clearly visible in the PlanetScope images. However, choosing a high upper scale threshold which just maps the large and clearly visible cliffs would underestimate the ice cliff distribution. It is therefore more appropriate to chose a lower threshold leading to a positive bias and post process the ice cliff maps to remove small false positive ice cliffs from the cliff maps.

To further evaluate the method, the cliff distribution of the Langtang test scene is compared to the cliff outlines of Kneib et al. (2021b) which are based on a Sentinel-2 and a Pléiades image. It can be seen in Figure 27 that the cliff distribution improved with the semi-automated method used in this study compared to the Sentinel-2 outlines. The outlines generated in this study overlap the Pléiades outlines very well apart from minor small ice cliffs and bright ice cliffs, which can be seen at the bottom left of Figure 27. The results of this new LSU-s method are therefore promising but there is still room for improvements. Bright cliffs are for example not mapped properly because they cannot clearly be seen in the ln(scale) map. This does not have a high influence on the results of this study, because the studied glaciers have a negligible number of bright cliffs. The cliff densities are therefore not majorly biased. However, using the adapted LSU-s approach for a glacier with a higher number of bright ice cliffs on it could be problematic because the resulting ice cliff distribution would be negatively biased.

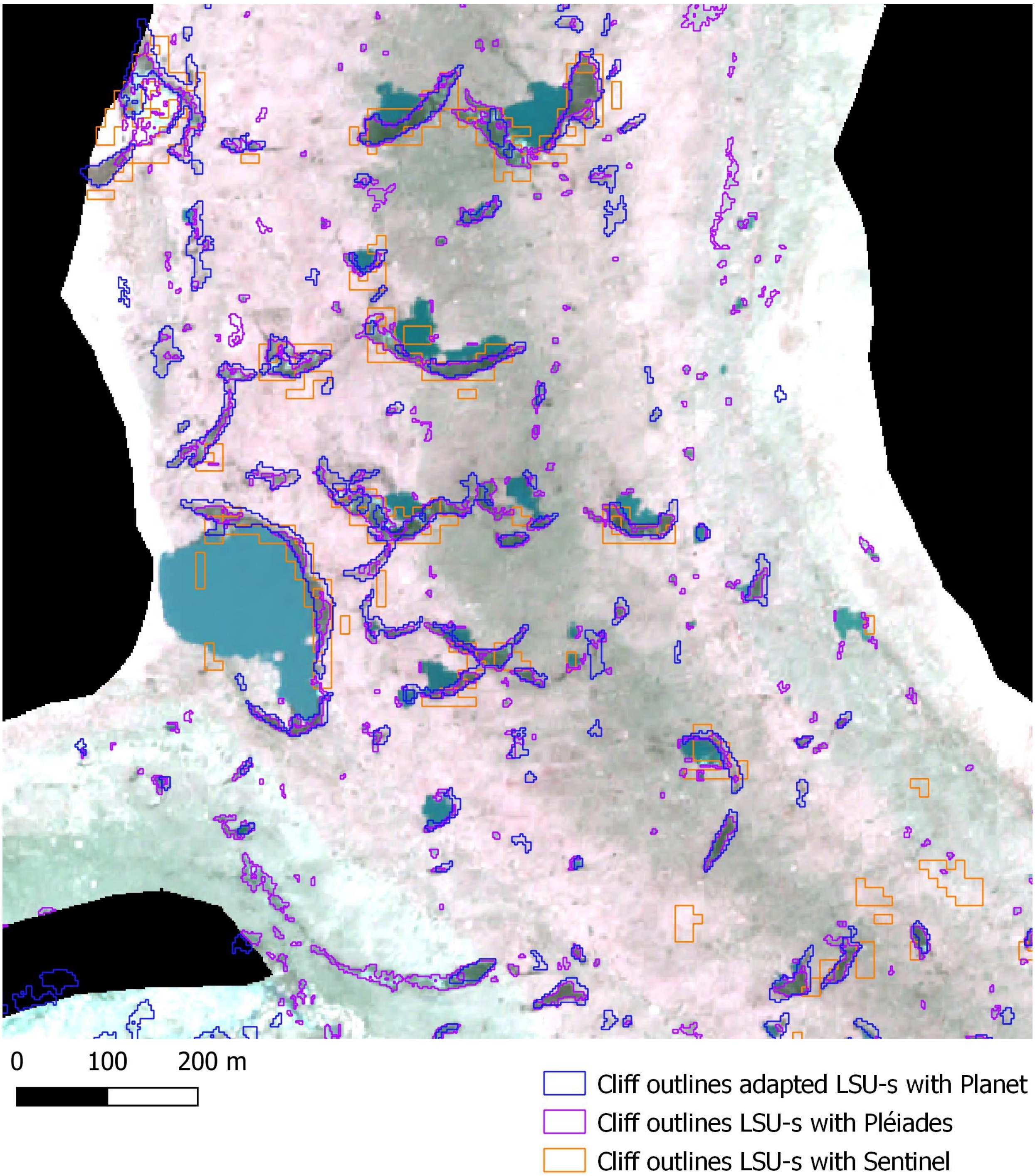

*Figure 27: Automatically generated cliff outlines from PlanetScope with the adapted LSU-s and from Pléiades and Sentinel-2 with LSU-s from Kneib et al. (2021). Background: false-color composite (NIR, red, green) Pléiades image acquired on 2019-06-14.*

To evaluate the transferability to sites where no validation set is available, the ice cliff distribution of the debris-covered glaciers of the Everest site (Appendix 10.3) are visually checked. The maps of the automatically classified ice cliffs look reasonable. Therefore, we assume that the adapted LSU-s approach is applicable to other study sites that do not show major variations in surface characteristics compared to validated sites.

Concluding, it can be said that the semi-automated ice cliff mapping with the LSU-s approach needed a lot of adaption and additional working steps, but at the end the resulting ice cliff distributions met our expectations. Overall, the mapping method used in this study works best for debris-covered glacier tongues that have rather large and darker ice cliffs than the surrounding debris. Additionally, the ice cliff mapping with LSU-s just works for areas and seasons with minimized cloud and snow cover. These points limit the usage of the method and it is therefore questionable if the ice cliff mapping with the LSU-s works at larger scales including more heterogeneous sites.

### 7.1.3 Definition of Spectral End-Members

The definition of the spectral end-members is subjective, because they are manually chosen from the satellite images and are therefore based on the expert knowledge of the operator. The selection is tricky and associated with many uncertainties because the defined pixels should only be composed of one of the pure spectral end-members (Kneib et al., 2021b). To minimize the uncertainty, it is useful to have a large number of sample points covering the whole spectral range for each end-member. Additionally, the dataset should be independently checked by at least a second operator to reduce the subjective selection bias.

## 7.2 Ice Cliff Distribution

This section compares the ice cliff densities of selected glaciers computed in this study with the relative ice cliff area found in former studies. Additionally, the variability of ice cliff distribution across the study sites and at glacier scale is discussed and explained.

### 7.2.1 Comparison with Former Studies

To validate the ice cliff densities that were computed in this study, we compare the relative ice cliff area of selected glaciers to former studies (Table 6). Overall, the ice cliff densities derived from the semi-automated ice cliff mapping with the adapted LSU-s approach are with the exception of S1/S2 considerably higher than the numbers found in former studies.

*Table 6: Ice cliff densities of selected glaciers from this study compared to ice cliff densities found in former studies.*

| | **Ice Cliff Density [%]** | | | | |
|---|---|---|---|---|---|
| | *This Study* | *Kneib et al., 2021* | *Steiner et al., 2019* | *Thompson et al., 2016* | *Kraaijenbrink et al., 2016* |
| *Mapping Method* | LSU-s | SC | manual delineation | manual delineation of top of ice cliffs | OBIA |
| *Image Type* | multispectral | multispectral | multispectral & DEM | DEM | DEM |
| *Spatial Resolution* | 3 *m* | 2 *m* | 1.5 - 9 *m* | 1 *m* | 0.1 - 0.2 *m* |
| **S1/S2** | 3.90 | 9.20 | | | |
| **L1** | 6.16 | | 2.00 | | |
| **L2** | 7.81 | | 2.70 | | |
| **L3** | 10.84 | 3.30 | 2.40 | | 1.80 |
| **L6** | 10.79 | | 3.00 | | |
| **K5** | 8.96 | | | 5.00 | |

On the one hand, these differences in the relative cliff area can be explained by differences in the ice cliff mapping methods. Each of these methods are based on a different definition of an ice cliff which influences the mapped ice cliff distributions. LSU-s (Kneib et al., 2021b) assumes that everything that looks like ice on debris-covered glacier is an ice cliff. OBIA (Kraaijenbrink et al., 2016) is more empirical and does additionally include the shape and values of the different bands in its definition of an ice cliff. Furthermore, slope based methods (Herreid and Pellicciotti, 2018; Reid and Brock, 2014) assume that ice cliffs have to be steep and that flat bare ice in contrary to the LSU-s is not a cliff. A manual delineation of ice cliffs depends on the ice cliff definition of the human operators and is therefore subjective compared to the more objective and physically based semi-automated mapping methods. Manual cliff delineation methods where only the top of the ice cliffs are delineated as lines (Thompson et al., 2016) and an area-perimeter relationship is assumed to compute the ice cliff area have high uncertainty in the ice cliff distribution and the reported cliff density.

The higher cliff relative areas of this thesis compared to numbers of former studies can be explained by an overestimation of ice cliffs in our results which comes from the definition of rather low thresholds. We decided on this positive bias because we wanted to be sure, that no obvious ice cliffs were left out and because it is simpler to exclude ice cliffs from the automatically derived map with post processing than to add ice cliffs to the distribution. Contrary to this statement, the ice cliff density of glaciers S1/S2 is almost 2.5 times higher in Kneib et al. (2021b) than what we derived in this thesis. Comparing the two ice cliff maps, we conclude that Kneib et al. automatically mapped many very small ice cliffs which are not mapped with the adapted LSU-s. This could be attributed to a positive bias in the SC approach of Kneib et al. or to small ice cliffs which are not visible in the PlanetScope image because it has a lower resolution than the Pléiades and geometric corrections could have lead to an exclusion of these cliffs from the PlanetScope image. Latter can be rejected if one takes into account that the lower relative cliff areas of the other studies are based on data with higher resolution.

On the other hand, differences in the ice cliff density can also be explained by factors which are not related to the method but to surface changes of debris-covered glaciers. They can for example be linked to seasonal changes which show higher ice cliff relative areas due to larger cliffs in the wet pre-monsoon season than in the dry post-monsoon season (Steiner et al., 2019). With this assumption, the ice cliff area will further grow with an extent of the melting period in the future (Bolch et al., 2012; Azam et al., 2018; Bhattacharya et al., 2021). However our results do not confirm this finding but rather show the opposite. The considerably lower ice cliff density of Langtang Glacier (L3) derived by Kneib et al. (2021b) is based on a Pléiades image taken in June 2019 whereas the PlanetScope image used in this study was collected in September 2019. The relative ice cliff area is therefore much higher in the dry post-monsoon season.

Additionally, the increase of ice cliff density can be linked to an ongoing surface lowering of the investigated glaciers due to recent melt increase, which leads to a higher number of supraglacial ponds and large ice cliffs surrounding these ponds (Ragettli et al., 2016; Watson et al., 2017; Steiner et al., 2019). This phenomena could explain the higher ice cliff density of Langtang Glacier (L3) in 2019 that is reported in this thesis compared to the relative cliff area derived by Steiner et al. (2019) for 2015 and by Kraaijenbrink et al. (2016) for 2014. Kraaijenbrink et al. found a rather low relative ice cliff area of 1.8% for a section of approximately one seventh of the debris-covered area of L3 which covers the terminus of the glacier. This number is more than 10 times lower than the ice cliff density we derived in this thesis. Figure 28 shows that the surface changed a lot in the five years between the images. It therefore confirms the assumption of a change in surface characteristics as a reason for increased ice cliff density. This statement is supported by Kneib et al. (2021a) finding that the relative ice cliff area can change by up to 20% in only one year. Considering these points, the ice cliff density may further increase in the future due to higher melt rates leading to further surface lowering of debris-covered glaciers. A larger ice cliff area in turn leads to higher melt rates. This process is therefore a positive feedback.

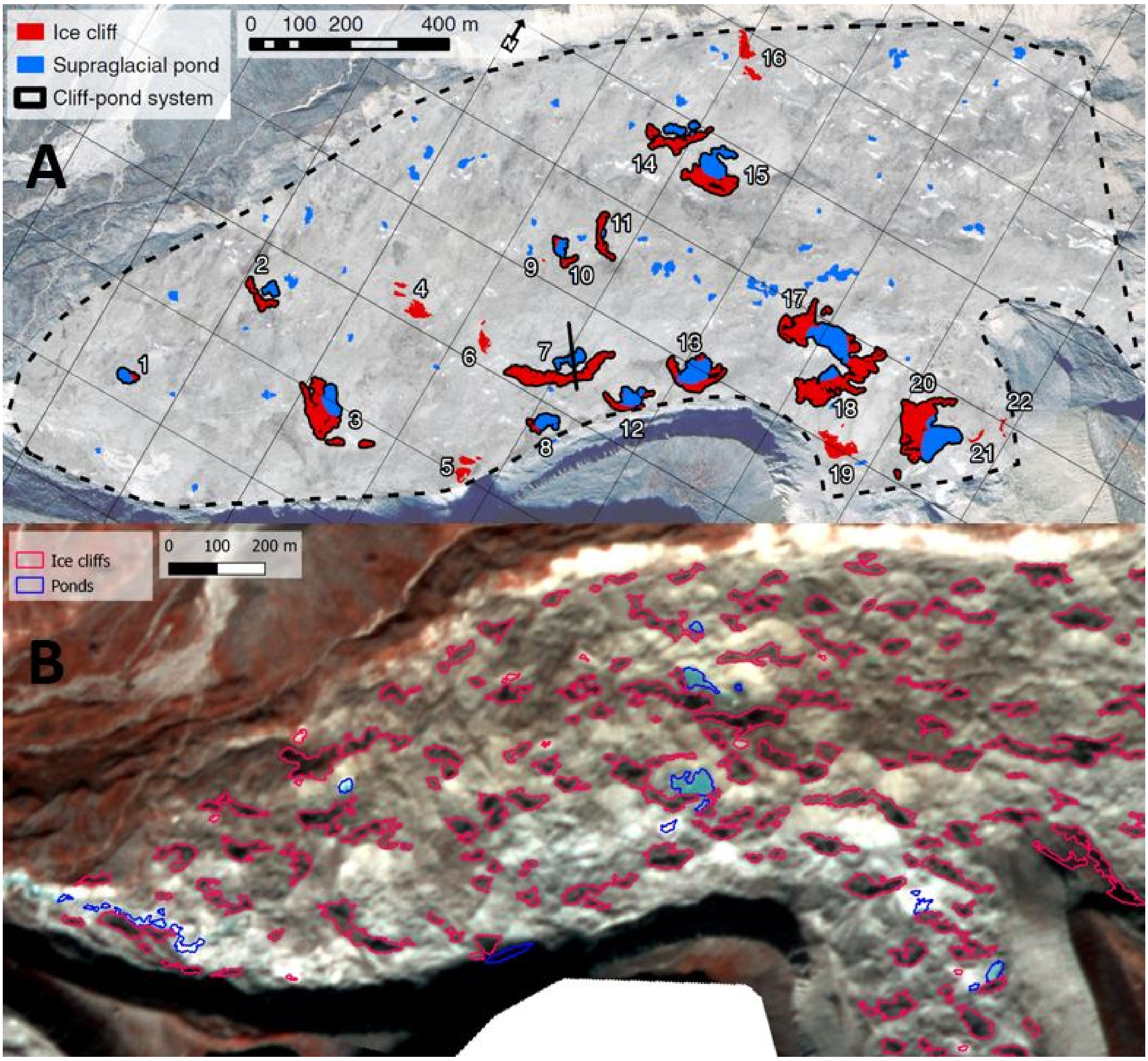

*Figure 28: Ice cliff map from May 2014 generated with OBIA from Kraaijenbrink et al. (2016), background: UAV image (A). Ice cliff map from November 2019 generated with adapted LSU-s from this study, background: bias corrected false-color composite (NIR, red, green) PlanetScope image (B).*

### 7.2.2 Variability of Ice Cliff Distributions

The ice cliff distribution is variable and not consistent across the debris-covered glaciers in the study area. The glaciers at the Bhutan site tend to have more ice cliffs than the other sites. Nevertheless, this statement must be viewed critically, because the higher ice cliff density can also come from a bias in the semi-automated ice cliff mapping, which failed to get rid of small false-positive ice cliffs. The variability of ice cliff distribution is also prominent on most of the glaciers showing differently shaped and sized ice cliffs on the debris-covered glacier tongue. Apart from that, glaciers which show a random pattern of ice cliff density across elevation bands have similarly shaped and sized ice cliffs on the whole debris-covered area. This finding is approved by Thompson et al. (2016) who found a uniform ice cliff distribution for glacier K5, where the ice cliff distribution of this study does not show a clear pattern.

Higher ice cliff density per elevation band is either due to larger cliffs or an increased number of cliffs. Larger ice cliffs can be associated with a higher number of supraglacial ponds which lead to increased melting of ice cliffs at the site of the ponds (Steiner et al., 2019). This phenomena occurs on glaciers with higher cliff density along the flow line, because a lower surface gradient towards the terminus of the glacier leads to an increased number of ponds (Benn et al., 2012). Additionally, Kraaijenbrink et al. (2016) found a higher number of larger cliff-pond systems at a confluence of Langtang Glacier (L3) due to higher strain rates. However, this finding cannot be confirmed with our results. In contrast to the statement of this paragraph, Steiner et al. (2019) stated that Lirung Glacier (L1) shows an atypical distribution of cliff size, where ice cliffs not connected to ponds are larger than the ones connected to ponds. This is also visible on our ice cliff map. However, this finding must be critically assessed because there are just three ponds mapped for L1. Our study therefore shows the opposite of a former study which concluded that ice cliffs on L1 are generally found near lakes (Immerzeel et al., 2014).

Furthermore, large ice cliffs with a straight and not circular shape perpendicular to the flow line can be linked to the opening of crevasses in areas with prominent elevation changes (Reid and Brock, 2014). The ice cliff maps of this study show this phenomena for glaciers with high cliff density in the center of the glacier.

At last, larger ice cliffs with a meander-like shape along the flow line appear on glaciers where melt water flows through cryo-valleys which have ice cliffs at the site (Mölg et al., 2020). Summing up, the investigated glaciers display all three ice cliff types, which Steiner et al. (2019) defined in their study: lateral cliffs which are perpendicular to the flow line, longitudinal cliffs which are positioned along the flow line and circular cliffs which have a partially or completely circular shape and mostly coexist with supraglacial ponds (Figure 29).

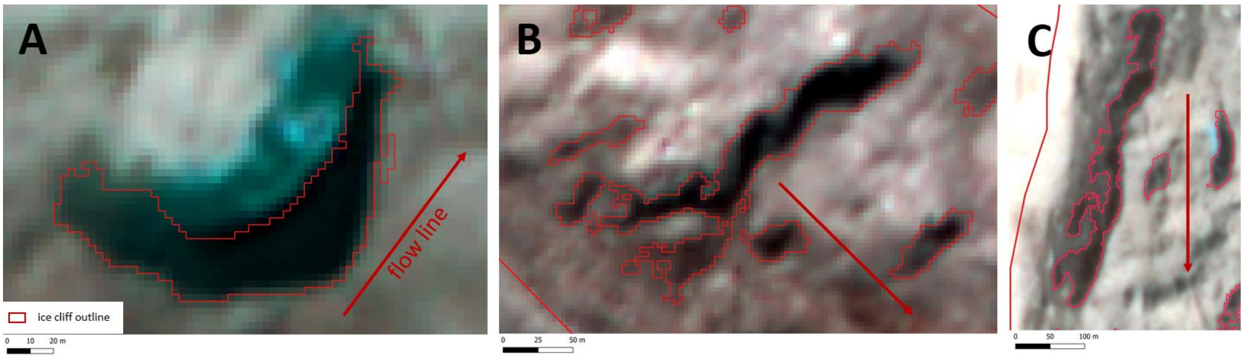

*Figure 29: Circular ice cliff at the side of a pond on glacier S1 (A). Lateral ice cliff perpendicular to the flow line on glacier L1 (B). Longitudinal ice cliff along the flow line on glacier B1 (C). Background: false-color composite (NIR, red, green) PlanetScope images.*

Generally, north-facing ice cliffs of each ice cliff type are more stable and therefore more numerous than south-facing cliffs which are exposed to direct sun radiation leading to higher melt at the top of the ice cliffs. These increased melt rates lead to a flattening of the ice cliff and if the critical steepness of approximately 30° is reached to its disappearance due to debris accumulation (Buri and Pellicciotti, 2018; Steiner et al., 2019; Herreid and Pellicciotti, 2018). The dominance of north-facing ice cliffs on Langtang Glacier (L3), which Kraaijenbrink et al. (2016) described in their study, can be approved with our results in a qualitative way by visually investigating the ice cliff map of L3 (Appendix 10.3). For a better qualitative verification of this assumption, the cliff aspect would have to be derived.

To conclude, interpreting the ice cliff density distribution by looking at the ice cliff density per elevation band shows interesting patterns on the investigated glaciers which can be linked to different phenomena. Nevertheless, the interpretation can be problematic when large cliffs along the flow-line are present. These cliffs can be separated by elevation bands and bias the interpretation of the cliff size and shape for different ice cliff densities. This phenomenon is for example prominent on glacier B1 (Appendix 10.3).

## 7.3 Driving Factors of Ice Cliff Distribution

### 7.3.1 Method Evaluation

Finding relationships between the glacier average values of relative cliff area and glacier characteristics at the scale of the whole study area is not representative because most of the glaciers show heterogeneous patterns of ice cliff distribution. An averaged value over the glacier does therefore not represent the variability and can lead to misinterpretation of relationships between the ice cliff density and potential driving factors. Averaging would just make sense for glaciers which have a homogeneous ice cliff distribution over the whole debris-covered area. Another criticism of averaging at glacier scale in this study is the small sample size. With 21 data points, it is very difficult to find relationships between the datasets and the uncertainty is higher. It is therefore useful to average the ice cliff density and the glacier characteristics at elevation bands to compare the datasets at the larger scale.

Furthermore, the analysis at the scale of a study site is not relevant for this study. This can be explained by the high spread of the data in the scatterplots of the four study sites (Figure 17-20) which comes from high variability in ice cliff distributions at the sites. The glaciers at each site do not show similar patterns of ice cliff density and furthermore, the ice cliff sizes and shapes are as well very variable within and across glaciers. Moreover, the relationships we found across sites are similar and it is therefore useful to directly plot the ice cliff density and the glacier characteristics averaged per elevation bands for all the glaciers in the study area. Nevertheless, the concentration on differences from site to site can be interesting if the sites are further away from each other and lay in a completely different climate regime.

To further understand the formation mechanisms and dynamics of ice cliffs at a local scale, it would be best to investigate the ice cliff distribution and the potential driving factors of every single glacier to find clear correlations. For that, we would not only look at the ice cliff density but also the ice cliff size, shape and aspect variations. This study contributed to this research by developing a transferable semi-automatic ice cliff mapping method which can generate a detailed ice cliff distribution at glacier scale for numerous glaciers.

### 7.3.2 Correlations with Driving Factors

The relationships we found between the ice cliff density and the glacier characteristics considering the elevation band averages confirm the findings of previous studies.

The negative correlation of the ice cliff relative area and the longitudinal gradient, which can be discovered considering both the elevation band and glacier averages, is also observed by Steiner et al. (2019). This correlation is linked to the negative correlation with driving stress and glacier velocity. The lowering of the ice surface leads to a reduction in glacier velocity and driving stress. In such areas, the collapse of englacial conduits and the formation of supraglacial ponds are more likely to happen. The ice cliffs which are built with this process are rather large and therefore, the ice cliff density increases because of more and larger cliffs (Benn et al., 2012; Steiner et al., 2019; Mölg et al., 2020). These processes will be enhanced in the future, because mass losses and retreat of glaciers result in more debris cover, a decrease of glacier velocity and the formation of further glacier lakes (Bolch et al., 2012).

The relation we found for the ice cliff relative area and the strain rates considering the elevation band averages is different to what was stated in former studies. Our results assume a negative relation where ice cliff density decreases with increasing strain rates. On the contrary, Reid and Brock (2014) described the opening of crevasses as an ice cliff formation mechanism in areas where extensive strain rates are high. This process of crack formation in the ice surface as well as the collapse of conduits and the cliff-forming process of debris slumping with increased strain rates is confirmed in other studies (Benn et al., 2012; Kraaijenbrink et al., 2016; Watson et al., 2017; Moore, 2018; Steiner et al., 2019). Considering these contrary findings, we come to the conclusion that the investigated debris-covered glaciers have less ice cliffs which are formed with the processes of crevasses opening and debris slumping. Though, our results could also suggest that strain rates are not appropriate to detect ice cliffs on a debris-covered glacier. The relationship between the cliff density and the strain rates considering the glacier averages is opposite than the one considering the elevation band averages and does therefore confirm the findings of the previous studies mentioned above. However, considering the small sample size of 21 glaciers, we believe that this finding is random and does not represent a real correlation of ice cliff density and strain rates for the glaciers in this study.

Additionally, our results do not confirm the formation of cryo-valleys (Mölg et al., 2020) and debris slumping at oversteepening slopes (Moore, 2018; Westoby et al., 2020) as ice cliff drivers, because these processes are said to happen mostly in areas where longitudinal gradient is high.

One relationship just occurred for Bhutan site. There, the specific mass balance seems to increase with higher ice cliff relative area. Considering the driver of ice cliff research to be the influence of the cliffs on glacier mass balance, this correlation was discovered in previous studies investigating the mass balance of debris-covered glaciers in HMA (Pellicciotti et al., 2015; Salerno et al., 2017). These studies identified an influence of supraglacial surface features such as ice cliffs on the specific mass balance of debris-covered glaciers.

Finally, it is important to say that no evidence or opposite findings do not mean that the correlations described in previous research do not exist, but that they cannot be shown with our data. These can be due to no appearance on the glaciers we investigated or due to the scales that we chose for interpreting the data. As the cliff formation processes happen at the local scale, we don't expect all of them to transpire at a larger scale. A detailed analysis of the relations of the ice cliff distribution and glacier characteristics at the local scale could lead to different outcomes.

Nevertheless, our findings contribute to the better understanding of ice cliff formation processes which is important to achieve regional glacier melt models which consider the influence of ice cliffs.

# Conclusion and Outlook

This chapter summarises the main findings of this thesis by answering the research questions. Furthermore, an outlook is given on the further improvement of the semi-automated ice cliff mapping method developed in this study and on future research in the field of ice cliffs based on the resulted ice cliff distribution.

## 8.1 Conclusion

This Master thesis had three aims which could be achieved with the method development, the application of the method and the analysis of the final ice cliff distribution. The first aim was to test the transferability of the semi-automated LSU-s approach developed by Kneib et al. (2021b) to PlanetScope multispectral images.

Secondly, we aimed to map the distribution of ice cliffs from PlanetScope satellite images at four different sites spread over HMA for the post-monsoon season 2019 using the further adapted semi-automated cliff delineation method.

The third aim was the comparison of the final ice cliff distribution with different glacier characteristics to identify the driving factors of ice cliff distribution.

Overall, the semi-automated ice cliff mapping approach developed in this study contributes to the ice cliff research by providing a method which allows a detailed mapping of ice cliffs for multiple satellite scenes over a large area. Considering the level of detail, the ice cliff distributions can not only be used for larger scale analysis, but also for the analysis of ice cliff formation and dynamics at local scale.

### Transferability of LSU-s to PlanetScope images

Despite the promising results, this study found a few limitations for the LSU-s approach. Principally, it has difficulties to map ice cliffs that are brighter than the surrounding debris. Secondly, larger ice cliffs can be recognized better in the ln(scale) maps. We therefore conclude, that the semi-automated ice cliff-mapping with LSU-s works best for debris-covered glaciers covered with rather large ice cliffs which are darker than the surrounding debris. As this was the case for most of the glaciers in our study area, we are overall satisfied with the final ice cliff maps.

1.1 Can PlanetScope satellite images be used to map ice cliffs on several glaciers across HMA in a semi-automated way?

PlanetScope images meet most of the requirements to map the ice cliff distribution at larger scales. The high spatial resolution of 3 $m$ allows to have detailed ice cliff distributions for each glacier considering that ice cliffs below a pixel area of 3-5 $m^2$ are very ephemeral and can therefore be neglected. Beside the adequate spatial resolution, the spectral resolution of PlanetScope images with the four bands blue, green, red and NIR is sufficient to properly map ice cliffs. Furthermore, PlanetScope images are freely available with an academic licence which is very important to map ice cliffs at a larger scale. Beside these advantages, there are some challenges which can limit the application of PlanetScope images at larger scales. Firstly, erroneous satellite scenes can lead to gaps in the ice cliff distribution. However, we just found one erroneous scene in 19 during this study. Secondly, multispectral images in general can just be used for the identification of surface features when they are cloud-free and not covered with shadows. Because the numerous PlanetScope satellites take images of the entire Earth surface on each day, this issue is not significant. Lastly, PlanetScope scenes show radiometric differences due to not identical sensors and errors in the geometric and radiometric corrections. Nevertheless, these differences can be overcome with the bias correction of the images to Landsat-8 scenes. Considering all these points, PlanetScope images are applicable to semi-automatically map the ice cliff distribution at a larger scale.

1.2 How do the PlanetScope images need to be adapted so that the delineation method is transferable over multiple satellite scenes?

That PlanetScope scenes can be used to map the ice cliff distribution at larger scales, they have to be bias corrected to remove radiometric differences between the satellite images. This is especially important, because the mapping of ice cliffs on numerous glaciers with PlanetScope images requires multiple satellite scenes of varying radiometric characteristics which hinder the transferability of end-members and thresholds from one scene to another. The bias correction was done with Landsat-8 images which include the same spectral bands as PlanetScope data. Furthermore, Landsat-8 scenes have a larger footprint and cover a whole study site. Lastly, these images are less prone to spectral differences because they are collected from one satellite. The bias correction was performed with empirical quantile mapping which adapts the histograms of the PlanetScope scenes to the histograms of the Landsat-8 scenes.

1.3 How consistent are the spectral end-members across the study sites?

Considering the spectra of the spectral end-members of the bias corrected PlanetScope test scenes (Figure 7), we can say that the end-members are not consistent across the study sites. This inconsistency either comes from different spectral responses of the end-members "water", "dark debris" and "bright debris" or the subjective manual selection of the end-members at each test site. Nevertheless, local end-members do not work best for each test scene. We can therefore conclude that an end-member set is transferable if a large number of sample points covering the whole spectral range for each end-member is selected and if the satellite scenes are not significantly heterogeneous.

### Distribution of ice cliffs across the study sites in HMA

2.1 Is the ice cliff distribution consistent over the whole study area?

The ice cliff distribution is variable and not consistent across the debris-covered glaciers at each site and across the study area. At the glacier scale, the investigated glaciers have different patterns of ice cliff distribution showing different sizes and shapes of ice cliffs. Only the glaciers showing a random pattern of ice cliff density per elevation band have similarly shaped and sized ice cliffs on the whole debris-covered glacier tongue. We conclude that a higher relative cliff area across a glacier is either due to larger ice cliffs or an increased number of ice cliffs. Additionally, our ice cliff maps show three specific ice cliff types: lateral ice cliffs which are perpendicular to the flow line, longitudinal ice cliffs positioned along the flow line and circular ice cliffs mostly coexisting with supraglacial ponds.

2.2 What is the ice cliff density for each glacier and how does it differ across HMA?

The relative ice cliff area of the investigated glaciers has a very high range going from 3.9% (Satopanth and Bagirath Kharak Glacier) to 17.1% (Lunana Glacier). The ice cliff densities vary significantly within and across study sites. We assume that we cannot see clear differences in the ice cliff density from site to site because the study sites are rather close to each other and therefore lay in similar climate regimes. Compared to former studies, the relative ice cliff areas derived from the semi-automated mapping with the adapted LSU-s are considerably higher. This can be explained by differences in the mapping methods, by a positive bias in our final ice cliff distribution and by changes in the surface characteristics of the debris-covered glaciers.

**Potential ice cliff driving factors**

3.1 How does the ice cliff density calculated per glacier correlate with different glacier characteristics at the scale of the whole study area?

We determined that the comparison of the ice cliff density and the glacier characteristics calculated per glacier is not representative because most if the investigated glaciers show heterogeneous patterns of ice cliff distribution. Furthermore, the sample size of 21 glaciers is too small to show significant correlations. Nevertheless, we can assume a correlation between the cliff relative area and the longitudinal gradient. The ice cliff density seems to decrease with increasing longitudinal gradient. This finding is confirmed by the comparison of elevation band averages.

3.2 How does the ice cliff density calculated across elevation bands for each glacier correlate with glacier characteristics at the scale of a study site?

Most of the correlations which we found at the scale of a study site are similar across sites. They are therefore recognizable in the comparison of the ice cliff density and the glacier characteristics averaged per elevation bands at the larger scale which is described in the next paragraph. An expectation is the correlation between the relative cliff area and the specific mass balance occurring at Bhutan site. The specific mass balance increases with higher ice cliff density. This finding is reasonable because former studies identified higher melt rates for ice cliffs. We conclude that high variability in the ice cliff distribution at each site makes the comparison between sites unclear and the analysis at the scale of a study site irrelevant for this study.

3.3 How does the ice cliff density calculated across elevation bands for each glacier correlate with glacier characteristics at the scale of the whole study area?

Considering the elevation band averages at the scale of the whole study area, we found a negative correlation between the ice cliff density and the longitudinal gradient which is linked to the negative correlations with driving stress and glacier velocity. These correlations can be explained by the lowering of the surface due to increasing melt which supports the collapse of englacial conduits and therefore the formation of supraglacial ponds with circular ice cliffs at the side.

Furthermore, we found a negative relationship of the relative cliff area and the strain rates that is contrary to the findings of former studies which assume the formation of ice cliffs at locations with higher strain rates. Our results could therefore suggest that strain rates are not appropriate to detect ice cliffs on a debris-covered glacier.

Considering these findings, we come to the conclusion that the correlations of ice cliff density with the longitudinal gradient, driving stress and glacier velocity confirm the results of previous research and give an idea of the formation of ice cliffs on debris-covered glaciers.

## 8.2 Outlook

To use the ice cliff mapping method developed within this thesis for a larger number of glaciers, further improvements on the automation of the approach can be done. Firstly, the bias correction with empirical quantile mapping could be improved by using Sentinel-2 instead of Landsat-8 data. Sentinel-2 images have a larger swath width and a higher temporal resolution than Landsat-8 scenes. The chance of finding a snow- and cloud-free satellite scene near-contemporaneous to the PlanetScope scene is therefore higher with Sentinel-2 data.

Secondly, the automation of the adapted LSU-s approach can be increased by automatizing the exclusion of cloud cover, snow and shadows from the satellite scenes. PlanetScope satellite images come with a usable data mask file which includes masks for these three disturbance factors (Planet Labs Inc., 2021). These masks can be used for the clipping of the multispectral scenes which are used for the ice cliff mapping. Beside these specific files, there are other approaches to automatically map snow- and cloud-covered areas. A snow mask can be derived by the calculation of the normalized difference snow index (NDSI) (Girona-Mata et al., 2019; Rastner et al., 2019; Kneib et al., 2021b). Clouds and shadows covering the study area can be masked with other automated approaches (Chen et al., 2013; Miles et al., 2017; Zhu et al., 2015; Kneib et al., 2021b). Automatizing these processes is especially important when mapping ice cliffs at regional scale with an increased number of glaciers.

Furthermore, the post processing of the ice cliff maps as the last step of the cliff mapping approach can be further automated by finding an individual threshold for each scene. The threshold could be automatically derived by a statistic-based method considering natural breaks in the distributions of the mean ln(scale) object values.

In a next step, the transferability of the adapted LSU-s approach beyond the Himalayan mountains can be evaluated by testing the method for heterogeneous sites in different climate regimes and with variable lithology. We assume that further adjustment to the LSU-s is needed to use it for the mapping of ice cliffs in other mountain ranges. If the automated ice cliff mapping is successful for glaciers with different surface characteristics and lithology, a world wide dataset with ice cliff outlines of numerous debris-covered glaciers for different points in time could be created. This dataset can than be used for further analysis of the ice cliff distribution of a single glacier or at larger scales.

The research on the ice cliff formation processes and ice cliff dynamics using the final ice cliff distributions of this study can be advanced by combining the ice cliff outlines with a DEM. With this, the aspect and the real area of the ice cliffs could be calculated. This values support the study of the ice cliff formation and dynamics at glacier scale. Furthermore, the calculation of the aspect and additionally the curvature horizontal to the surface could help to classify the ice cliffs as belonging to one of the three categories: lateral ice cliffs which are perpendicular to the flow line, longitudinal ice cliffs positioned along the flow line and partially or completely circular ice cliffs. This classification could be a key element for further ice cliff research.

# Bibliography

Airbus Defence & Space (2021). Pléiades Imagery User Guide.

Anderson, L. S., Armstrong, W. H., Anderson, R. S., and Buri, P. (2021). Debris cover and the thinning of Kennicott Glacier, Alaska: In situ measurements, automated ice cliff delineation and distributed melt estimates. *Cryosphere*, 15(1):265–282.

Azam, M. F., Wagnon, P., Berthier, E., Vincent, C., Fujita, K., and Kargel, J. S. (2018). Review of the status and mass changes of Himalayan-Karakoram glaciers. *Journal of Glaciology*, 64(243):61–74.

Benn, D. I., Bolch, T., Hands, K., Gulley, J., Luckman, A., Nicholson, L. I., Quincey, D., Thompson, S., Toumi, R., and Wiseman, S. (2012). Response of debris-covered glaciers in the Mount Everest region to recent warming, and implications for outburst flood hazards. *Earth-Science Reviews*, 114(1-2):156–174.

Benn, D. I., Wiseman, S., and Hands, K. A. (2001). Growth and drainage of supraglacial lakes on debris-mantled Ngozumpa Glacier, Khumbu Himal, Nepal. *Journal of Glaciology*, 47(159):626–638.

Beyer, R. A., Alexandrov, O., and McMichael, S. (2018). The Ames Stereo Pipeline: NASA's Open Source Software for Deriving and Processing Terrain Data. *Earth and Space Science*, 5(9):537–548.

Bhattacharya, A., Bolch, T., Mukherjee, K., King, O., Menounos, B., Kapitsa, V., Neckel, N., Yang, W., and Yao, T. (2021). High Mountain Asian glacier response to climate revealed by multi-temporal satellite observations since the 1960s. *Nature Communications*, 12(1):1–13.

Bhattacharya, A., Bolch, T., Mukherjee, K., Pieczonka, T., Kropáček, J., and Buchroithner, M. F. (2016). Overall recession and mass budget of Gangotri Glacier, Garhwal Himalayas, from 1965 to 2015 using remote sensing data. *Journal of Glaciology*, 62(236):1115–1133.

Bolch, T., Kulkarni, A., Kääb, A., Huggel, C., Paul, F., Cogley, J. G., Frey, H., Kargel, J. S., Fujita, K., Scheel, M., Bajracharya, S., and Stoffel, M. (2012). The state and fate of himalayan glaciers. *Science*, 336(6079):310–314.

Brun, F., Wagnon, P., Berthier, E., Jomelli, V., Maharjan, S. B., Shrestha, F., and Kraaijenbrink, P. D. (2019). Heterogeneous Influence of Glacier Morphology on the Mass Balance Variability in High Mountain Asia. *Journal of Geophysical Research: Earth Surface*, 124(6):1331–1345.

Brun, F., Wagnon, P., Berthier, E., Shea, J. M., Immerzeel, W. W., Kraaijenbrink, P. D., Vincent, C., Reverchon, C., Shrestha, D., and Arnaud, Y. (2018). Ice cliff contribution to the tongue-wide ablation of Changri Nup Glacier, Nepal, central Himalaya. *Cryosphere*, 12(11):3439–3457.

Buri, P., Miles, E. S., Steiner, J. F., Immerzeel, W. W., Wagnon, P., and Pellicciotti, F. (2016). A physically based 3-D model of ice cliff evolution over debris-covered glaciers. *Journal of Geophysical Research: Earth Surface*, 121(12):2471–2493.

Buri, P., Miles, E. S., Steiner, J. F., Ragettli, S., and Pellicciotti, F. (2021). Supraglacial Ice Cliffs Can Substantially Increase the Mass Loss of Debris-Covered Glaciers. *Geophysical Research Letters*, 48(6):1–11.

Buri, P. and Pellicciotti, F. (2018). Aspect controls the survival of ice cliffs on debris-covered glaciers. *Proceedings of the National Academy of Sciences of the United States of America*, 115(17):4369–4374.

Cannon, A. J. (2018). Multivariate quantile mapping bias correction: an N-dimensional probability density function transform for climate model simulations of multiple variables. *Climate Dynamics*, 50:31–49.

Chen, W., Fukui, H., Doko, T., and Gu, X. (2013). Improvement of glacial lakes detection under shadow environment using ASTER data in Himalayas, Nepal. *Chinese Geographical Science*, 23(2):216–226.

Dehecq, A., Gourmelen, N., Gardner, A. S., Brun, F., Goldberg, D., Nienow, P. W., Berthier, E., Vincent, C., Wagnon, P., and Trouvé, E. (2019). Twenty-first century glacier slowdown driven by mass loss in High Mountain Asia. *Nature Geoscience*, 12(1):22–27.

Enayati, M., Bozorg-Haddad, O., Bazrafshan, J., Hejabi, S., and Chu, X. (2021). Bias correction capabilities of quantile mapping methods for rainfall and temperature variables. *Journal of Water and Climate Change*, 12(2):401–419.

Farinotti, D., Huss, M., Fürst, J. J., Landmann, J., Machguth, H., Maussion, F., and Pandit, A. (2019). A consensus estimate for the ice thickness distribution of all glaciers on Earth. *Nature Geoscience*, 12(3):168–173.

Farinotti, D., Immerzeel, W. W., de Kok, R. J., Quincey, D. J., and Dehecq, A. (2020). Manifestations and mechanisms of the Karakoram glacier Anomaly. *Nature Geoscience*, 13(1):8–16.

Feigenwinter, I., Kotlarski, S., Casanueva, A., Fischer, A., Schwierz, C., and Liniger, M. A. (2018). Exploring quantile mapping as a tool to produce user tailored climate scenarios for Switzerland. Technical Report 270.

Fujita, K., Suzuki, R., Nuimura, T., and Sakai, A. (2008). Performance of ASTER and SRTM DEMs, and their potential for assessing glacial lakes in the Lunana region, Bhutan Himalaya. *Journal of Glaciology*, 54(185):220–228.

Fyffe, C. L., Woodget, A. S., Kirkbride, M. P., Deline, P., Westoby, M. J., and Brock, B. W. (2020). Processes at the margins of supraglacial debris cover: Quantifying dirty ice ablation and debris redistribution. *Earth Surface Processes and Landforms*, 45(10):2272–2290.

Gardelle, J., Berthier, E., Arnaud, Y., and Kääb, A. (2013). Region-wide glacier mass balances over the Pamir-Karakoram-Himalaya during 1999-2011. *Cryosphere*, 7(4):1263–1286.

Gardner, A. S., Fahnestock, M. A., and Scambos, T. A. (2020). ITS_LIVE Regional Glacier and Ice Sheet Surface Velocities. Data archived at National Snow and Ice Data Center.

Girona-Mata, M., Miles, E. S., Ragettli, S., and Pellicciotti, F. (2019). High-Resolution Snowline Delineation From Landsat Imagery to Infer Snow Cover Controls in a Himalayan Catchment. *Water Resources Research*, 55(8):6754–6772.

Herreid, S. and Pellicciotti, F. (2018). Automated detection of ice cliffs within supraglacial debris cover. *Cryosphere*, 12(5):1811–1829.

Herreid, S. and Pellicciotti, F. (2020). The state of rock debris covering Earth's glaciers. *Nature Geoscience*, 13(9):621–627.

Hirschmüller, H. (2008). Stereo processing by semiglobal matching and mutual information. *IEEE Transactions on Pattern Analysis and Machine Intelligence*, 30(2):328–341.

Hock, R., Rasul, G., Adler, C., Cáceres, B., Gruber, S., Hirabayashi, Y., Jackson, M., Kääb, A., Kang, S., Kutuzov, S., Milner, A., Molau, U., Morin, S., Orlove, B., and Steltzer, H. I. (2019). High Mountain Areas. IPCC Special Report on the Ocean and Cryosphere in a Changing Climate. In Pörtner, H.-O., Roberts, D., Masson-Delmotte, V., Zhai, P., Tignor, M., Poloczanska, E., Mintenbeck, K., Alegría, A., Nicolai, M., Okem, A., Petzold, J., Rama, B., and Weyer, N., editors, *IPCC Special Report on the Ocean and Cryosphere in a Changing Climate*, pages 131–202.

Hugonnet, R., McNabb, R., Berthier, E., Menounos, B., Nuth, C., Girod, L., Farinotti, D., Huss, M., Dussaillant, I., Brun, F., and Kääb, A. (2021). Accelerated global glacier mass loss in the early twenty-first century. *Nature*, 592(7856):726–731.

Huss, M. and Hock, R. (2018). Global-scale hydrological response to future glacier mass loss. *Nature Climate Change*, 8(2):135–140.

Immerzeel, W. W., Kraaijenbrink, P. D., Shea, J. M., Shrestha, A. B., Pellicciotti, F., Bierkens, M. F., and De Jong, S. M. (2014). High-resolution monitoring of Himalayan glacier dynamics using unmanned aerial vehicles. *Remote Sensing of Environment*, 150:93–103.

Immerzeel, W. W., Lutz, A. F., Andrade, M., Bahl, A., Biemans, H., Bolch, T., Hyde, S., Brumby, S., Davies, B. J., Elmore, A. C., Emmer, A., Feng, M., Fernández, A., Haritashya, U., Kargel, J. S., Koppes, M., Kraaijenbrink, P. D., Kulkarni, A. V., Mayewski, P. A., Nepal, S., Pacheco, P., Painter, T. H., Pellicciotti, F., Rajaram, H., Rupper, S., Sinisalo, A., Shrestha, A. B., Viviroli, D., Wada, Y., Xiao, C., Yao, T., and Baillie, J. E. (2020). Importance and vulnerability of the world's water towers. *Nature*, 577(7790):364–369.

Kääb, A., Berthier, E., Nuth, C., Gardelle, J., and Arnaud, Y. (2012). Contrasting patterns of early twenty-first-century glacier mass change in the Himalayas. *Nature*, 488(7412):495–498.

King, O., Turner, A. G., Quincey, D. J., and Carrivick, J. L. (2020). Morphometric evolution of Everest region debris-covered glaciers. *Geomorphology*, 371:107422.

Kneib, M., Miles, E., Buri, P., Molnar, P., McCarthy, M., Fugger, S., and Pellicciotti, F. (2021a). Interannual Dynamics of Ice Cliff Populations on Debris-Covered Glaciers from Remote Sensing Observations and Stochastic Modeling. *Journal of Geophysical Research: Earth Surface (unpublished).*

Kneib, M., Miles, E. S., Jola, S., Buri, P., Herreid, S., Bhattacharya, A., Watson, C. S., Bolch, T., Quincey, D., and Pellicciotti, F. (2021b). Mapping ice cliffs on debris-covered glaciers using multispectral satellite images. *Remote Sensing of Environment*, 253:112201.

Kopačková, V. and Hladíková, L. (2014). Applying spectral unmixing to determine surface water parameters in a mining environment. *Remote Sensing*, 6(11):11204–11224.

Kraaijenbrink, P. D., Bierkens, M. F., Lutz, A. F., and Immerzeel, W. W. (2017). Impact of a global temperature rise of 1.5 degrees Celsius on Asia's glaciers. *Nature*, 549(7671):257–260.

Kraaijenbrink, P. D., Shea, J. M., Pellicciotti, F., Jong, S. M., and Immerzeel, W. W. (2016). Object-based analysis of unmanned aerial vehicle imagery to map and characterise surface features on a debris-covered glacier. *Remote Sensing of Environment*, 186:581–595.

Messerli, A. and Grinsted, A. (2015). Image georectification and feature tracking toolbox: ImGRAFT. *Geoscientific Instrumentation, Methods and Data Systems*, 4(1):23–34.

Miles, E., McCarthy, M., Dehecq, A., Kneib, M., Fugger, S., and Pellicciotti, F. (2021). Health and sustainability of glaciers in High Mountain Asia. *Nature Communications*, 12:2868.

Miles, E. S., Willis, I., Buri, P., Steiner, J. F., Arnold, N. S., and Pellicciotti, F. (2018). Surface Pond Energy Absorption Across Four Himalayan Glaciers Accounts for 1/8 of Total Catchment Ice Loss. *Geophysical Research Letters*, 45(19):464–10.

Miles, E. S., Willis, I. C., Arnold, N. S., Steiner, J., and Pellicciotti, F. (2017). Spatial, seasonal and interannual variability of supraglacial ponds in the Langtang Valley of Nepal, 1999-2013. *Journal of Glaciology*, 63(237):88–105.

Mölg, N., Bolch, T., Walter, A., and Vieli, A. (2019). Unravelling the evolution of Zmuttgletscher and its debris cover since the end of the Little Ice Age. *Cryosphere*, 13(7):1889–1909.

Mölg, N., Ferguson, J., Bolch, T., and Vieli, A. (2020). On the influence of debris cover on glacier morphology: How high-relief structures evolve from smooth surfaces. *Geomorphology*, 357:107092.

Moore, P. L. (2018). Stability of supraglacial debris. *Earth Surface Processes and Landforms*, 43(1):285–297.

Naito, N., Suzuki, R., Komori, J., Matsuda, Y., Yamaguchi, S., Sawagaki, T., Tshering, P., and Ghalley, K. S. (2012). Recent Glacier Shrinkages in the Lunana Region , Bhutan Himalayas. *Global Environmental Research*, 16(2012):13–22.

NASA/METI/AIST/Japan Spacesystems and U.S./Japan ASTER Science Team (2019). ASTER Global Digital Elevation Model V003. https://doi.org/10.5067/ASTER/ASTGTM.003. Last accessed on August 25, 2021.

Nicholson, L. I., McCarthy, M., Pritchard, H. D., and Willis, I. (2018). Supraglacial debris thickness variability: Impact on ablation and relation to terrain properties. *Cryosphere*, 12(12):3719–3734.

Nye, J. F. (1959). A Method of Determining the Strain-Rate Tensor at the Surface of a Glacier. *Journal of Glaciology*, 3(25):409–419.

Östrem, G. (1959). Ice Melting under a Thin Layer of Moraine, and the Existence of Ice Cores in Moraine Ridges. *Geografiska Annaler*, 41(4):228–230.

Pellicciotti, F., Stephan, C., Miles, E., Herreid, S., Immerzeel, W. W., and Bolch, T. (2015). Mass-balance changes of the debris-covered glaciers in the Langtang Himal, Nepal, from 1974 to 1999. *Journal of Glaciology*, 61(226):373–386.

Planet Labs Inc. (2021). PlanetScope Product Specifications. https://assets.planet.com/docs/Planet_PSScene_Imagery_Product_Spec_June_2021.pdf. Last accessed on September 15, 2021.

Planet Team (2017). Planet Application Program Interface: In Space for Life on Earth. https://api.planet.com. Last accessed on June 30, 2021.

Pritchard, H. D. (2019). Asia's shrinking glaciers protect large populations from drought stress. *Nature*, 569(7758):649–654.

Ragettli, S., Immerzeel, W. W., and Pellicciotti, F. (2016). Contrasting climate change impact on river flows from high-altitude catchments in the Himalayan and Andes Mountains. *Proceedings of the National Academy of Sciences of the United States of America*, 113(33):9222–9227.

Rastner, P., Prinz, R., Notarnicola, C., Nicholson, L., Sailer, R., Schwaizer, G., and Paul, F. (2019). On the automated mapping of snow cover on glaciers and calculation of snow line altitudes from multi-temporal Landsat data. *Remote Sensing*, 11(12):1–24.

Reid, T. D. and Brock, B. W. (2014). Assessing ice-cliff backwasting and its contribution to total ablation of debris-covered Miage glacier, Mont Blanc massif, Italy. *Journal of Glaciology*, 60(219):3–13.

RGI Consortium (2017). Randolph Glacier Inventory – A Dataset of Global Glacier Outlines: Version 6.0: Technical Report. https://doi.org/10.7265/N5-RGI-60. Last accessed on June 30, 2021.

Rounce, D. R., Hock, R., and Shean, D. E. (2020). Glacier Mass Change in High Mountain Asia Through 2100 Using the Open-Source Python Glacier Evolution Model (PyGEM). *Frontiers in Earth Science*, 7:331.

Sakai, A., Nakawo, M., and Fujita, K. (2002). Distribution Characteristics and Energy Balance of Ice Cliffs on Debris-covered Glaciers, Nepal Himalaya. *Arctic, Antarctic, and Alpine Research*, 34(1):12–19.

Salerno, F., Thakuri, S., D'Agata, C., Smiraglia, C., Manfredi, E. C., Viviano, G., and Tartari, G. (2012). Glacial lake distribution in the Mount Everest region: Uncertainty of measurement and conditions of formation. *Global and Planetary Change*, 92-93:30–39.

Salerno, F., Thakuri, S., Tartari, G., Nuimura, T., Sunako, S., Sakai, A., and Fujita, K. (2017). Debris-covered glacier anomaly? Morphological factors controlling changes in the mass balance, surface area, terminus position, and snow line altitude of Himalayan glaciers. *Earth and Planetary Science Letters*, 471:19–31.

Scherler, D., Wulf, H., and Gorelick, N. (2018). Global Assessment of Supraglacial Debris-Cover Extents. *Geophysical Research Letters*, 45(21):798–11.

Sharp, R. P. (1949). Studies of superglacial debris on valley glaciers. *American Journal of Science*, pages 289–315.

Shean, D. E., Alexandrov, O., Moratto, Z. M., Smith, B. E., Joughin, I. R., Porter, C., and Morin, P. (2016). An automated, open-source pipeline for mass production of digital elevation models (DEMs) from very-high-resolution commercial stereo satellite imagery. *ISPRS Journal of Photogrammetry and Remote Sensing*, 116:101–117.

Steiner, J. F., Buri, P., Miles, E. S., Ragettli, S., and Pellicciotti, F. (2019). Supraglacial ice cliffs and ponds on debris-covered glaciers: Spatio-temporal distribution and characteristics. *Journal of Glaciology*, 65(252):617–632.

Steiner, J. F., Kraaijenbrink, P. D., and Immerzeel, W. W. (2021). Distributed Melt on a Debris-Covered Glacier: Field Observations and Melt Modeling on the Lirung Glacier in the Himalaya. *Frontiers in Earth Science*, 9:678375.

The European Space Agency (2021). Sentinel-2. https://sentinel.esa.int/web/sentinel/missions/sentinel-2. Last accessed on August 25, 2021.

Thompson, S., Benn, D. I., Mertes, J., and Luckman, A. (2016). Stagnation and mass loss on a Himalayan debris-covered glacier: Processes, patterns and rates. *Journal of Glaciology*, 62(233):467–485.

USGS (2021). Landsat Missions: Landsat 8. https://www.usgs.gov/core-science-systems/nli/landsat/landsat-8?qt-science_support_page_related_con=0#qt-science_support_page_related_con. Last accessed on August 25, 2021.

Vincent, C., Wagnon, P., Shea, J. M., Immerzeel, W. W., Kraaijenbrink, P., Shrestha, D., Soruco, A., Arnaud, Y., Brun, F., Berthier, E., and Sherpa, S. F. (2016). Reduced melt on debris-covered glaciers: Investigations from Changri Nup Glacier, Nepal. *Cryosphere*, 10(4):1845–1858.

Viviroli, D., Kummu, M., Meybeck, M., Kallio, M., and Wada, Y. (2020). Increasing dependence of lowland populations on mountain water resources. *Nature Sustainability*, 3(11):917–928.

Watson, C. S., King, O., Miles, E. S., and Quincey, D. J. (2018). Optimising NDWI supraglacial pond classification on Himalayan debris-covered glaciers. *Remote Sensing of Environment*, 217:414–425.

Watson, C. S., Quincey, D. J., Carrivick, J. L., and Smith, M. W. (2017). Ice cliff dynamics in the Everest region of the Central Himalaya. *Geomorphology*, 278:238–251.

Westoby, M. J., Rounce, D. R., Shaw, T. E., Fyffe, C. L., Moore, P. L., Stewart, R. L., and Brock, B. W. (2020). Geomorphological evolution of a debris-covered glacier surface. *Earth Surface Processes and Landforms*, 45(14):3431–3448.

Zhu, Z., Wang, S., and Woodcock, C. E. (2015). Improvement and expansion of the Fmask algorithm: Cloud, cloud shadow, and snow detection for Landsats 4-7, 8, and Sentinel 2 images. *Remote Sensing of Environment*, 159:269–277.

# Appendix

## 10.1 Flow Charts of Ice Cliff Mapping Process

### 10.1.1 Adaptation of LSU-s

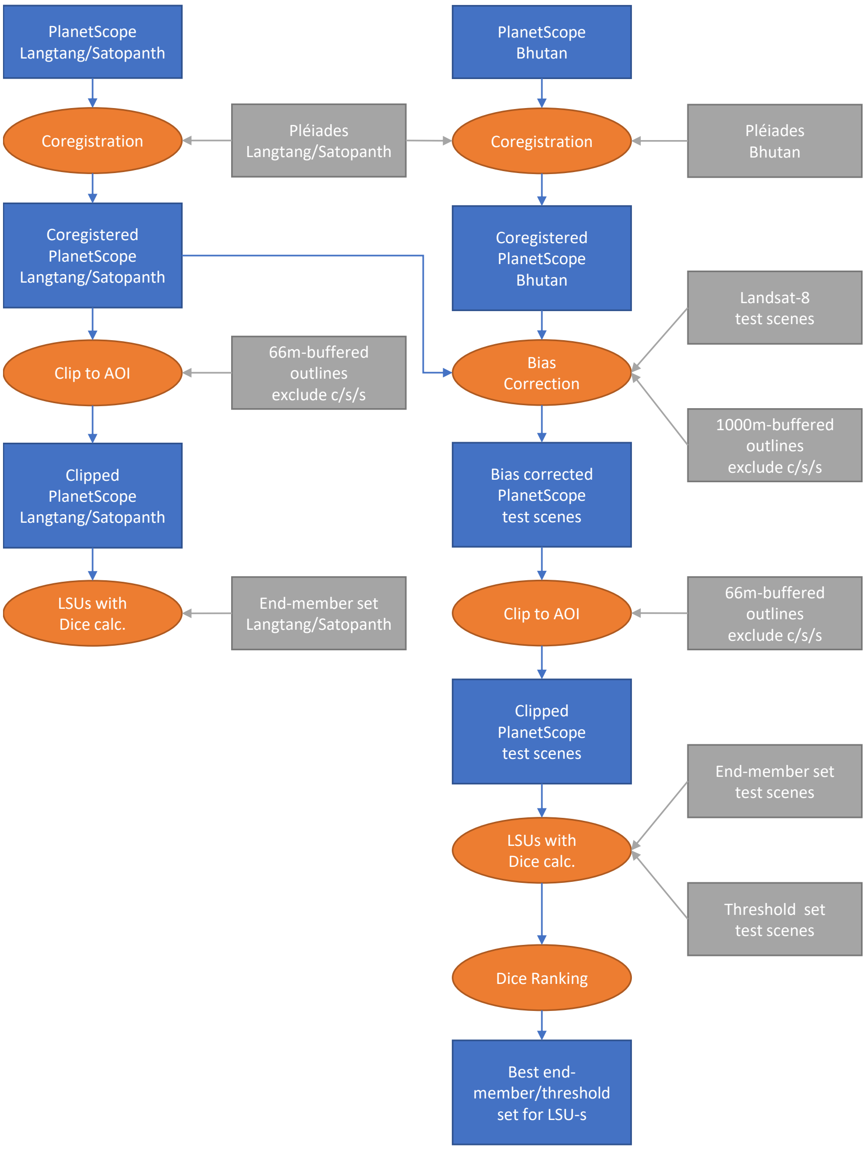

### 10.1.2 Ice Cliff Mapping with LSU-s

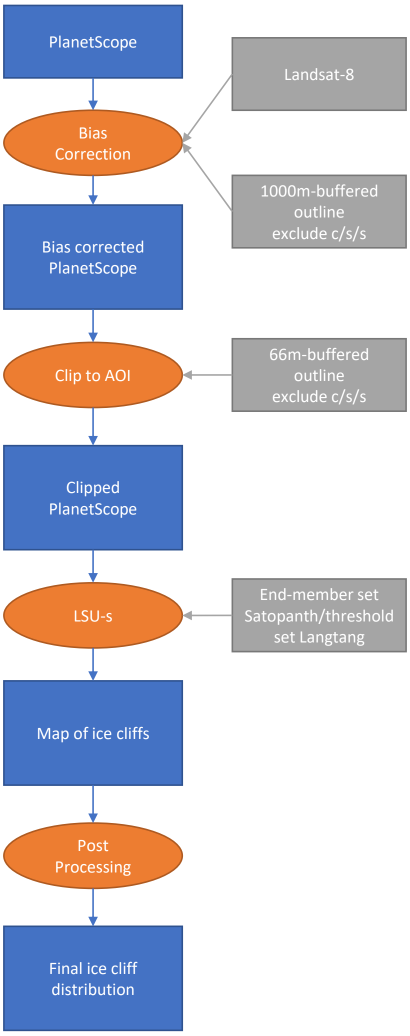

## 10.2 Scatterplots of the Mean Absolute Ln(scale) Object Values

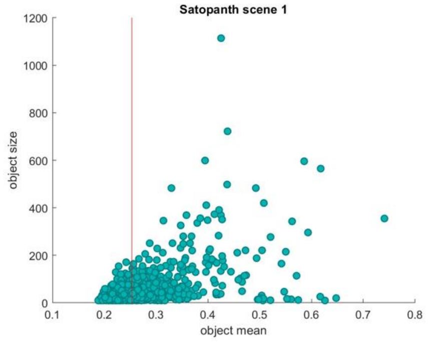

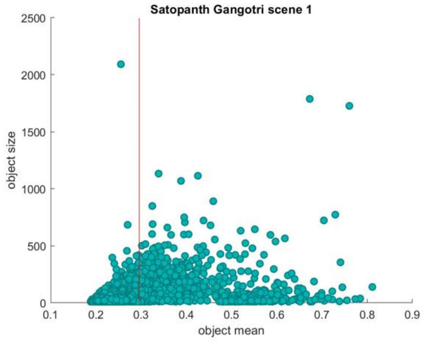

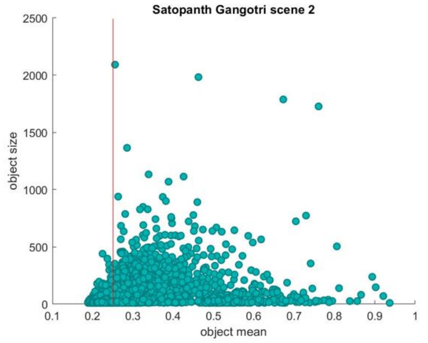

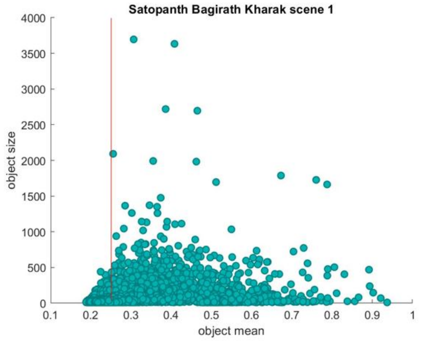

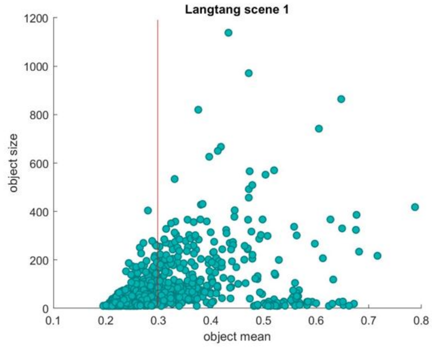

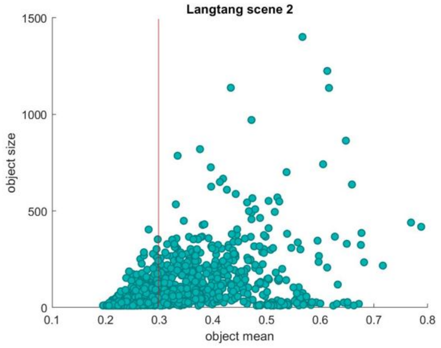

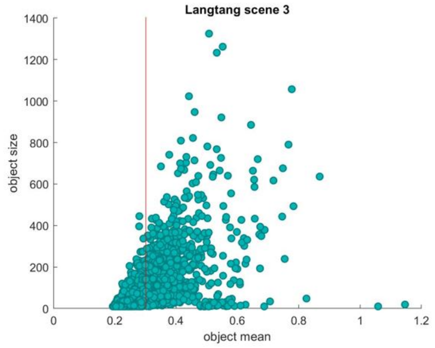

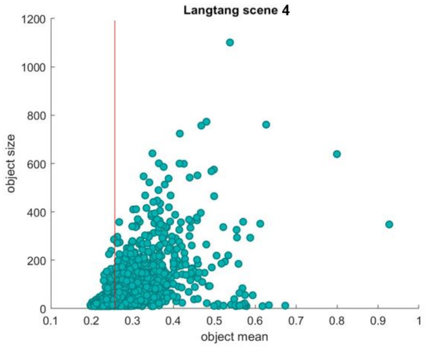

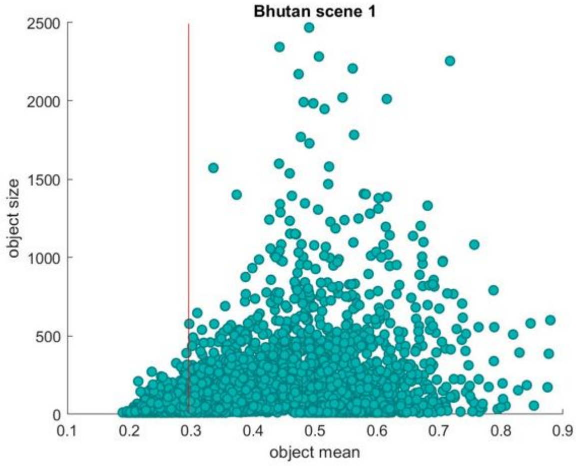
Bhutan scene 1
object size
object mean
0
500
1000
1500
2000
2500
0.1
0.2
0.3
0.4
0.5
0.6
0.7
0.8
0.9

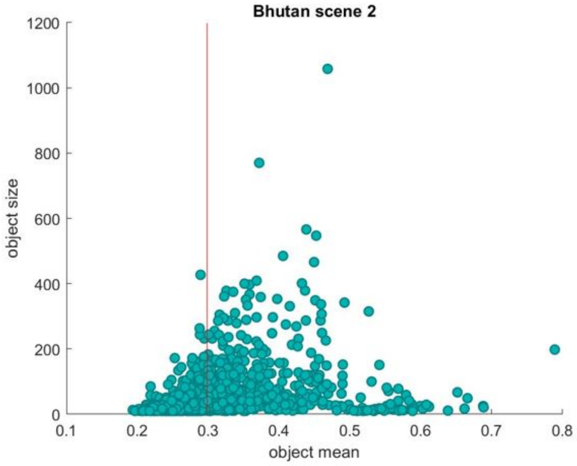
Bhutan scene 2
object size
object mean
0
200
400
600
800
1000
1200
0.1
0.2
0.3
0.4
0.5
0.6
0.7
0.8

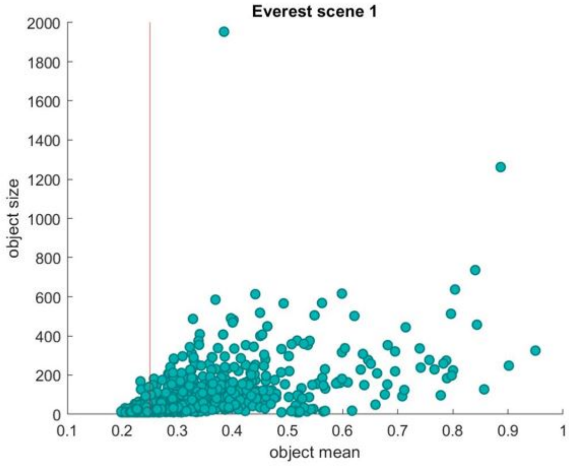
Everest scene 1
object size
object mean
0
200
400
600
800
1000
1200
1400
1600
1800
2000
0.1
0.2
0.3
0.4
0.5
0.6
0.7
0.8
0.9
1

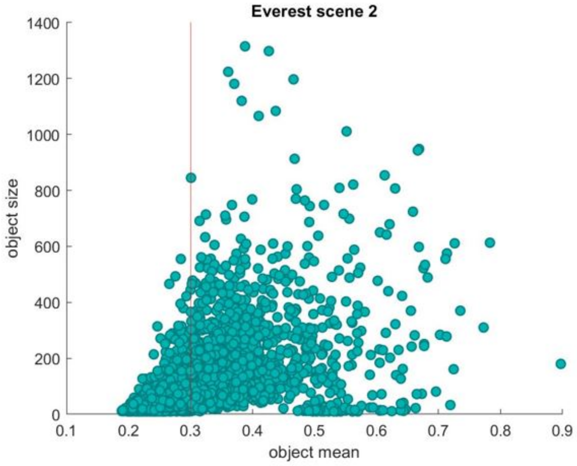
Everest scene 2
object size
object mean
0
200
400
600
800
1000
1200
1400
0.1
0.2
0.3
0.4
0.5
0.6
0.7
0.8
0.9

## 10.3 Final Ice Cliff Maps

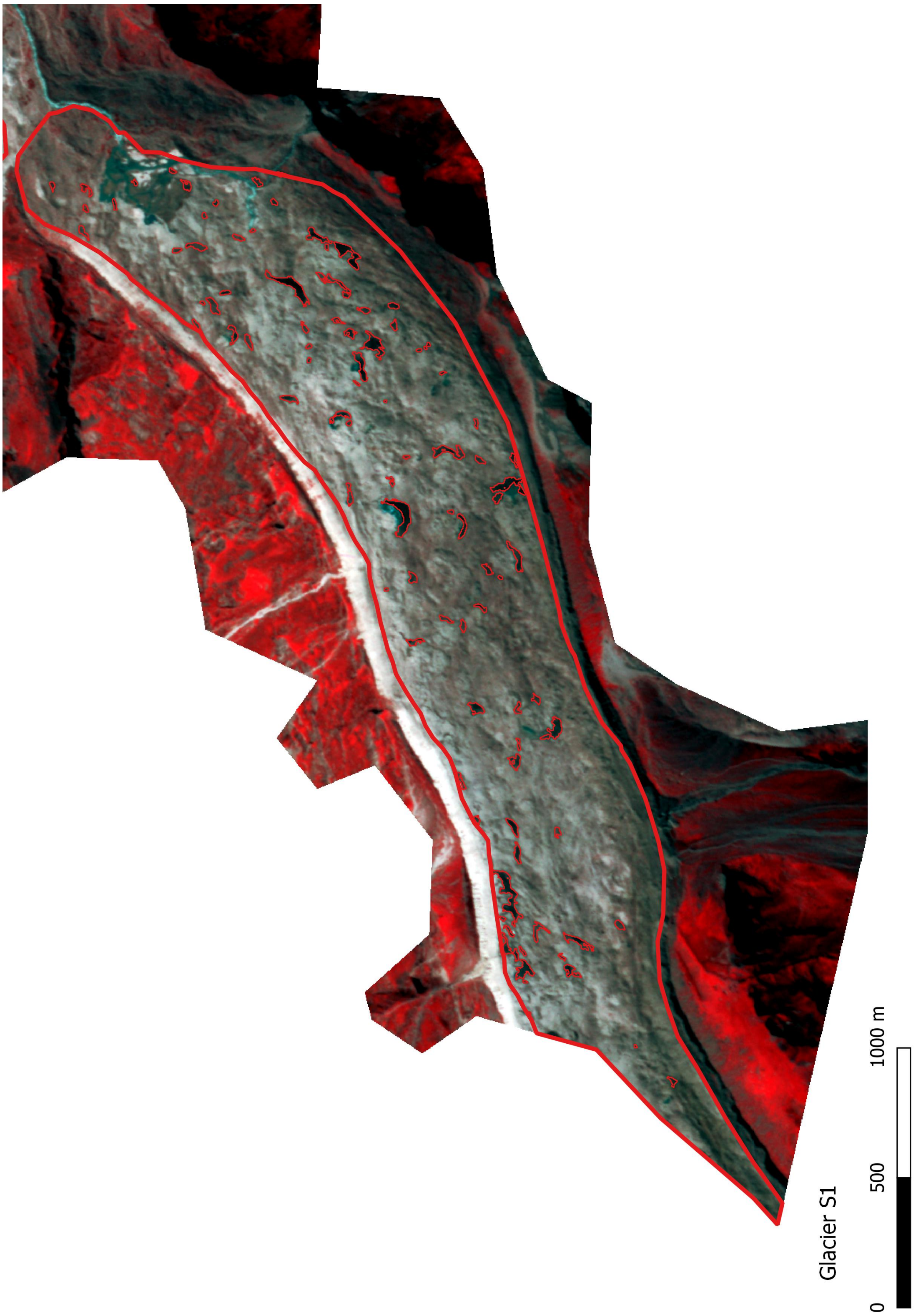

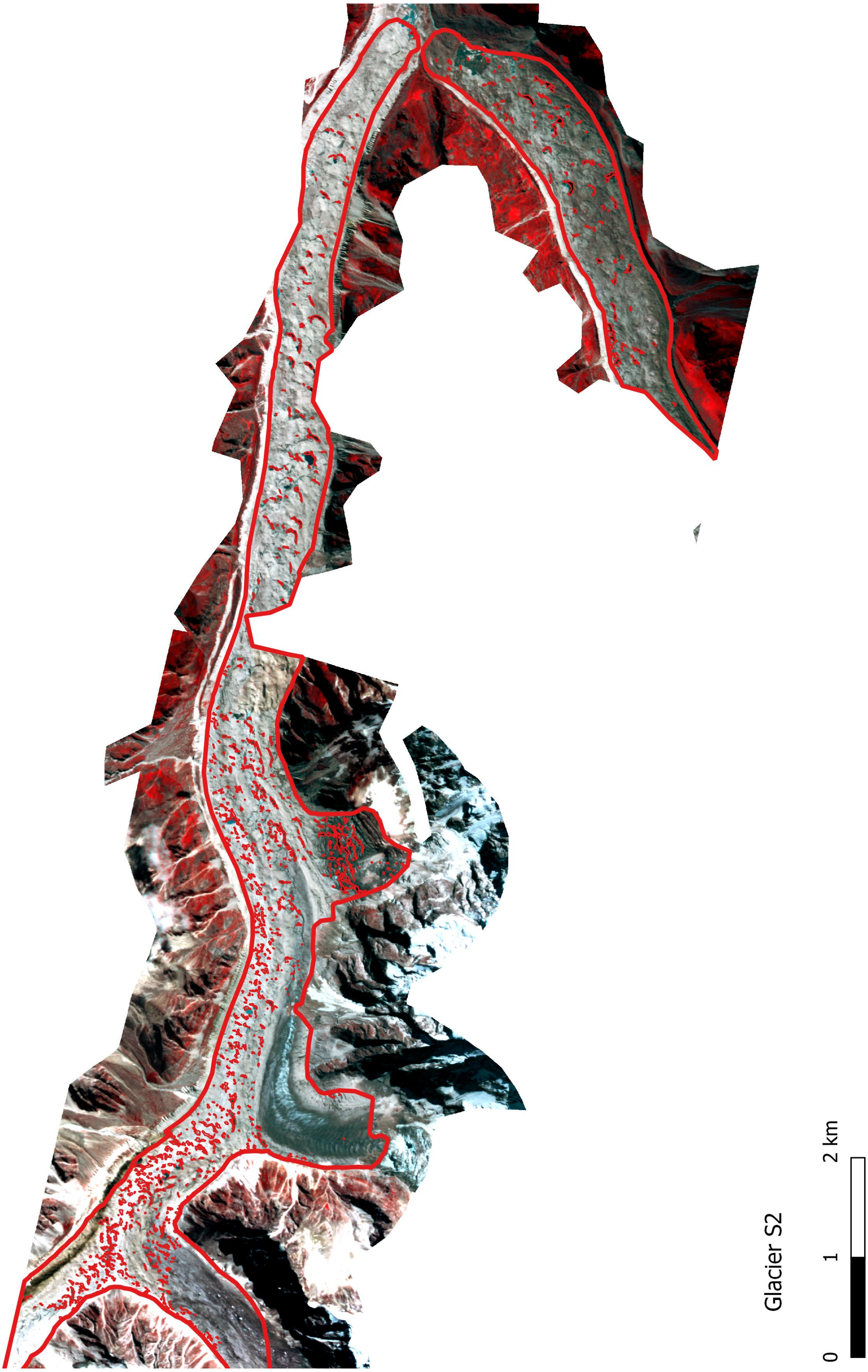
Glacier S2
0
1
2 km


Glacier S3
0
1
2 km

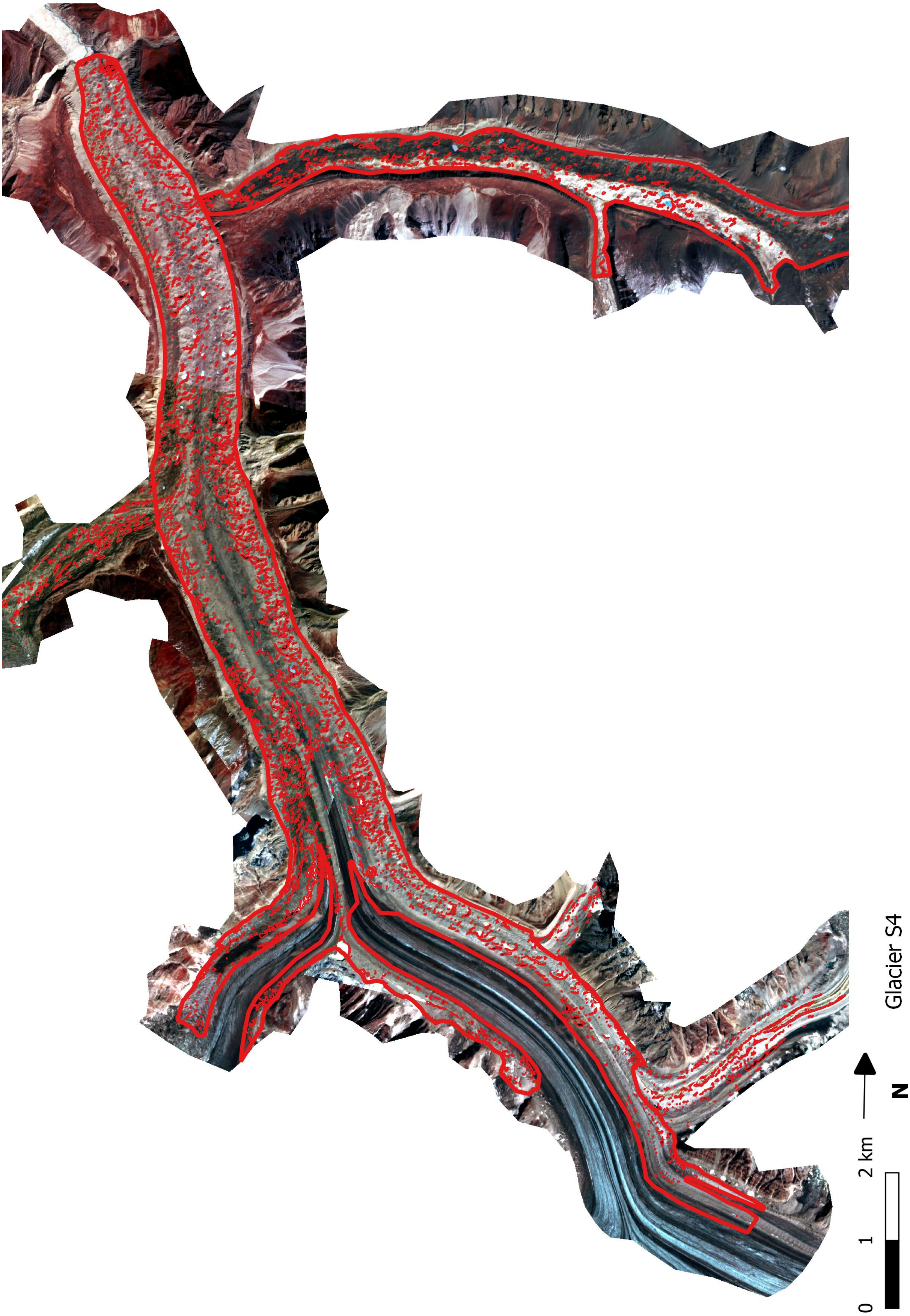
Glacier S4
N
0
1
2 km


Glacier L1
N
0
250
500 m

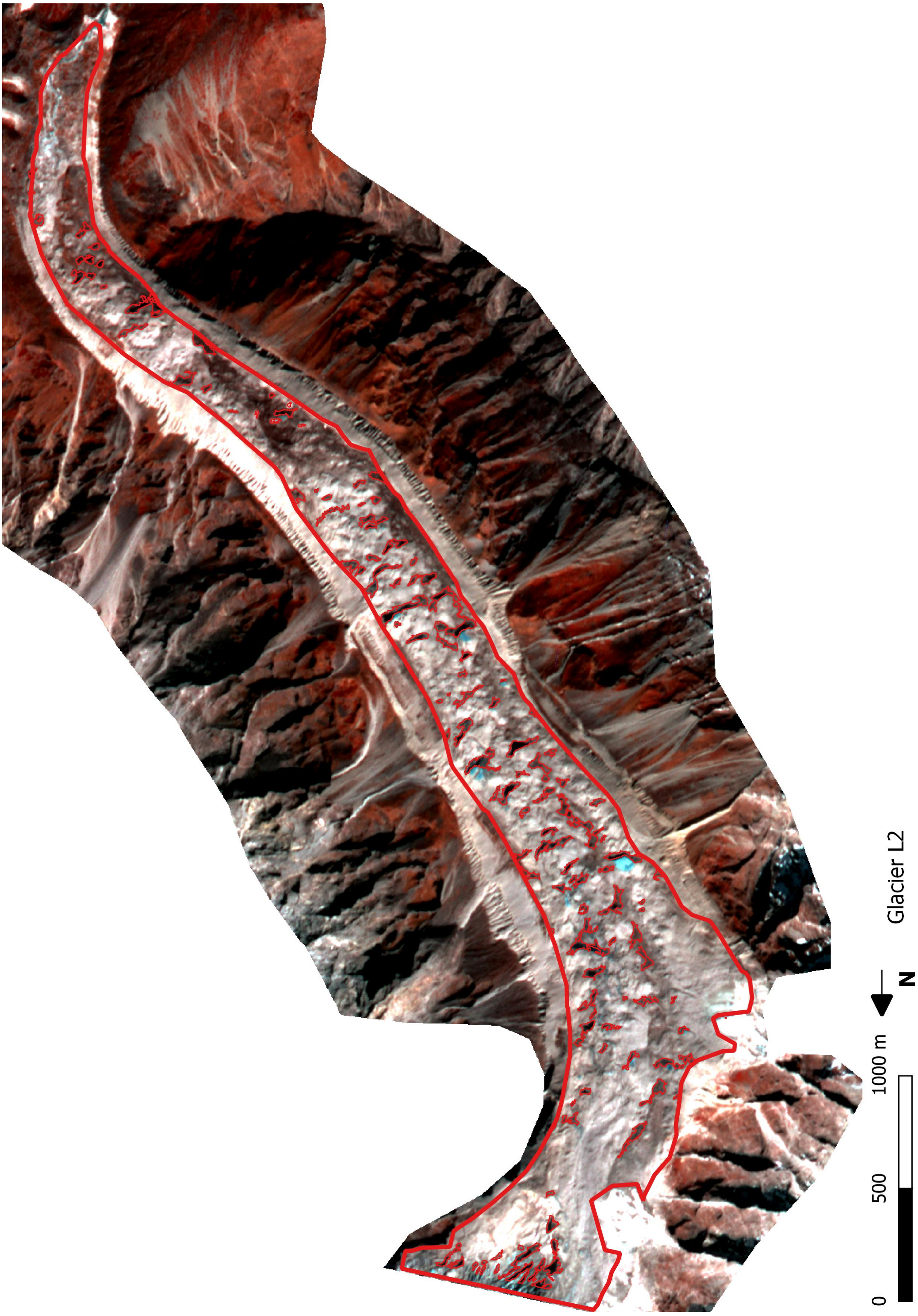
Glacier L2
N
0
500
1000 m


Glacier L3
N
0
1
2 km


Glacier L4
0
750
1500 m

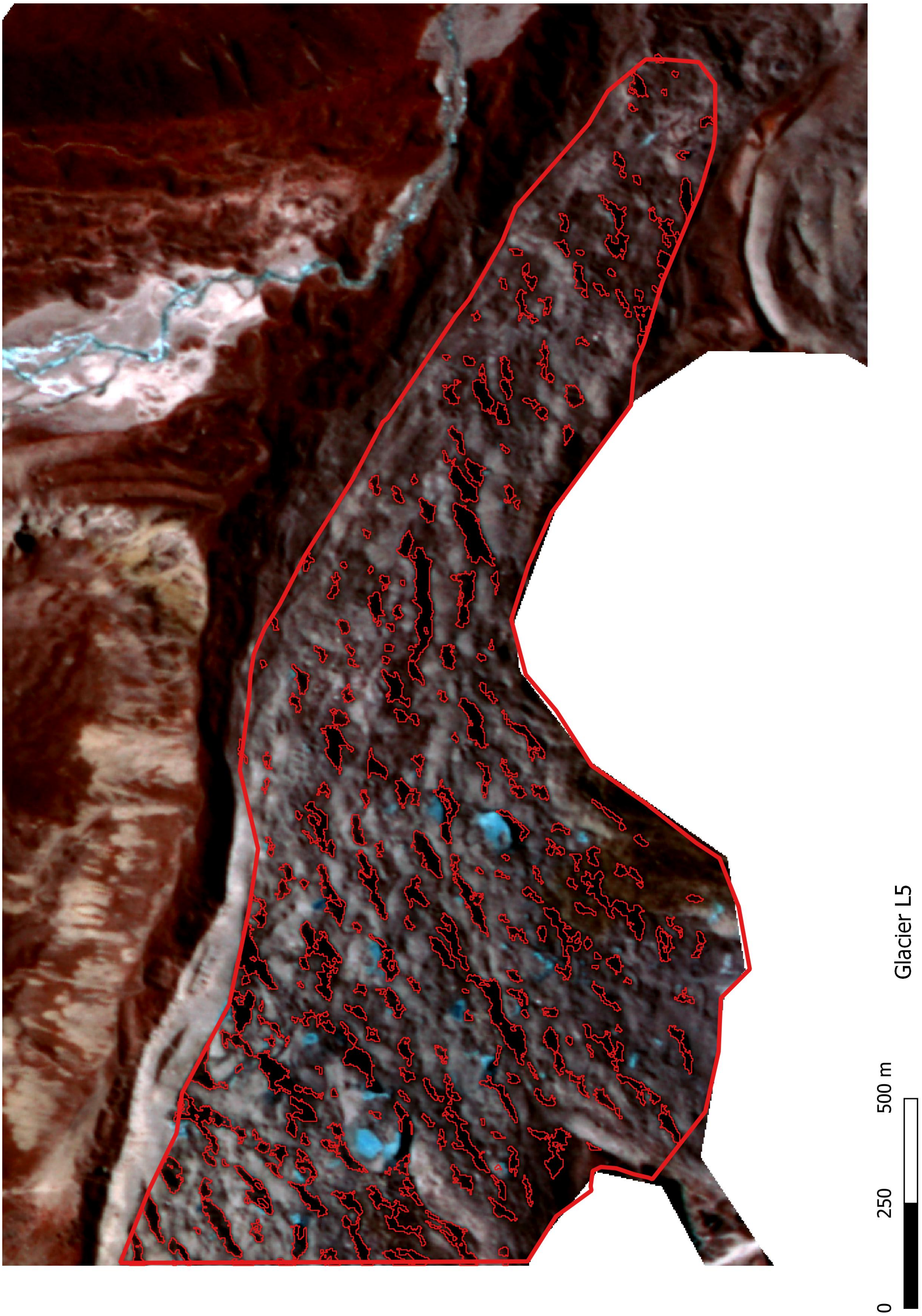
Glacier L5
0
250
500 m

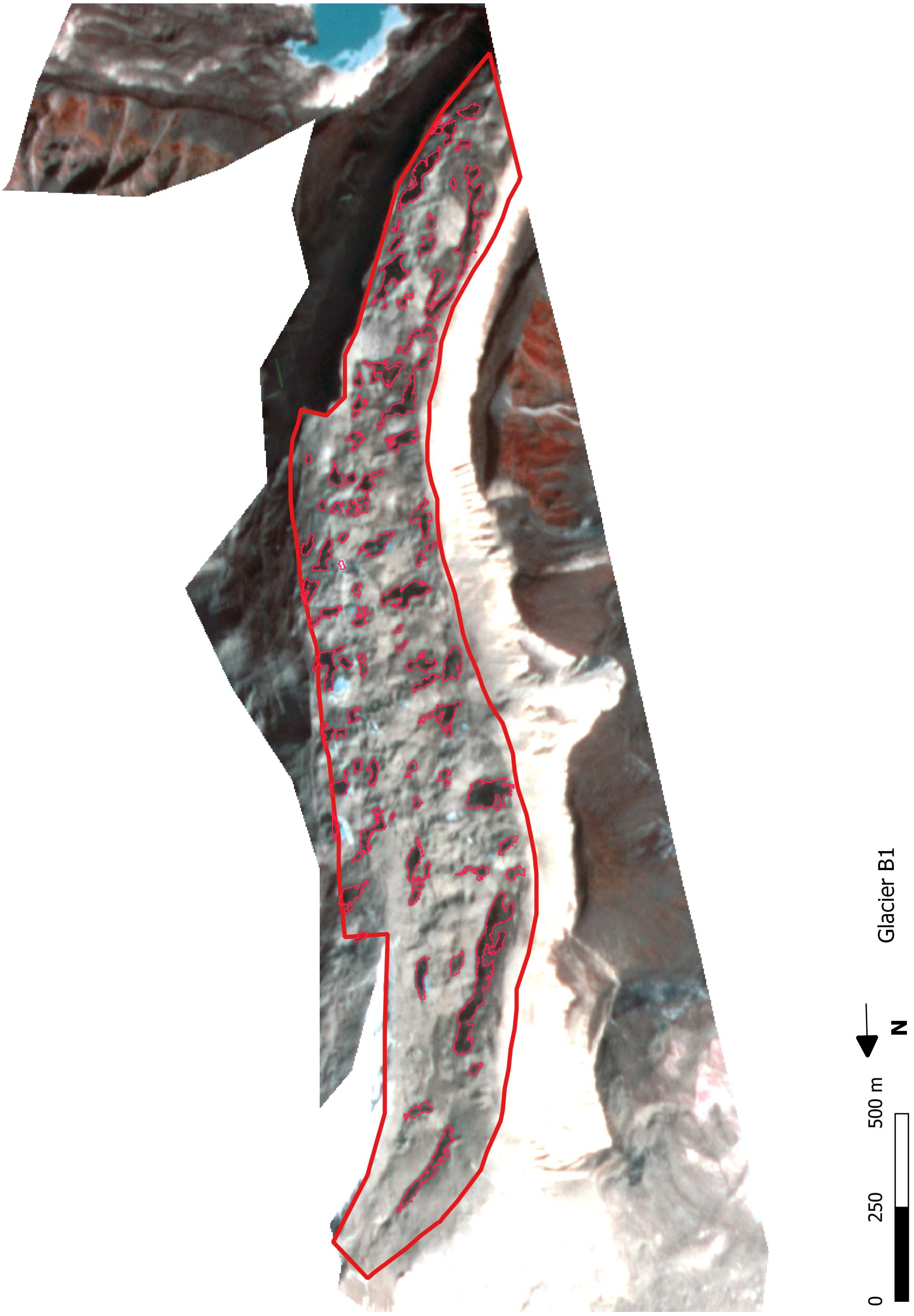
Glacier B1
N
0
250
500 m


Glacier B2
N
0
1
2 km


Glacier B3
N
0
750
1500 m


Glacier B4
N
0
1
2 km


Glacier B5
0
250
500 m

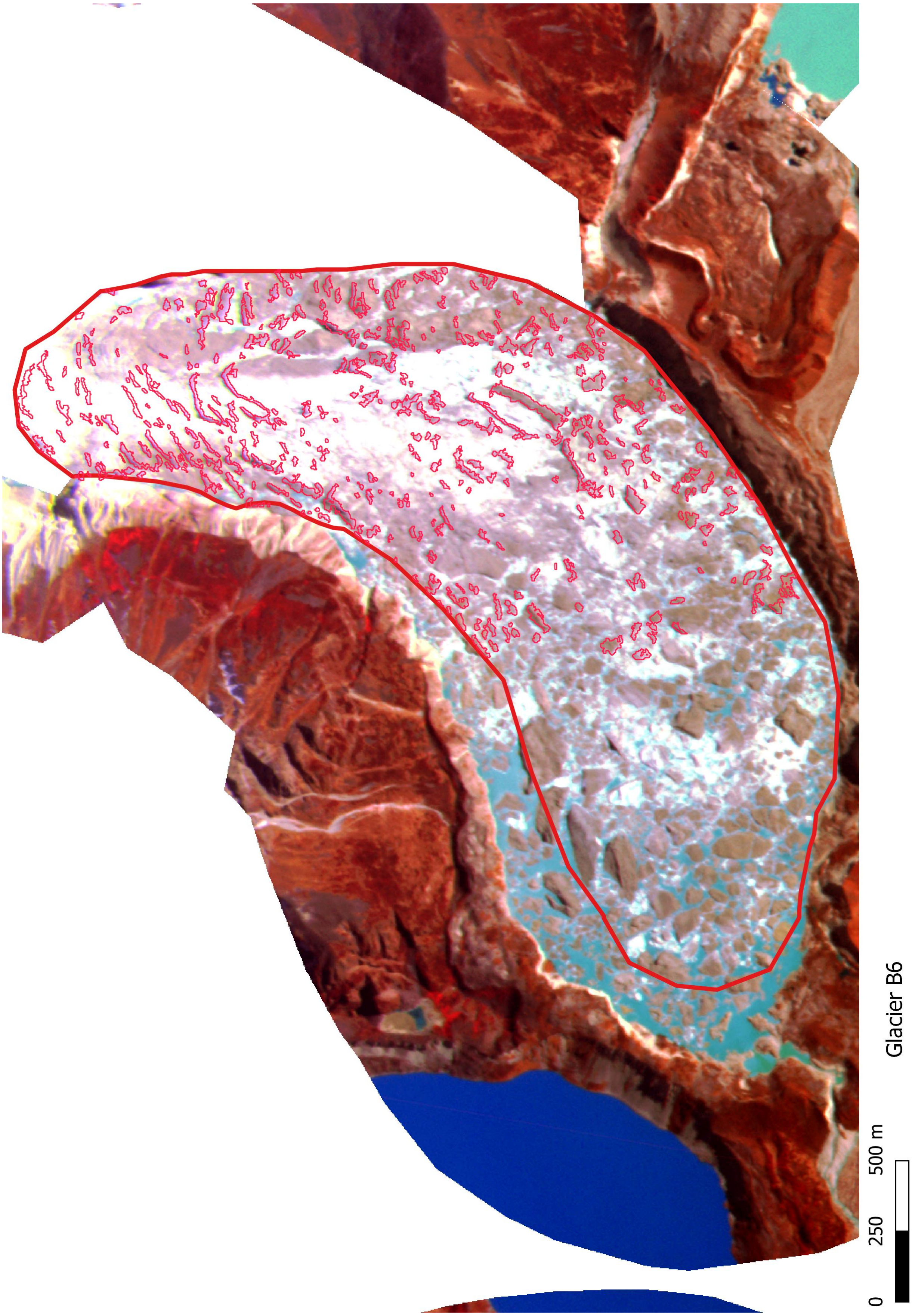
Glacier B6
0
250
500 m

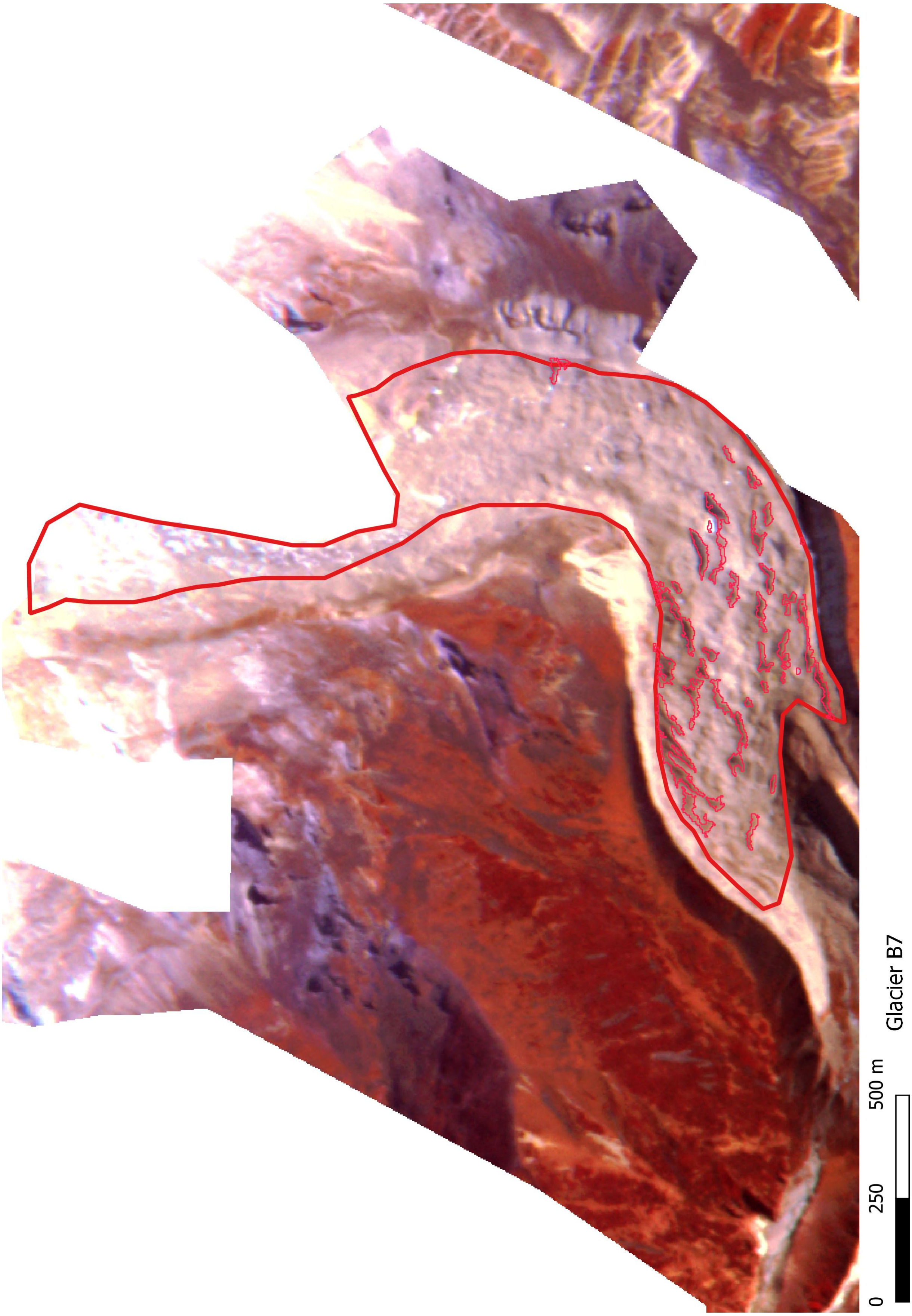
Glacier B7
0
250
500 m


Glacier K1
0
250
500 m

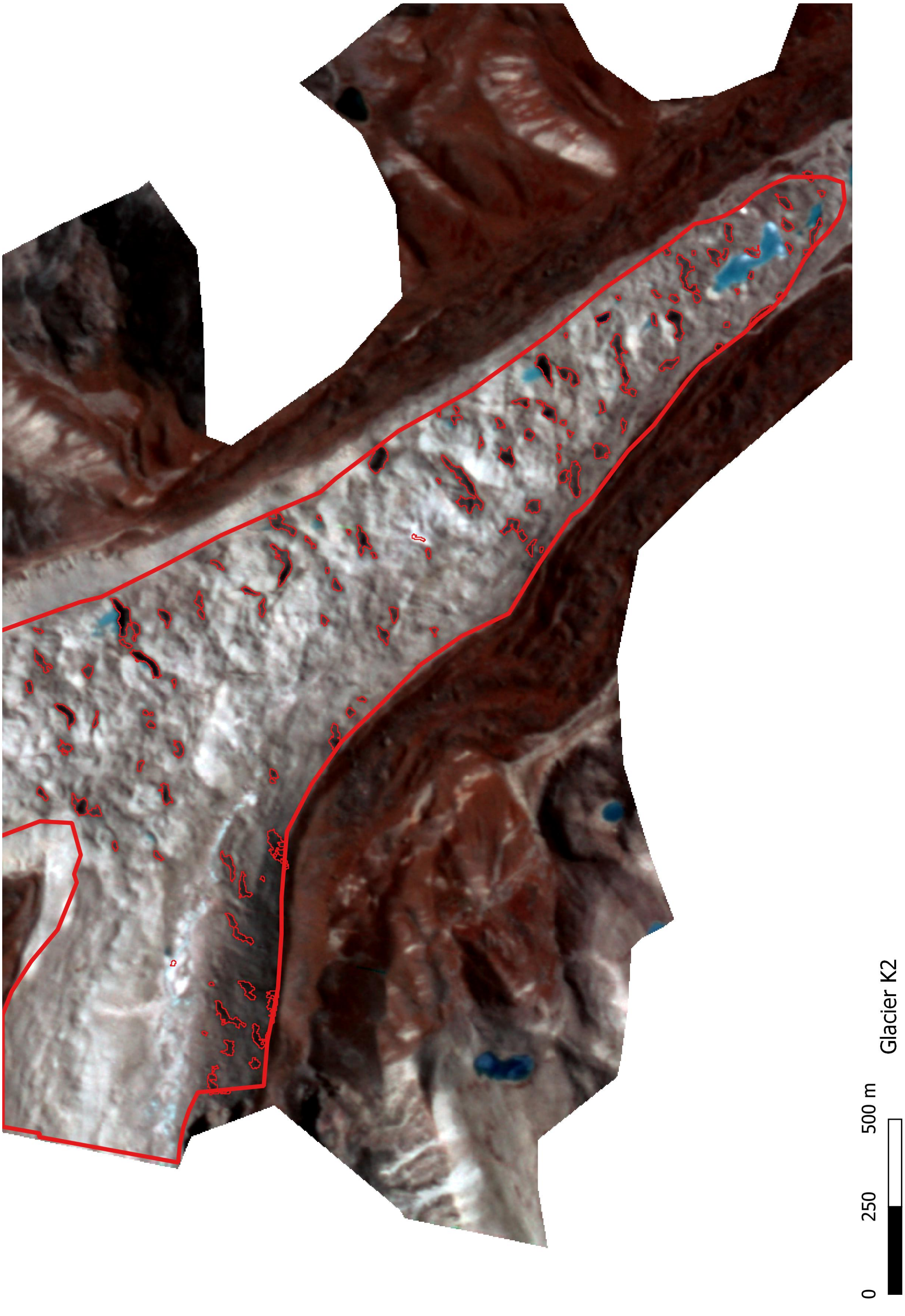
Glacier K2
0
250
500 m

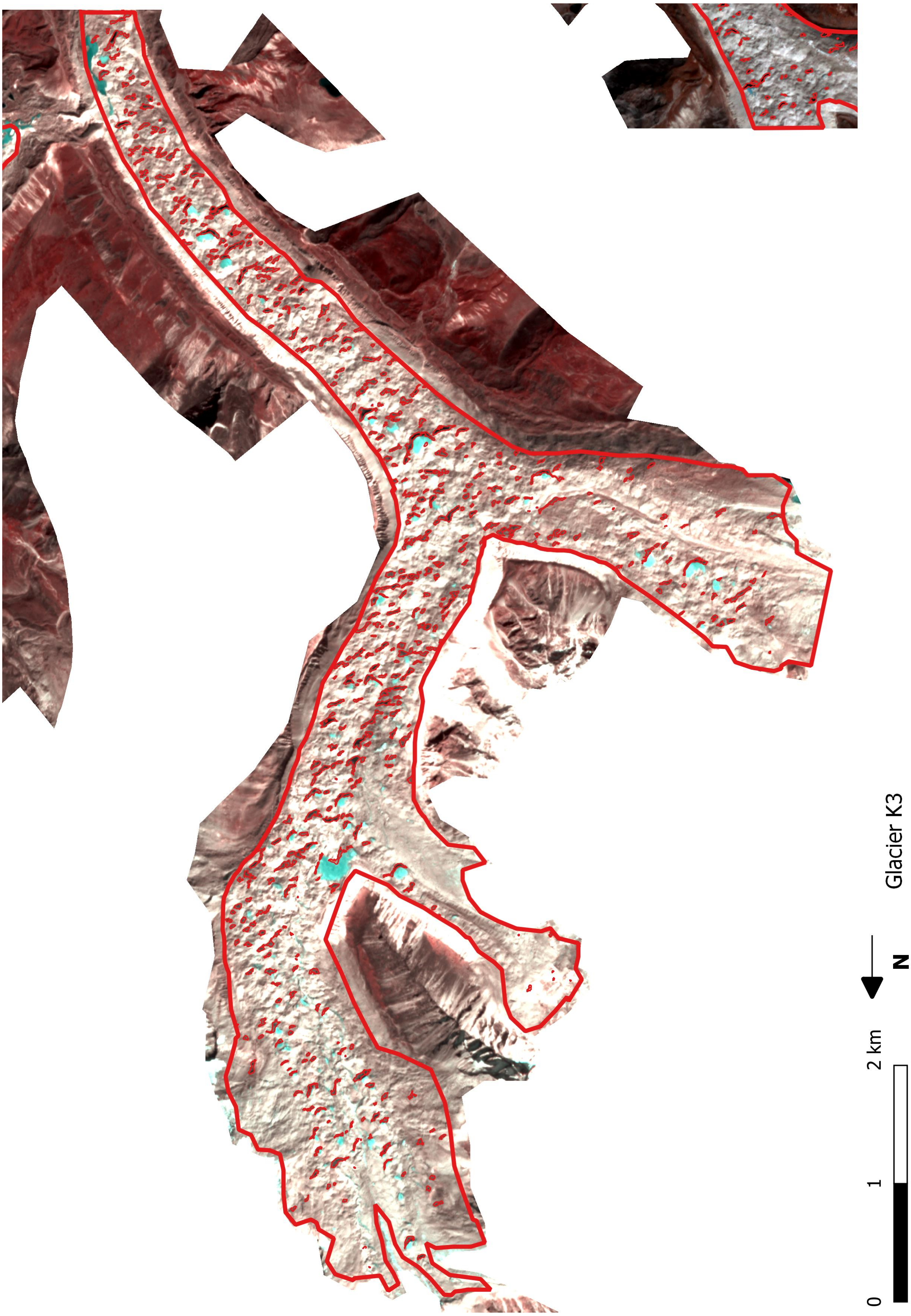
Glacier K3
N
0
1
2 km


Glacier K4
N
0
750
1500 m

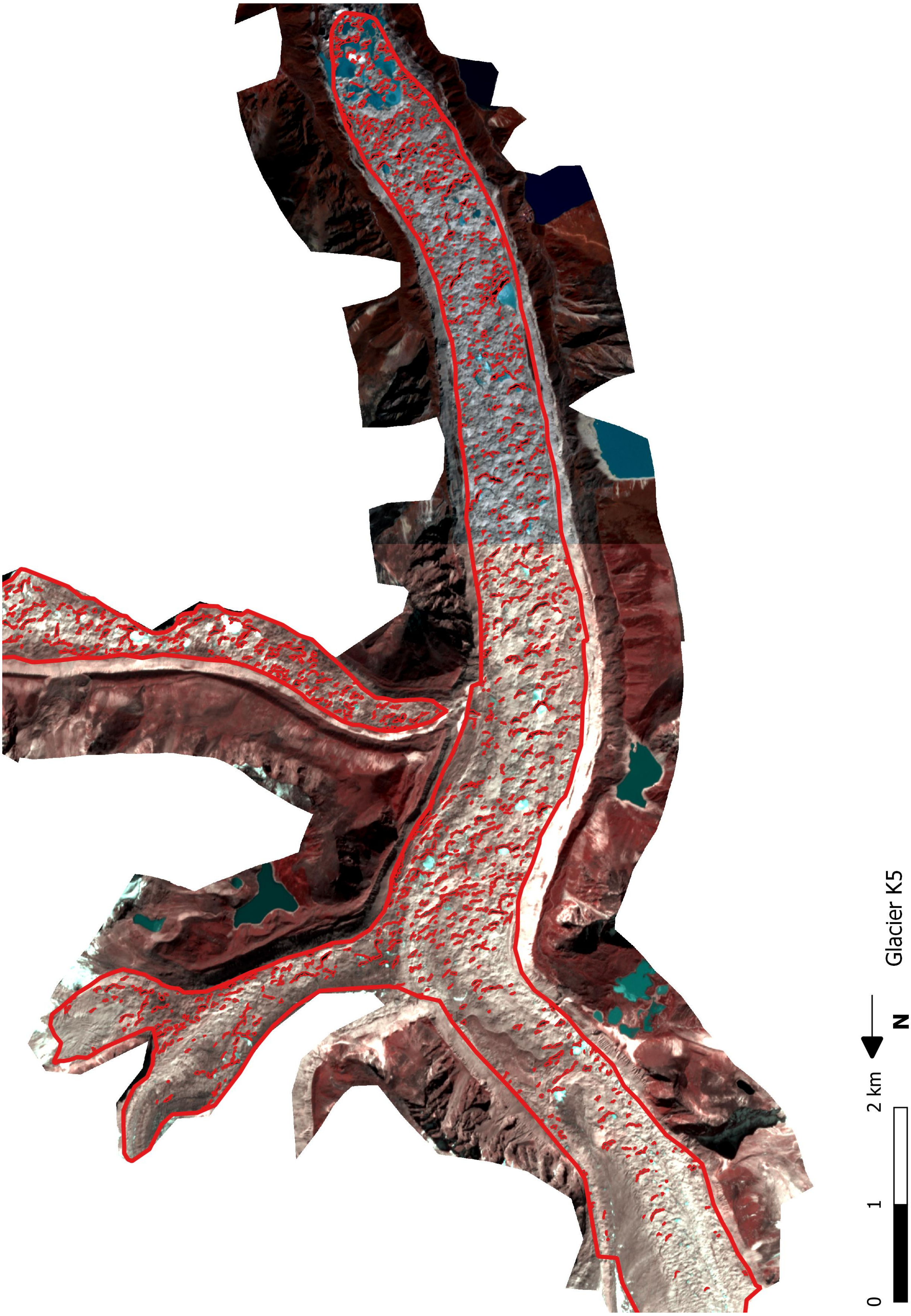
Glacier K5
N
0
1
2 km


Glacier K6
0
500
1000 m

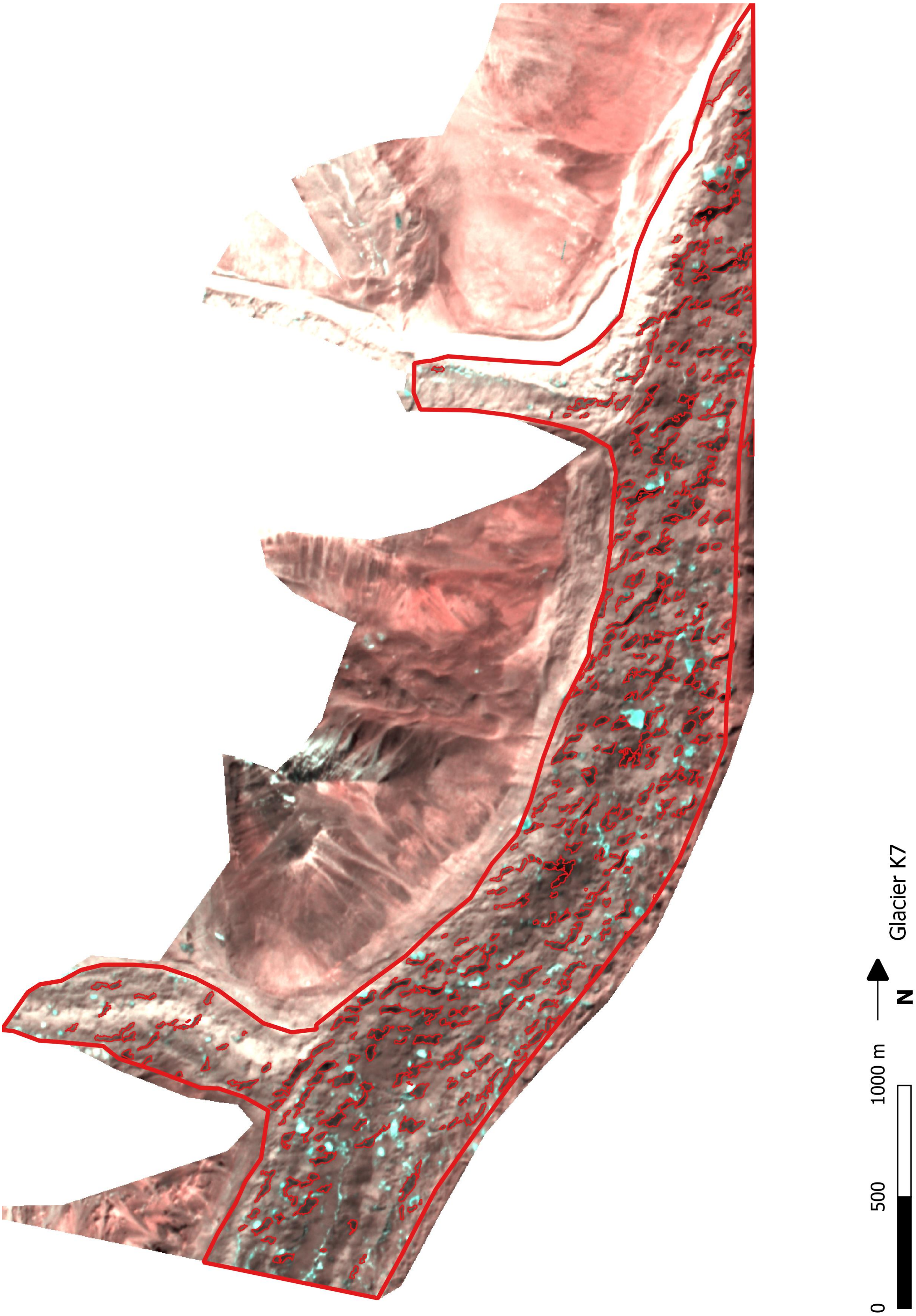
Glacier K7
N
0
500
1000 m

## 10.4 Ice Cliff Density Distributions

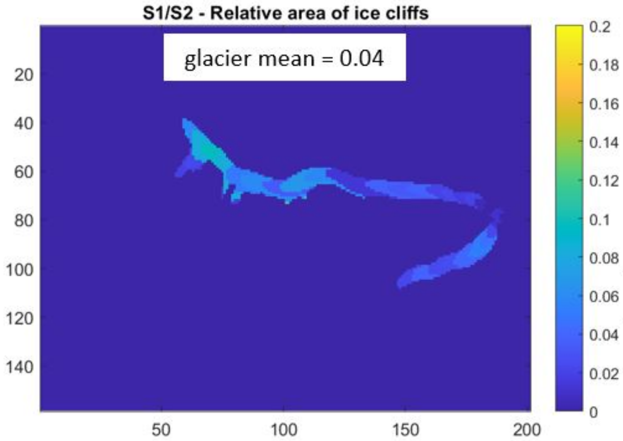

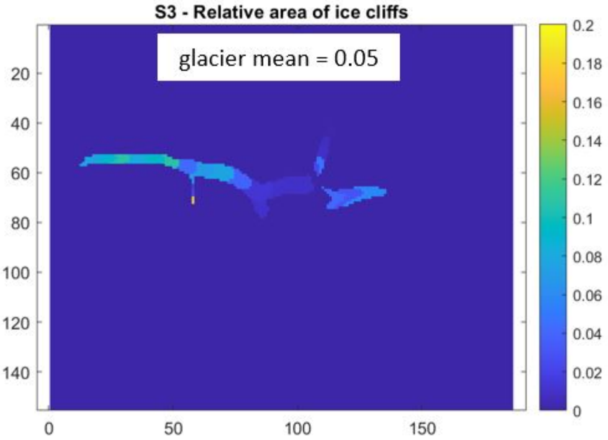

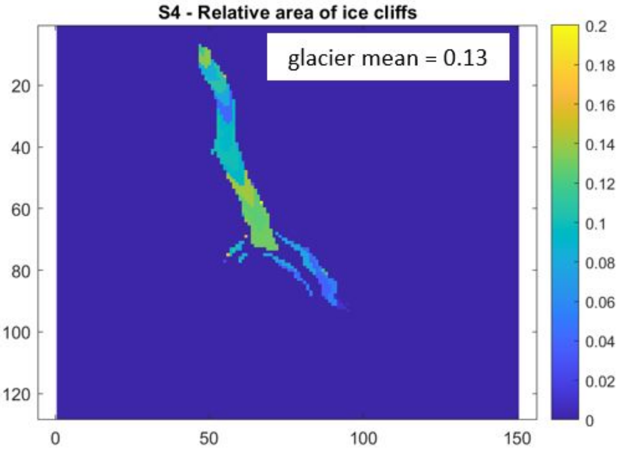

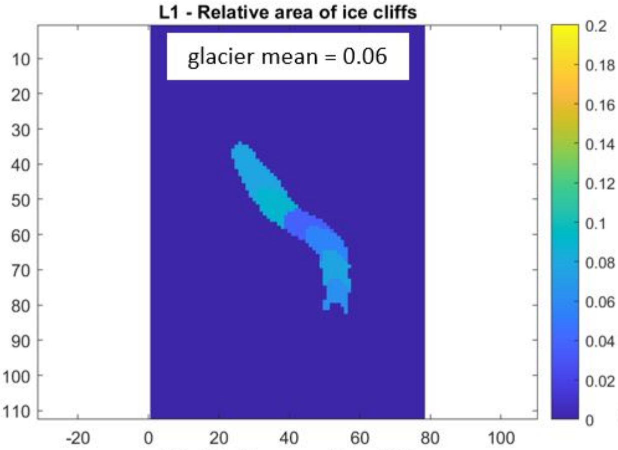
L1 - Relative area of ice cliffs
glacier mean = 0.06
10
20
30
40
50
60
70
80
90
100
110
-20
0
20
40
60
80
100
0.2
0.18
0.16
0.14
0.12
0.1
0.08
0.06
0.04
0.02
0

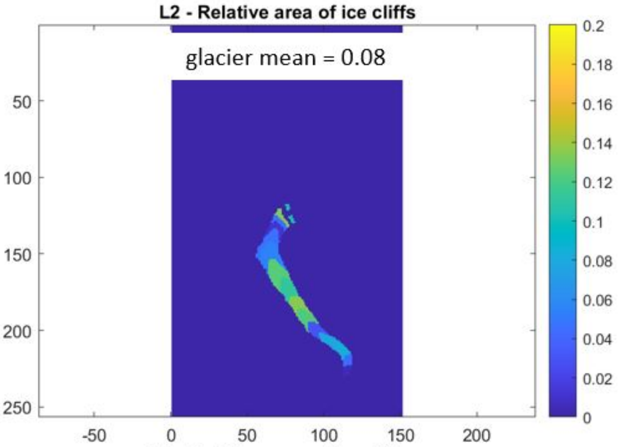
L2 - Relative area of ice cliffs
glacier mean = 0.08
50
100
150
200
250
-50
0
50
100
150
200
0.2
0.18
0.16
0.14
0.12
0.1
0.08
0.06
0.04
0.02
0

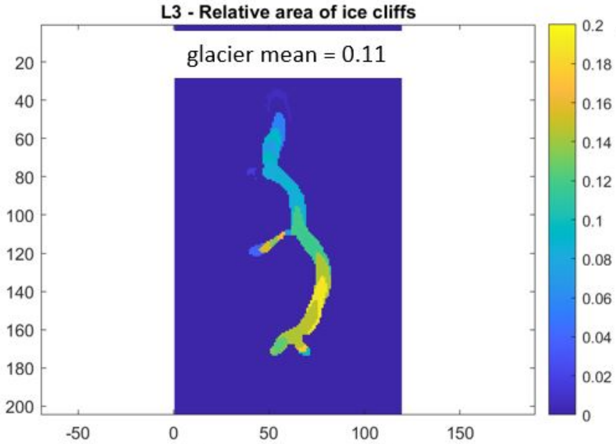
L3 - Relative area of ice cliffs
glacier mean = 0.11
20
40
60
80
100
120
140
160
180
200
-50
0
50
100
150
0.2
0.18
0.16
0.14
0.12
0.1
0.08
0.06
0.04
0.02
0

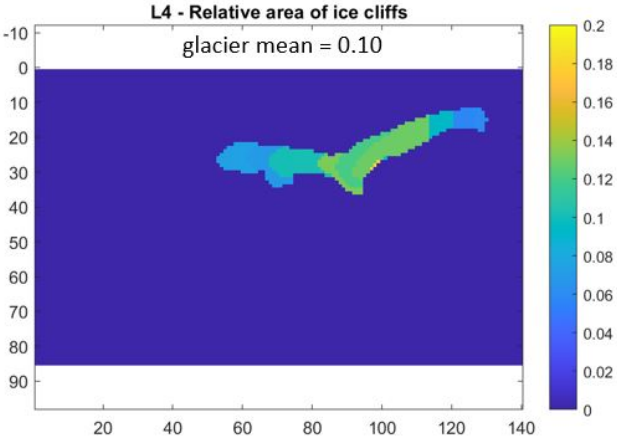
L4 - Relative area of ice cliffs
glacier mean = 0.10
-10
0
10
20
30
40
50
60
70
80
90
20
40
60
80
100
120
140
0.2
0.18
0.16
0.14
0.12
0.1
0.08
0.06
0.04
0.02
0

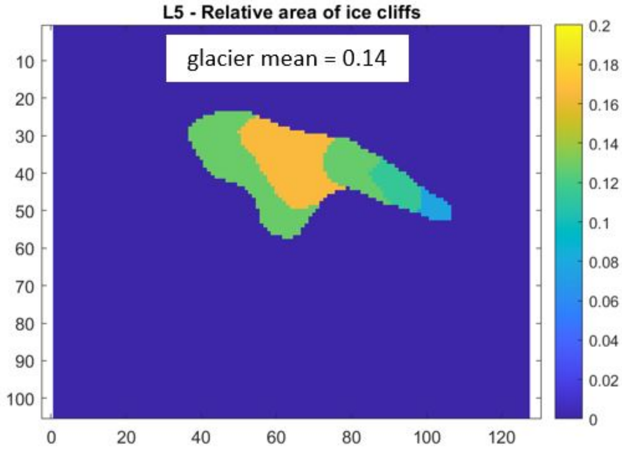
L5 - Relative area of ice cliffs
glacier mean = 0.14
10
20
30
40
50
60
70
80
90
100
0
20
40
60
80
100
120
0.2
0.18
0.16
0.14
0.12
0.1
0.08
0.06
0.04
0.02
0

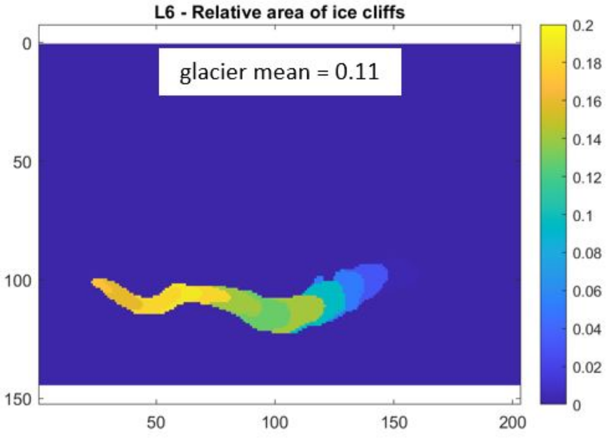
L6 - Relative area of ice cliffs
glacier mean = 0.11
0
50
100
150
50
100
150
200
0.2
0.18
0.16
0.14
0.12
0.1
0.08
0.06
0.04
0.02
0

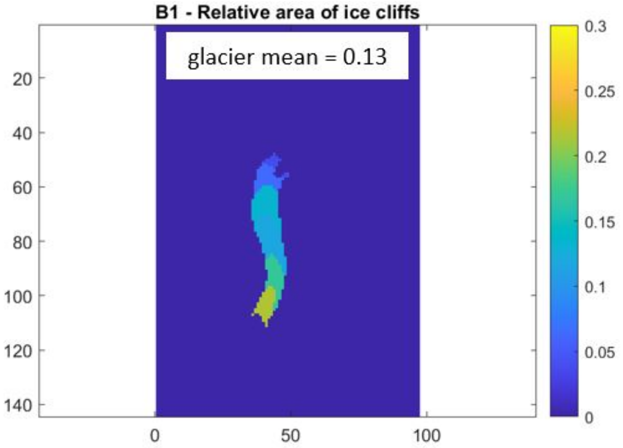
B1 - Relative area of ice cliffs

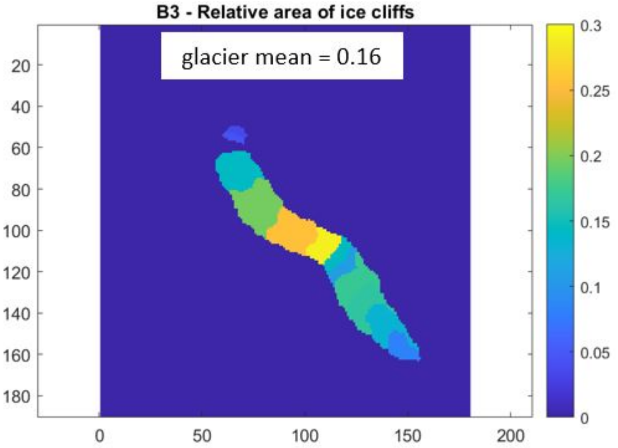
B3 - Relative area of ice cliffs

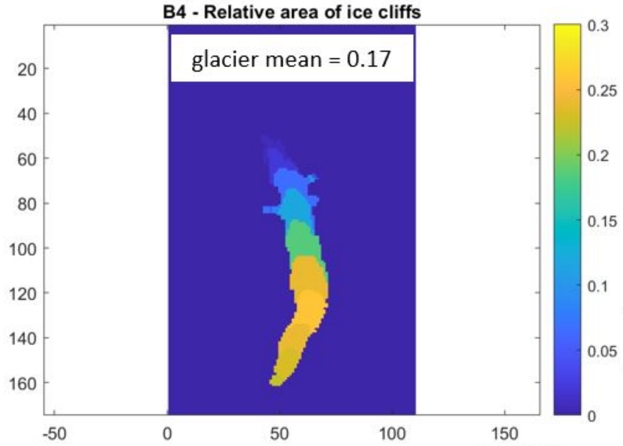
B4 - Relative area of ice cliffs

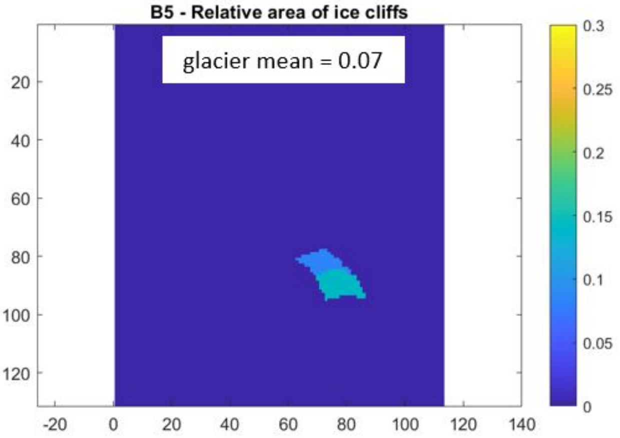
B5 - Relative area of ice cliffs

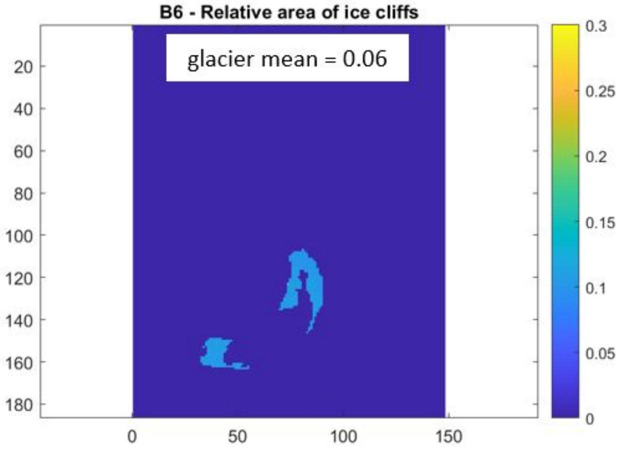
B6 - Relative area of ice cliffs

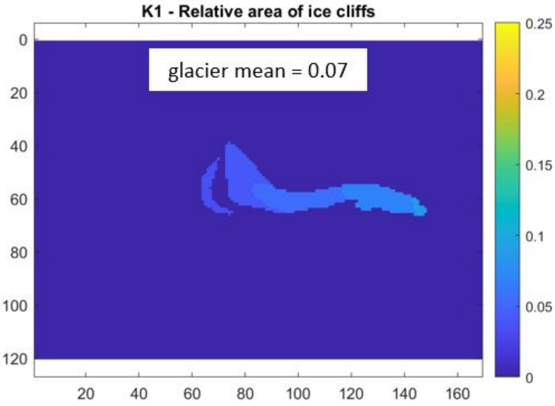
K1 - Relative area of ice cliffs
glacier mean = 0.07
0
20
40
60
80
100
120
20
40
60
80
100
120
140
160
0.25
0.2
0.15
0.1
0.05
0

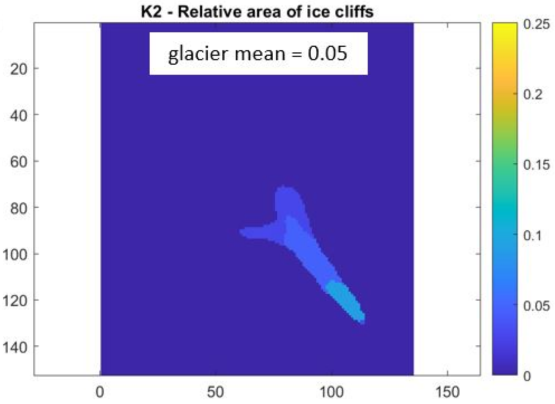
K2 - Relative area of ice cliffs
glacier mean = 0.05
20
40
60
80
100
120
140
0
50
100
150
0.25
0.2
0.15
0.1
0.05
0

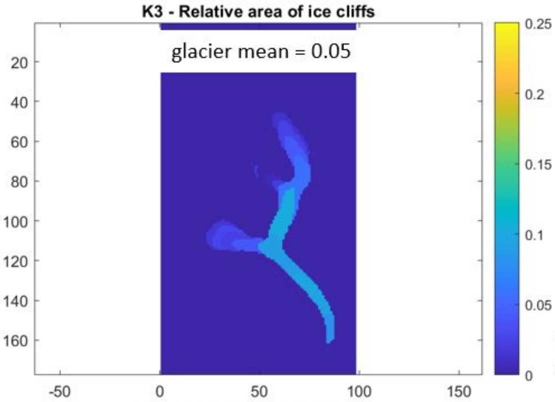
K3 - Relative area of ice cliffs
glacier mean = 0.05
20
40
60
80
100
120
140
160
-50
0
50
100
150
0.25
0.2
0.15
0.1
0.05
0

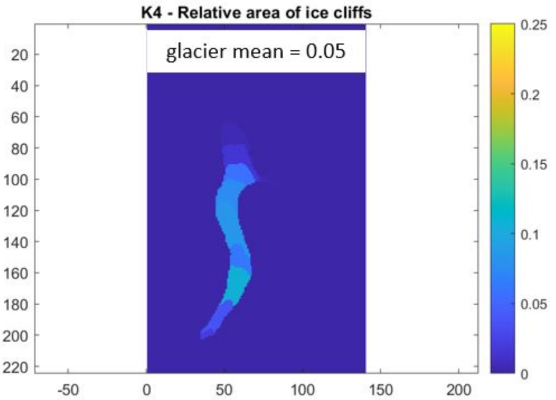
K4 - Relative area of ice cliffs
glacier mean = 0.05
20
40
60
80
100
120
140
160
180
200
220
-50
0
50
100
150
200
0.25
0.2
0.15
0.1
0.05
0

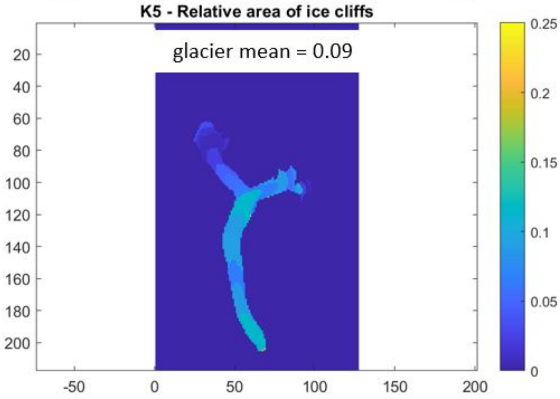
K5 - Relative area of ice cliffs
glacier mean = 0.09
20
40
60
80
100
120
140
160
180
200
-50
0
50
100
150
200
0.25
0.2
0.15
0.1
0.05
0

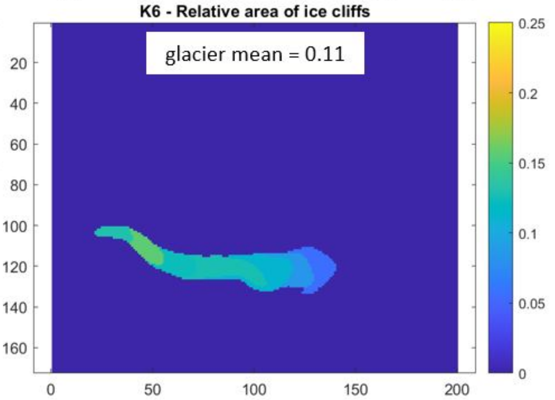
K6 - Relative area of ice cliffs
glacier mean = 0.11
20
40
60
80
100
120
140
160
0
50
100
150
200
0.25
0.2
0.15
0.1
0.05
0

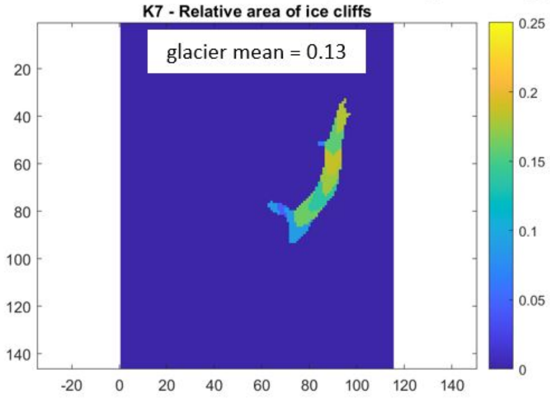
K7 - Relative area of ice cliffs
glacier mean = 0.13
20
40
60
80
100
120
140
-20
0
20
40
60
80
100
120
140
0.25
0.2
0.15
0.1
0.05
0

# Personal Declaration

I hereby declare that the submitted thesis is the result of my own, independent work. All external sources are explicitly acknowledged in the thesis.

Zürich, 28.09.2021

Seraina Walz